Flux-Limited Heat-flow and Magnetic-Field Transport in Laser-Plasmas

Contact: john.bissell@durham.ac.uk

J. J. Bissell
Department of Mathematical Sciences,
University of Durham,
DH1 3LE, United Kingdom

Abstract

It has long been recognised that classical theory overestimates the thermal flux in laser-plasma interactions when the temperature gradient is steep - an effect known as flux-limited heat-flow. To account for such discrepancies, many laser plasma fluid codes employ *ad hoc* flux-limiters, typically set to some fraction s_f of the free-streaming heat-flow $\mathbf{q}_f$, where $s_f < 1$ is 'tuned' by comparison with kinetic calculations. Here we argue that the inclusion of flux-limited heat-flow necessitates similar limitation of the thermoelectric term in Ohm's Law; indeed, we demonstrate that without such restrictions fluid codes are liable to over-estimate magnetic field advection, sometimes by more than an order of magnitude, with further implications for thermal energy transport.

1 Introduction

Reliable calculations for the transport of thermal energy and magnetic-field play a key role in efforts to understand laser-plasma interactions, and may prove crucial to the success of fusion experiments, such as those at the National Ignition Facility [1, 2, 3, 4, 5, 6, 7, 8, 9, 10]. Electron transport is commonly modelled using Braginskii's classical theory [11], which yields a physically intuitive picture of transport effects while retaining the level of sophistication necessary to describe more exotic phenomena. Unfortunately, however, classical theory has long been known to predict much larger heat-flows $\mathbf{q}$ in the presence of steep temperature gradients than those suggested by both experiment and kinetic simulation [12, 13, 14], an effect referred to as *flux limited heat flow*. When calculating transport using fluid codes therefore, it has become routine to account for such discrepancies by arbitrarily limiting the flux to some fraction s_f of the free-streaming heat-flow $\mathbf{q}_f$, where the limitation s_f can be adjusted on an *ad hoc* basis to yield agreement with experiment (see, for example, the review by Colombant *et al.* [15] and references therein).

In this report we consider the impact of flux-limited heat-flow on the transport of magnetic field which can be rapidly advected by $\mathbf{q}$ [16, 17], both in terms of a simple analysis of the restricted flux, and *via* numerical simulation using the classical transport code CTC [18, 19]. We argue that without a similarly restricted thermoelectric term in the expression for the magnetic field, flux-limited heat-flow calculations are liable to greatly overestimate both field compression and advection. Since magnetic fields can strongly suppress heat-flow in laser plasmas [5, 11], such inconsistencies are expected to impact further on thermal transport in turn. Similar problems are likely to exist in other transport models, for example, those involving a spatially convolved-flux [15, 20].

2 Background : Braginskii's Transport Equations

Braginskii's forms for the electric field $\mathbf{E}$ and heat-flow $\mathbf{q}$ are expressed by Ohm's Law and the heat-flow equation

$$en_e\mathbf{E} = -\nabla P_e + \mathbf{j}\times\mathbf{B} + \frac{m_e}{e\tau_B}\underline{\underline{\alpha}}^c\cdot\mathbf{j} - n_e\underline{\underline{\beta}}^c\cdot\nabla T_e, \quad (1)$$

$$\text{and} \quad \mathbf{q} = -\frac{n_e\tau_B T_e}{m_e}\underline{\underline{\kappa}}^c\cdot\nabla T_e - \left(\underline{\underline{\beta}}^c + \frac{5}{2}\underline{\underline{\mathbf{I}}}\right)\cdot\mathbf{j}\frac{T_e}{e} \quad (2)$$

respectively [11]. Here e is the elementary charge, n_e is the electron number density, T_e is the electron temperature (in energy units), m_e is the electron mass, $\mathbf{j}$ is the current, $\mathbf{B}$ is the magnetic flux density, and $P_e = n_eT_e$ is the electron pressure, while the Braginskii collision time $\tau_B \propto (T_e^{3/2}/n_e)$ may be related to the thermal collision time τ_T through the constant $c_B = 3\sqrt{\pi}/4$ such that $\tau_B = c_B\tau_T$. With $\underline{\underline{\mathbf{I}}}$ as the identity tensor, the transport coefficients, i.e., the resistivity $\underline{\underline{\alpha}}^c$, thermoelectric tensor $\underline{\underline{\beta}}^c$, and conductivity $\underline{\underline{\kappa}}^c$, are dimensionless functions of the atomic number Z and Hall Parameter $\chi = \omega_L\tau_B$ only, where $\omega_L = (e|\mathbf{B}|/m_e)$ is the electron Larmor frequency [11, 21, 22].[1] Note that a general transport coefficient $\underline{\underline{\eta}} \in \{\underline{\underline{\alpha}}^c, \underline{\underline{\beta}}^c, \underline{\underline{\kappa}}^c\}$ may be expressed in terms of components parallel and perpendicular to the $\mathbf{B}$-field using functions $\eta_\perp(\chi, Z)$, $\eta_\wedge(\chi, Z)$ and $\eta_\parallel(Z) = \eta_\perp(0, Z)$. However, in this report we shall assume an x-y planar geometry with $\mathbf{B} = B\mathbf{z}$, such that $\mathbf{B}\cdot\nabla\phi = \mathbf{B}\cdot\mathbf{A} = 0$ for scalar ϕ and vector $\mathbf{A}$ fields. Thus, with $\mathbf{b} = \mathbf{B}/|B|$, we have the simplified form [24]

$$\underline{\underline{\eta}}\cdot\mathbf{s} = \eta_\perp\mathbf{s} + \eta_\wedge\mathbf{b}\times\mathbf{s}, \quad (3)$$

where $\mathbf{s}$ is the driving force behind the transport (for example, $\mathbf{s} = \nabla T_e$ for the thermal conductivity $\underline{\underline{\kappa}}^c$) and the sign of the last term is negative for the resistivity $\underline{\underline{\alpha}}^c$.

[1] Here the term in $\left(\underline{\underline{\beta}}^c + (5/2)\underline{\underline{\mathbf{I}}}\right)$ in the heat-flow equation accounts for the difference between the total heat-flow $\mathbf{q}$ and the intrinsic heat-flow $\mathbf{q}_e'$, that is, $\mathbf{q} + (5T_e)/(2e)\mathbf{j} = \mathbf{q}_e'$ [19, 23].

3 Harmonic Flux Limitation

Of main concern here is the component of the heat-flow perpendicular to the temperature gradient and to which we will refer as the *diffusive heat-flow*, *viz*

$$\mathbf{q}_\perp = -\frac{c_B \tau_T n_e T_e}{m_e} \kappa_\perp \nabla T_e. \tag{4}$$

When implementing flux-limiters, this heat-flow is restricted to some fraction of the *free-streaming limit*

$$\mathbf{q}_f = -\frac{1}{2} n_e m_e v_T^3 \frac{\nabla T_e}{|\nabla T_e|}, \tag{5}$$

that is, the flux $\mathbf{q}_f$ which would result if all electrons had temperature T_e and moved at the thermal speed $v_T = (2T_e/m_e)^{1/2}$ in the direction $-\nabla T_e/|\nabla T_e|$. Our code CTC is an implicit solver, and for this reason some care must be taken to ensure consistent numerical implementation. Fortunately, it is relatively straightforward to apply a restriction by making the transformation

$$\mathbf{q}_\perp \to \mathbf{q}'_\perp, \quad \text{where} \quad \mathbf{q}'_\perp = \theta_f(r_f)\mathbf{q}_\perp \tag{6}$$

is the *flux-limited* (F.L.) diffusive heat-flow, with $\theta_f(r_f)$ as a dimensionless *flux-limiting factor* defined such that the magnitude of $\mathbf{q}'_\perp$ satisfies the harmonic mean

$$\frac{1}{|\mathbf{q}'_\perp|} = \frac{1}{|\mathbf{q}_\perp|} + \frac{r_f}{|\mathbf{q}_f|}, \quad \text{with} \quad r_f > 1 \tag{7}$$

as some kind of dimensionless *'flux-limiting coefficient'*. Indeed, rearranging this expression with reference to equation (6) we have

$$\theta_f(r_f) = \left(\frac{1}{1 + (r_f |\mathbf{q}_\perp|/|\mathbf{q}_f|)} \right), \tag{8}$$

and consequently

$$\mathbf{q}' \approx \begin{cases} \mathbf{q}_\perp, & \text{for} \quad |\mathbf{q}_\perp| \ll (|\mathbf{q}_f|/r_f) \\ \mathbf{q}_f/r_f, & \text{for} \quad |\mathbf{q}_\perp| \gg (|\mathbf{q}_f|/r_f), \end{cases} \tag{9}$$

so that, as required, the flux-limited diffusive heat-flow cannot exceed some fraction $(1/r_f)$ of the free streaming limit $\mathbf{q}_f$. Note that for very large or small values of r_f, corresponding to severely restricted or un-restricted heat-flows respectively, such implementation gives us

$$\lim_{r_f \to \infty} \mathbf{q}'_\perp = \frac{\mathbf{q}_f}{r_f} \quad \text{and} \quad \lim_{r_f \to 0} \mathbf{q}'_\perp = \mathbf{q}_\perp. \tag{10}$$

These limits illustrate one of the advantages of defining the upper bound on the F.L. flux in terms of $\mathbf{q}_f/r_f$ with $r_f > 1$, as opposed to a fraction $s_f \mathbf{q}_f$ with some constant $s_f < 1$. In particular, if one needs access to the unrestricted flux for purposes of numerical computation, it is more meaningful to let $r_f = 0$ in CTC than to set s_f equal to some arbitrarily large number.

From the expressions for the diffusive and free-streaming heat-flows in equations (4) and (5) respectively, the flux-limiting factor may be written as

$$\theta_f(r_f) = \left(1 + \frac{r_f c_B \lambda_T}{2 l_T} \kappa_\perp \right)^{-1}, \tag{11}$$

where l_T is characteristic *positive* thermal length-scale defined by

$$\frac{1}{l_T} = \frac{|\nabla T_e|}{T_e}, \quad \text{such that} \quad \frac{1}{l_T^2} = \frac{1}{l_{Tx}^2} + \frac{1}{l_{Ty}^2}, \tag{12}$$

with $l_{Tx} = T_e/(\partial T_e/\partial x)$ and $l_{Ty}/(\partial T_e/\partial y)$ as either positive *or* negative thermal length-scales in the x and y-directions respectively. Equation (11) forms the basis for our flux-limiter in CTC, and a motivation for the introduction of restricted thermoelectric effects.

4 Flux-Limited Magnetic Field-Advection

In laser-plasma interactions heat-flow effects are closely linked to magnetic field dynamics *via* the thermoelectric term in Ohm's Law of equation (1) [11]. Indeed, denoting the cross-gradient thermoelectric component $\beta_\wedge$ to the electric field as $\mathbf{E}_{\beta_\wedge}$, such that (see equation (3))

$$\mathbf{E}_{\beta_\wedge} = -\frac{1}{e} \beta_\wedge \mathbf{b} \times \nabla T_e, \tag{13}$$

the impact of the $\beta_\wedge$ term on field evolution may be understood through its contribution to Faraday's Law:

$$\left[\frac{\partial \mathbf{B}}{\partial t}\right]_{\beta_\wedge} = -\nabla \times \mathbf{E}_{\beta_\wedge} = \nabla \times (\mathbf{v}_N \times \mathbf{B}), \tag{14}$$

$$\text{where} \quad \mathbf{v}_N = -a_N \frac{\nabla T_e}{T_e}, \quad \text{and} \quad a_N = \frac{c_B}{2\chi} \frac{\lambda_T^2}{\tau_T} \beta_\wedge. \tag{15}$$

Since equation (14) is an advection equation, we see that the thermoelectric term acts to advect magnetic-field with a velocity $\mathbf{v}_N \propto -\nabla T_e$ directed down temperature gradients, a phenomenon known as the *Nernst effect* [16]. Here the *Nernst velocity* $\mathbf{v}_N$ has been written in terms of a *Nernst advection coefficient* a_N [19]. Noting that the diffusive heat-flow may be expressed

$$\mathbf{q}_\perp = -\frac{3}{2} n_e d_T \nabla T_e, \quad \text{where} \quad d_T = \frac{c_B}{3} \frac{\lambda_T^2}{\tau_T} \kappa_\perp \tag{16}$$

is the coefficient of thermal diffusion, one may write the Nernst velocity as

$$\mathbf{v}_N = \frac{a_N}{d_T} \frac{\mathbf{q}_\perp}{U_T}, \quad \text{with} \quad U_T = \frac{3}{2} n_e T_e \tag{17}$$

as the energy density. Hence, because $a_N \approx d_T$ [19], and since $\mathbf{q}_\perp/U_T$ represents a characteristic velocity associated with $\mathbf{q}_\perp$, one may interpret the Nernst effect physically as advection of magnetic field with the diffusive heat-flow (cf. Nishiguchi *et al.* [16]). Indeed, this interpretation continues to hold even when either non-local [17] or super-Gaussian [24] transport effects become important, and classical transport theory begins to break down. Note that in regions where $\mathbf{v}_N$ is divergent, compressional amplification by the Nernst effect can have dramatic consequences for the magnetic field, magnifying field strengths by factors of 10-100 [25], meaning that Nernst can be far more important than other more commonly considered effects, such as frozen in flow [26]. Since strong fields tend to reduce the heat-flow, and thus the Nernst effect itself, these interactions play a key role in determining the interplay bewteen magnetic field dynamics and thermal evolution [26, 27].

Of course, in a flux-limited codes it is $\mathbf{q}'_\perp$ rather than $\mathbf{q}_\perp$ which determines the heat-flow, and in such cases the Nernst velocity expressed as it is in equation (17) will be a factor $1/\theta_f$ greater than the characteristic heat-flow velocity $\mathbf{q}'_\perp/U_T$. To restore physical consistency to flux-limited calculations it is therefore necessary to restrict the thermoelectric term according to the transformation

$$\mathbf{E}_{\beta_\wedge} \to \mathbf{E}'_{\beta_\wedge} = \theta_N \mathbf{E}_{\beta_\wedge}, \quad \text{with} \quad \theta_N = \theta_f \tag{18}$$

as the *'thermoelectric limiting factor'*. Indeed, in this way we obtain

$$\left[\frac{\partial \mathbf{B}}{\partial t}\right]_{\beta_\wedge} = -\nabla \times \mathbf{E}'_{\beta_\wedge} = \nabla \times (\mathbf{v}'_N \times \mathbf{B}), \tag{19}$$

$$\text{where} \quad \mathbf{v}'_N = -a_N \theta_N \frac{\nabla T_e}{T_e} = \frac{a_N}{d_T}\frac{\mathbf{q}'_\perp}{U_T} \tag{20}$$

is the restricted Nernst velocity in terms of advection with the characteristic *flux-limited* heat-flow velocity $\mathbf{q}'_\perp/U_T$ as required. This restricted thermoelectric term has been implemented in CTC alongside our flux limiter.

5 Preliminary Simulations

In light of our discussion in §4, it appropriate to consider possible discrepancies in classical transport calculations arising from limiting the heat-flow when leaving the Nernst thermoelectric term unrestricted. In this section therefore, we briefly describe data from some preliminary one-dimensional CTC+ simulations of an initially uniform plasma which is laser-heated for 150ps. We adopt parameters similar to those assumed in reference [19] and applied fields ranging between 0.1T, 1T and 10T.

For comparative purposes, we repeat a set of three simulations for each the various field strengths asserting different conditions on the limited transport. In particular, we set the transport to be either: i) 'Dual-Limited', in which case both the heat-flow and Nernst effect are restricted, with $r_f = r_N = 30$ (i.e., an upper limit on $\mathbf{q}'_\perp$ of $0.0\dot{3}\mathbf{q}_f$); ii) 'Half-Limited', for which only the heat-flow is restricted, with $r_f = 30$ and $r_N = 0$; or iii) 'Full Classical', in which case neither the heat-flow nor Nernst effect are restricted ($r_f = r_N = 0$).

Results from these simulations are displayed graphically in figure 1, and demonstrate marked discrepancies between the field calculations, especially at low magnetisation. For example, considering the region of peak field compression for both the 'Half-Limited' and 'Dual-Limited' 0.1T simulations, which occurs at 125μm, then for the former we find fractional-difference compression by $(0.26 - 0.1)/0.1 = 1.6$, and in the latter by $(0.11 - 0.1)/0.1 = 0.1$, that is, a factor of 16 discrepancy. Qualitative differences are also present: in all of the 'Half-Limited' simulations, maximum cavitation of the field occurs beyond the centrally heated region; this contrasts with the 'Dual-Limited' and 'Full Classical' calculations, for which field cavitation is most pronounced at the origin. The differences between the various calculations mainly arise in two ways:

1. Even when all other parameters are equal, the unrestricted Nernst velocity is larger than the restricted Nernst velocity by the factor $1/\theta_N$.

2. Flux-limited heat-flow results in steeper gradients relative to classical predictions, and thus larger ∇T_e in the thermoelectric term.

Ultimately these effects will often be intimately linked, though for the 10T simulations they are effectively decoupled. Indeed, for large $\mathbf{B}$ we find that magnetic suppression of the diffusive thermal conductivity forces a sufficiently small $\mathbf{q}'_\perp \approx \mathbf{q}_\perp$ such that the effect of Nernst compression is minimal, and the field stays uniform to within approximately 5%. In terms of thermal evolution, this means that conditions are almost identical in each of the three types of calculation, yielding very similar thermal profiles. However, although ∇T_e does not change much across the different calculations, the two simulations with unrestricted Nernst exhibit enhanced advection of the field by the factor $1/\theta_N$.

From the results presented here it would appear that the discrepancy between thermal profiles derived from the 'Half-Limited' and 'Full-Limited' simulations is small, but this is partly a consequence of heating for only 150ps. Indeed, when one looks at the field data from the 0.1T runs, one can clearly see the formation of a magnetic-field transport barrier when only the heat-flow is flux-limited, contrasting with a relatively small amount of field compression when both heat-flow and the Nernst effect are restricted: at later times one might expect this to play an important role in the transport of thermal energy. Sadly, however, it has not been possible to run out much further than 150ps in the 'Half-Limited' simulations, since sharp steeping of the magnetic-field as it forms the transport barrier (evidenced in figure 1) seems to destabilise the numerics of CTC. Interestingly, it appears that simulation results are most stable when the field moves with the heat-flow, consistent with the physical picture of Nernst advection.

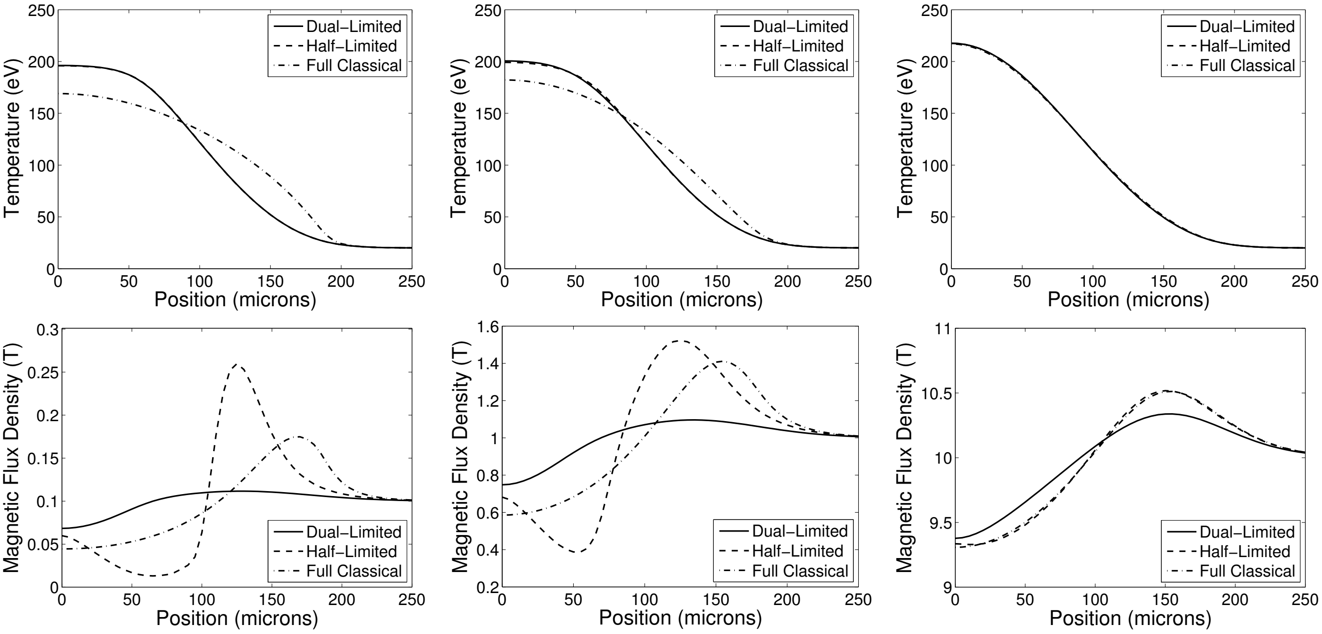

Figure 1: Temperature (top row) and **B**-field (bottom row) profiles following 150ps laser-heating of initially uniform plasmas magnetised at 0.1T (left column), 1T (middle column), and 10T (right column).

6 Conclusion

Flux-limiters are a commonly employed numerical 'fix' for describing lower than classically predicted heat-flows in laser-plasma interactions (§1, §2), and can be implemented in a relatively straightforward fashion using a 'flux-liming factor' θ_f (§3). However, given the physical interpretation of the Nernst effect as advection of the magnetic-field with the heat-flow, flux-limited codes should also restrict the Nernst term in Ohm's Law *via* a 'thermoelectric-limiting factor' $\theta_N = \theta_f$ (§4). Indeed, our simulations demonstrate the importance of accounting for such restricted Nernst advection, especially for weakly magnetised plasmas, and that failure to limit Nernst may result in the formation of un-physically large transport barriers (§5). These result suggest that other thermal transport models, e.g. convolved-fluxes $\tilde{\mathbf{q}}_\perp$ [15, 20], should also limit Nernst; one method for doing so might be to simply replace the thermoelectric term in Ohm's Law with a direct thermal advection force, *viz*

$$\frac{1}{e}\underline{\underline{\beta}}^c \cdot \nabla T_e \quad \longrightarrow \quad \frac{\tilde{\mathbf{q}}_\perp \times \mathbf{B}}{3n_e T_e/2} \tag{21}$$

(cf. Haines [23]). However, more work is needed in combination with kinetic calculations to investigate the potential for such effects to impact on thermal profiles.

References

[1] S. H. Glenzer *et al.*, *Phys Plasmas*, **6**(5):2117–2128, 1999.

[2] J. Lindl *et al.*, *Phys Plasmas*, **11**(2):339–491, 2004.

[3] P. M. Nilson *et al.*, *Phys. Rev. Lett.*, **97**(25):255001, 2006.

[4] B. Frolov *et al.*, *New J. Phys.*, **8**(56):1367–2630, 2006.

[5] D. H. Froula *et al.*, *Phys. Rev. Lett.*, **98**:135001, 2007.

[6] C. K. Li *et al.*, *Phys. Rev. Lett.*, **99**(1):015001, 2007.

[7] C. K. Li *et al.*, *Phys. Rev. Lett.*, **99**(5):055001, 2007.

[8] G. Schurtz *et al.*, *Phys. Rev. Lett.*, **98**:095002, 2007.

[9] D. H.Froula *et al.*, *Plasma Phys and Controlled Fusion*, **51**(2):024009, 2009.

[10] C. K. Li *et al.*, *Phys. Rev. E*, **80**(1):016407, 2009.

[11] S. I. Braginskii, Transport Processes in a Plasma. *Reviews of Plasma Physics*, 1:205, 1965.

[12] R. C. Malone *et al.*, *Phys. Rev. Lett*, **34**(12):721–724, 1975.

[13] A. R. Bell *et al.*, *Phys. Rev. Lett*, **46**(4):243–246, 1981.

[14] A. Sunahara *et al.*, *Phys. Rev. Lett.*, **91**(9):095003, 2003

[15] D. G. Colombant *et al.*, *Phys Plasmas*, **11**:072702, 2005

[16] A. Nishiguchi *et al.*, *Phys Fluids*, **28**(12):3683–3690, 1985.

[17] T. H. Kho and M. G. Haines, *Phys. Rev. Lett.*, **55**(8):825–828, 1985.

[18] J. J. Bissell *et al.*, *Phys. Rev. Lett.*, **105**(17):175001, 2010.

[19] J. J. Bissell, *Magnetised Transport and Instability in Laser Produced Plasmas*, Ph.D. thesis, Imperial College of Science, Technology, and Medicine (London), 2011.

[20] E. M. Epperlein and R. W. Short, *Phys Fluids*, **3**(11):3092–3098, 1991.

[21] E M Epperlein, *J.Phys D*, **17**(9):1823–1827, 1984.

[22] E. M. Epperlein and M. G. Haines, *Physics of Fluids*, **29**(4):1029–1041, 1986.

[23] M. G. Haines, *Plasma Physics and Controlled Fusion*, **28**(11):1705–1716, 1986.

[24] J. J. Bissell *et al.*, *New J. Phys*, **15**(2):025017, 2013.

[25] A. Nishiguchi *et al.*, *Phys. Rev. Lett.*, **53**(3):262265, 1984.

[26] C. P. Ridgers *et al.*, *Phys. Rev. Lett.*, **100**(7):075003, 2008.

[27] J. F. Luciani *et al.*, *Phys. Rev. Lett.*, **55**(22):24212424, 1985.

Quantum radiation reaction in laser-electron beam collisions

Contact: tom.blackburn@physics.ox.ac.uk

T. G. Blackburn
Clarendon Laboratory,
University of Oxford,
Parks Road, Oxford,
OX1 3PU, United Kingdom

J. G. Kirk
Max-Planck-Institut für Kernphysik,
Postfach 10 39 80,
69029 Heidelberg,
Germany

C. P. Ridgers
Central Laser Facility,
STFC Rutherford Appleton Laboratory,
Chilton, Didcot,
OX11 0QX, United Kingdom

A. R. Bell
Central Laser Facility,
STFC Rutherford Appleton Laboratory,
Chilton, Didcot,
OX11 0QX, United Kingdom

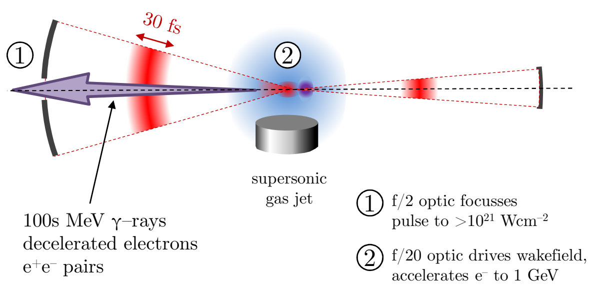

Fig. 1: An experimental geometry that could demonstrate quantum radiation reaction. The GeV electrons decelerate in large fields at the laser focus, producing gamma rays that pass through a hole in the f/2 optic.

Abstract

As the power focussed in laser facilities exceeds 1 PW, a crossover regime between classical and QED physics will be reached. The emission of high-energy gamma rays will dominate electron dynamics in these ultra-intense laser fields. Understanding these processes will be vital for the next generation of high-intensity laser experiments. Under current conditions, however, it will be possible to demonstrate the stochastic nature of photon emission in the generation of highly energetic gamma rays by a GeV electron beam counterpropagating into a laser pulse of intensity 10^{21} to 10^{22}Wcm^{-2}.

1 Motivation

The magnitude of strong-field QED effects is controlled by the Lorentz invariant parameter $\eta = |F_{\mu\nu}p^{\nu}|/mcE_{\text{Sch}}$ [1], where $F_{\mu\nu}$ is the electromagnetic field tensor, p^{μ} (m) the electron four-momentum (mass) and E_{Sch} is the Schwinger field [2] (equivalent intensity $I_{\text{Sch}} = 2 \times 10^{29}$ Wcm^{-2}). η compares the strength of the electromagnetic field in the electron rest frame to that of the Schwinger field (also called the critical field of QED), at which pair production from the vacuum is possible.

For an ultrarelativistic electron with Lorentz factor γ colliding antiparallel to a laser pulse of intensity I, this is well-approximated by $\eta = 2\gamma\sqrt{I/I_{\text{Sch}}}$. The f/2 parabolic optic of the Astra-Gemini laser may be capable of focussing a 30 fs, $\lambda = 1\,\mu$m laser pulse to a peak intensity $> 2\times 10^{21}$ Wcm^{-2} (strength parameter $a_0 > 30$). Thus $\eta \sim \mathcal{O}(0.1)$ could be achieved with GeV electrons, and strong-field QED effects begin to become significant.

The electron motion in fields of this intensity will be dominated by radiation reaction. This can be modelled classically with the Lorentz-Abraham-Dirac force, usually in the Landau-Lifshitz prescription [3]. This adds to the equation of motion for the electron the term

$$\left.\frac{\mathrm{d}\mathbf{p}}{\mathrm{d}t}\right|_{\text{rad}} \simeq -\frac{2\alpha_{\text{f}}}{3}\eta^2 mc\hat{\mathbf{p}} \tag{1}$$

where α_{f} is the fine-structure constant. However, this cannot give a complete description of the electron motion when $\eta \sim 1$ because the typical amount of energy lost in a single emission, $0.44\eta\gamma mc^2$ [4], becomes comparable to the energy of the electron. Therefore the electron is no longer subject to continuous loss of energy to radiation and the process of photon emission must be treated stochastically.

The probability rate that an electron with parameter η emits a photon with normalised energy $\chi = (\hbar\omega/2mc^2)\sqrt{I/I_{\text{Sch}}}$ is calculated [5, 6] to be

$$\frac{\mathrm{d}^2\tau}{\mathrm{d}t\mathrm{d}\chi} = \frac{\sqrt{3}\alpha_{\text{f}}}{2\pi\tau_{\text{C}}}\frac{\eta}{\gamma}\frac{F(\eta,\chi)}{\chi} \tag{2}$$

where τ is the optical depth against emission and $F(\eta,\chi)$ the quantum synchrotron function. This is non-zero only for $0 < \chi < \eta/2$ [7] and includes spin-flip transitions [8]:

$$F(\eta,\chi) = \frac{4\chi}{3\eta^2}\left[\left(1 - \frac{2\chi}{\eta} + \frac{1}{1-2\chi/\eta}\right)K_{2/3}(\delta) - \int_{\delta}^{\infty} K_{1/3}(t)\,\mathrm{d}t\right] \tag{3}$$

where $\delta(\eta, \chi) = (4\chi/3\eta^2)/(1 - 2\chi/\eta)$.

The fact that a high-energy electron has now a probability to radiate a gamma ray will give rise to a phenomenon called 'straggling'. An electron propagating through a strong laser pulse, which will have a temporal intensity profile, may reach the centre of that pulse having lost much less energy than would be possible if it radiated classically. Then $\eta_{\max} = 2\gamma_0\sqrt{I_0/I_{\mathrm{Sch}}}$, where γ_0 is the electron's initial Lorentz factor and I_0 the peak intensity of the pulse. This will always be greater than the maximum η that can be reached classically.

The spectrum of emitted photons is controlled by $F(\eta, \chi)$, the high-energy tail of which increases non-linearly with η. Therefore straggling electrons emit more gamma rays with higher energy.

2 Model

We have developed a Monte-Carlo code to simulate the collision of an energetic electron beam with an intense laser pulse. As $\gamma \gg a_0$, we neglect any transverse momentum gained from the laser fields and the space-charge field of the electron beam.

At the start of the simulation, each electron is assigned a 'final' optical depth τ_{f}, using $P = 1 - \exp(-\tau_{\mathrm{f}})$ where P is a uniformly distributed pseudorandom number $\in (0, 1)$. The total differential optical depth against emission

$$\frac{\mathrm{d}\tau}{\mathrm{d}t} = \frac{\sqrt{3}\alpha_{\mathrm{f}}}{2\pi\tau_{\mathrm{C}}}\frac{\eta}{\gamma}\int_0^{\eta/2}\frac{F(\eta,\chi)}{\chi}\,\mathrm{d}\chi \tag{4}$$

is then integrated along the electron trajectory. When $\tau = \tau_{\mathrm{f}}$, emission takes place and the photon energy is obtained by pseudorandomly sampling the quantum synchrotron distribution. The electron then recoils, losing energy equal to that of the generated gamma ray; between emissions, its energy remains constant.

We compare this fully stochastic model with one that is semi-classical. In this case the electron loses energy according to (1), modified to include a damping factor $g(\eta) \in (0, 1)$. This is necessary because quantum corrections mean that the total power lost in synchrotron radiation is smaller than the equivalent classical power [5, 6]. For consistency, photon spectra are obtained by sampling at each timestep the quantum synchrotron distribution. $g(\eta)$ has been measured in electron beam-crystal experiments [9] and is included in the model in [10] to simulate laser-electron collisions for electrons with $\gamma_0 = 400$, where η is small enough that probabilistic effects can be neglected.

3 Simulation results

The parameters of the simulation are are as follows: the laser pulse has wavelength $\lambda = 1\,\mu$m, is linearly polarised and has Gaussian temporal profile with a full width at half-maximum (FWHM) of 30 fs. The electrons have initial gamma factor $\gamma_0 = 2 \times 10^3$, corresponding to a GeV, and propagate along the optical axis antiparallel to the laser pulse.

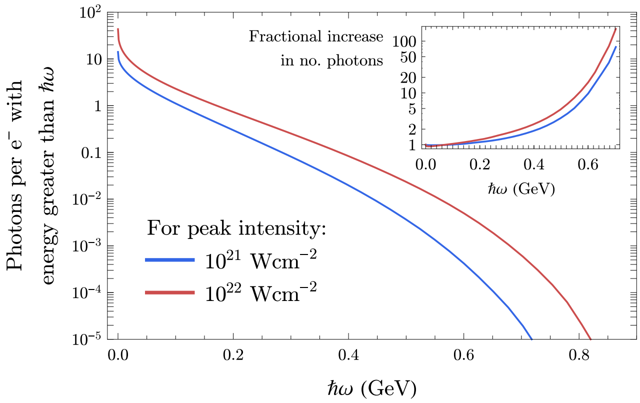

Fig. 2: The number of photons with energy greater than $\hbar\omega$ for a 1 GeV electron incident on a laser pulse with given peak intensity and (inset) the fractional increase in the same gained by treating emission discontinuously.

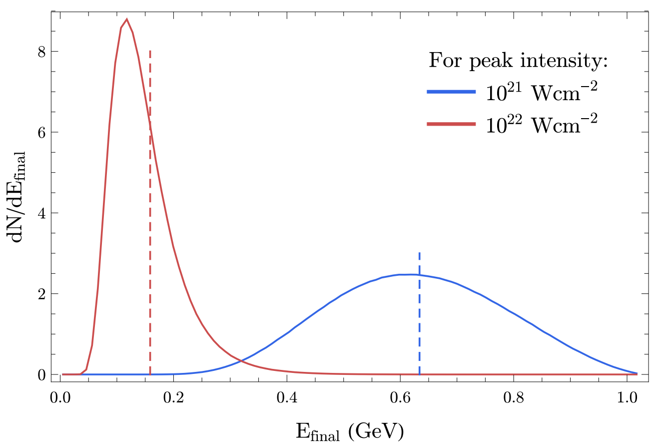

Fig. 3: The energy distribution for a 1 GeV electron that has passed through a laser pulse with given peak intensity. Dashed lines give the final energy that would be reached by a classically radiating electron.

We have found that modelling photon emission as stochastic leads to a dramatic increase in the yield of photons with energy comparable to that of the electron. Fig. 2 shows this increase is greater than an order of magnitude for photons with $\hbar\omega > 500$ MeV. If these photons can be detected, it would provide a clear signal that some electrons were incident on, and straggled through, the region of highest laser intensity.

Furthermore, as the electrons lose energy probabilistically, a monoenergetic beam will acquire a spread in energy as it propagates through the laser pulse. It can be seen in Fig. 3 that more than half the electron beam loses more energy than would be possible classically.

4 Conclusion

It is now possible to probe the quantum radiation reaction dominated regime in a high-intensity laser facility. Using a laser wakefield to drive GeV electrons into a laser pulse of intensity $> 10^{21}\,\mathrm{Wcm}^{-2}$ can make $\eta \sim 0.1$, at which point the stochastic nature of emission radically changes the spectrum of emitted gamma rays.

As laser intensities continue to increase, this will lead to more exotic phenomena, such as the generation of electron-positron pair plasmas [11] in laser-solid experiments above $10^{23}\,\mathrm{Wcm}^{-2}$.

By attempting to detect either the enhanced yield of high-energy gamma rays caused by straggling, or the consequent increase in energy loss of the electron beam, we can obtain a good signal of strong-field QED effects at intensities well below this.

References

[1] J. G. Kirk, A. R. Bell and I. Arka, Plasma Phys. Control. Fusion **51**, 085008 (2009)

[2] J. Schwinger, Phys. Rev. **82**, 664 (1951)

[3] L. D. Landau and E. M. Lifshitz, *The Course of Theoretical Physics* Vol. 2, (Butterworth-Heinemann, Oxford, 1987)

[4] A. R. Bell and J. G. Kirk, Phys. Rev. Lett. **101**, 200403 (2008)

[5] T. Erber, Rev. Mod. Phys. **38** 4, 626 (1966)

[6] V. N. Baier, V. M. Katkov and V. M. Strakhovenko, *Electromagnetic Processes at High Energies in Oriented Single Crystals*, (World Scientific, Singapore, 1998)

[7] V. I. Ritus, *Quantum effects of the interaction of elementary particles with an intense electromagnetic field*, Moscow Izdatel Nauka AN SSR Fizicheskii Institut Trudy **111**, 5 (1978)

[8] K. K. Andersen *et al.*, Phys. Rev. D **86**, 072001 (2012)

[9] U. I. Uggerhøj, Rev. Mod. Phys. **7**, 1131 (2005)

[10] A. G. R. Thomas *et al.*, Phys. Rev. X **2**, 041004 (2012)

[11] C. P. Ridgers *et al.*, Phys. Rev. Lett. **108**, 165006 (2012)

Angular distribution of high harmonics generated during laser-preplasma interaction

Contact *raoul.trines@stfc.ac.uk*

W. Boekee-West

The University of Warwick
Coventry, CV4 7AL, UK

R. Trines, A. Machacek, P. Norreys

STFC Rutherford Appleton Laboratory
Didcot, OX11 0QX, UK

Abstract

High harmonic generation in laser-solid interactions is important for the generation of sub-fs pulses having ultrahigh intensity [Baeva et al., Phys. Plasmas (2011)]. In order to maximise the efficiency of this process, a precise characterisation of the angular distribution of the emitted harmonic spectrum is indispensable. The results of particle-in-cell simulations indicate that the maximum intensity of the harmonics is found at angles close to the target surface, rather than close to the incident or reflected laser beam, for preformed plasma. This appears closely related to the deformation of the critical surface by the impact of the laser beam and laser-plasma instabilities in the area of impact. The effect of density gradient scale length, laser angle of impact and laser pulse intensity and duration on the angular distribution of the harmonics will be discussed.

Introduction

In laser-target interaction, especially when long (nanosecond) or strongly focused pulses are used, the laser impact will generate a halo of ablated plasma, extending from the impact spot. This plasma halo can have a scale length of many microns, and extend over a fairly long distance from the target. Its presence will strongly modify any subsequent laser-target interactions. This is especially important in the case of high-harmonic generation (HHG) in oblique laser-solid interactions [1-6]. Most of the models for laser reflection and HHG assume that the target surface is a "hard-edged" moving mirror [7-11]. Also, most theoretical studies of HHG are one-dimensional and do not cover the angular distribution of the emitted harmonics. However, a preplasma with a 3-5 µm scale length is anything like "hard-edged" to a laser pulse with 1 µm wave length, and when the laser pulse contains enough energy to drive plasma turbulence, even familiar concepts like the "critical density surface" (the surface where the effective laser reflection should take place) suddenly become hard to define. Similarly, the reflection of a laser beam by a target in the presence of a preplasma can be very different from the usual "specular reflection". Thus, the angular distribution of the emitted harmonics deserves close scrutiny as well.

In this paper, we study the reflection and high-harmonic generation by a laser pulse that obliquely hits a solid target preceded by a preplasma. We will do this via 2-dimensional computer simulations, so we can study the harmonics spectrum over a range of angles simultaneously.

Simulations

We have conducted a number of 2-dimensional particle-in-cell (PIC) simulations to investigate the influence of a preplasma on laser reflection and HHG, using the particle-in-cell code Osiris. It has been found that the presence of a preplasma causes laser light to be scattered in many directions ("beam spray"), while the concept of specular reflection no longer has much meaning. The plasma becomes turbulent to such an extent that laser light is reflected from a fairly large range of depths rather than from a single surface. Most tellingly, surface waves that propagate almost perpendicularly to the target-normal direction cause side-scattering of laser light in the same direction, i.e. almost parallel to the target surface, and *towards* the incoming laser beam.

We start from a simulation using a typical set of parameters, which we will refer to as the "reference simulation". The parameters are as follows. Laser pulse: 1.054 micron wave length, 30-degree incidence with respect to the target normal, 250 fs pulse duration, 14 micron spot diameter and $3*10^{18}$ Wcm^{-2} intensity. Target: 8 micron thick, with a maximum density of $80*n_{cr}$blah and a preplasma with a 2 micron scale length. The incoming beam travels purely in the x1 direction and hits the target at an angle of 30 degrees with respect to the target normal. Snapshots of the EM field intensity, the electron density and the Fourier transform of the electric field were taken after 250 fs, i.e. when the pulse had almost completely been reflected by the target. The results of this reference simulation are shown in Figures 1 and 2.

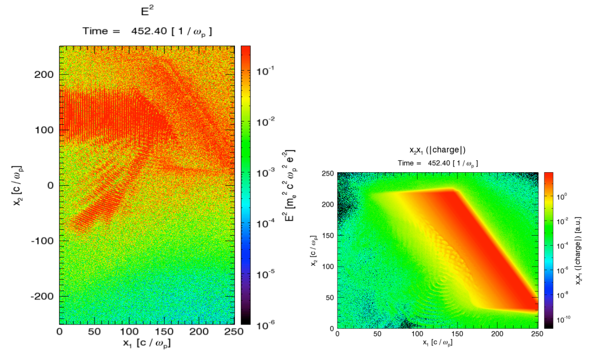

Figure 1. Left: intensity plot of incoming and scattered laser radiation, for the reference simulation at 250 fs. Right: the corresponding electron density.

In Figure 1, the field intensity of the laser beam is shown as it reflects from the target, as well as the target's electron density. While most of the light is reflected in the specular direction, a significant fraction is reflected in directions closer to the target normal and/or the incoming beam. The electron density plot shows significant turbulence in the neighbourhood of the "critical layer", partly caused by interference between the incoming and outgoing EM waves. Also visible are plasma electrons being ejected from the target in well-defined bunches, as predicted by various theoretical models [7-11].

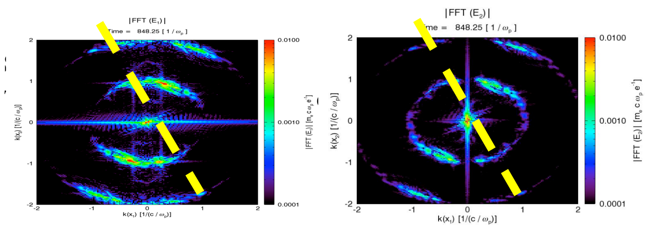

Figure 2: Fourier k-spectra of the components of the electric field of the reference simulation, at 475 fs. The yellow dashed line corresponds to the target angle.

Figure 2 shows the Fourier transforms (wavevector spectrum) of the electric field components, at the "final" simulation time of 475 fs. These transforms confirm that most of the EM waves are reflected at 60 degrees (specular reflection), but that there is significant reflection in other directions. In particular, reflection at angles very close to the target surface can be seen. This corresponds to the turbulence and surface waves seen in the electron density plots.

Starting from this reference simulation, we will now introduce variations. First, we increase the scale length of the preplasma to 4 micron. This leads to more diffuse scattering, in more directions. The peaks for the harmonics in the wave vector spectra are also broader and less clearly defined. Simulation results for this case are displayed in figures 3 and 4.

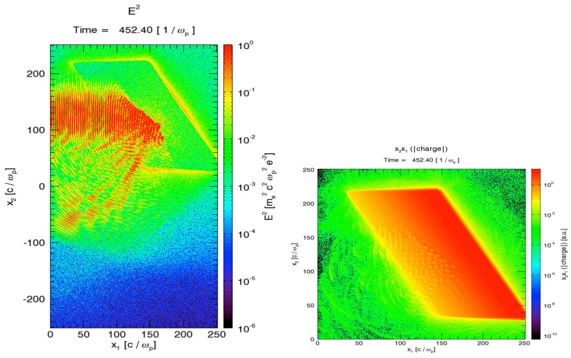

Figure 3: Electric field intensity (left) and plasma electron density (right) for a simulation where the preplasma has a longer scale length (4 micron instead of 2 micron).

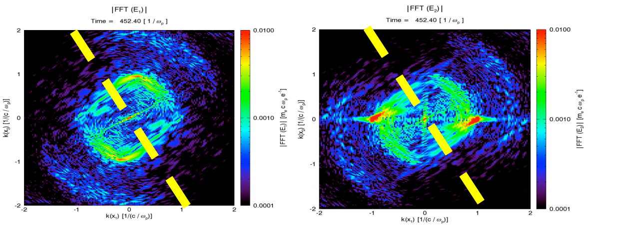

Figure 4: Fourier wave vector spectra for a simulation where the preplasma has a longer scale length (4 micron instead of 2 micron). Note that the radiation is scattered in more directions, while the harmonics are less clearly defined.

The next simulation is again similar to the reference simulation, also having a density scale length of 2 micron, but the laser pulse duration is reduced to 125 fs and its intensity increased to $1.2*10^{19}$ Wcm^{-2}. Simulation results are shown in figures 5 and 6. Compared to the reference simulation, the harmonic generation is more pronounced, and more confined to specific directions. While a strong signal is observed at a 60-degree angle (specular reflection), the strongest signal is observed in a direction almost parallel to the target surface. This is accompanied by strong turbulence and surface waves in the plasma electron density, which are the probable source of the radiation close to the target surface.

The final simulation will combine both the shorter density scale length and the shorter, more intense laser pulse. The simulation results also show a combination of effects caused by either parameter change: the harmonics in the spectrum of the reflected radiation are more "smeared out", and appear in more directions (caused by the longer scale length), while the highest intensity is achieved for radiation propagating almost parallel to the target surface (caused by the higher pulse intensity and shorter duration). Scattered radiation and high harmonics emerge at almost any angle between "incidence" and "reflection", with significant amounts of high harmonic radiation being emitted roughly *towards* the incoming beam.

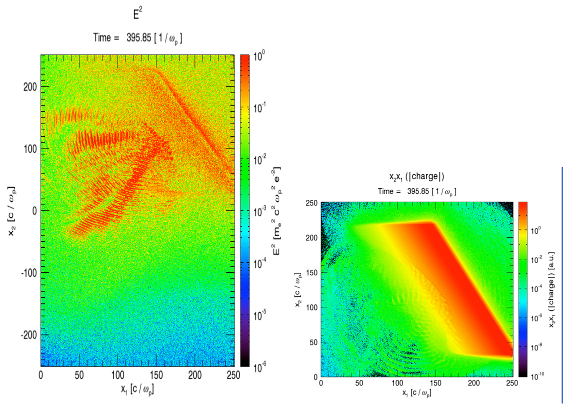

Figure 5: Laser intensity and plasma density profile for the simulation with a shorter, more intense laser pulse (125 fs and $1.2*10^{19}$ Wcm^{-2} respectively).

The plasma density plots show large amounts of plasma electrons being ejected in many directions, again with significant amounts being emitted roughly *towards* the incoming beam.

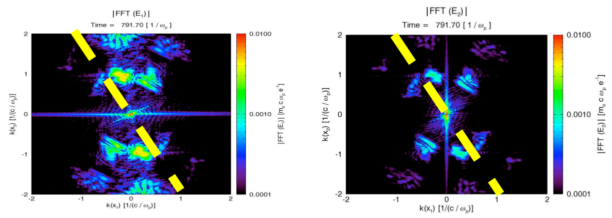

Figure 6: Fourier wave vector spectra for a simulation where the laser pulse is shorter and more intense (125 fs instead of 250 fs). Note that radiation emission parallel to the target surface is now dominant over emission in the "specular" direction.

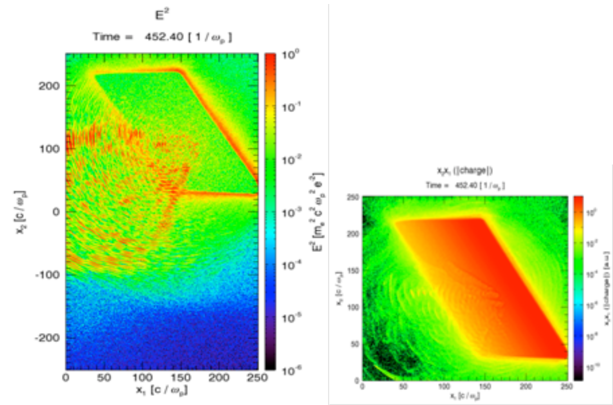

Figure 7: Laser intensity and plasma density profile for the interaction of an intense (10^{19} Wcm^{-2}) short (125 fs) laser pulse with a solid target having a long scale length (4 micron).

Conclusions

In conclusion, we have studied the oblique interaction of a short, intense laser pulse with a solid target and a preplasma extending 10-15 micron in front of that target. By varying the laser pulse intensity and duration, and the preplasma scale length, we could regulate the production of high harmonics. It was found that increasing the density gradient scale length would cause the harmonics of the laser frequency to broaden and become less clearly defined. Increasing the laser intensity would lead to strong plasma turbulence, and the presence of surface waves on the target surface. In turn, this would lead to strong (harmonic) radiation emission in a direction (almost) parallel to the target surface, and ejection of plasma electrons in the same direction. This will have consequences for the study of high harmonic generation in laser-solid interactions. It might also have consequences for the study of the interaction of laser beams with the inner surface of hohlraum targets. This will be addressed in future investigations.

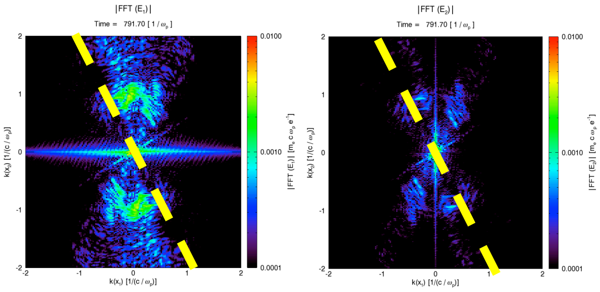

Figure 8: FFT wave number spectra of the E1 and E2 components of the electric field for the simulation of Figure 7.

Acknowledgements

We thank the Osiris consortium for the use of the code Osiris. Simulations have been performed on the Scarf-Lexicon cluster at the CLF.

References

1. B. Dromey et al., Nature Physics 2, 456 (2006).
2. B. Dromey et al., Phys. Rev. Lett. 99, 085001 (2007).
3. Y. Nomura et al., Nature Physics 5, 124 (2009).
4. B. Dromey et al., Nature Physics 5, 146 (2009).
5. B. Dromey et al., Phys. Rev. Lett. 102, 225002 (2009).
6. B. Dromey et al., Nature Physics 8, 804 (2012).
7. S. Gordienko et al., Phys. Rev. Lett. 93, 115002 (2004).
8. S. Gordienko et al., Phys. Rev. Lett. 94, 103903 (2005).
9. T. Baeva, S. Gordienko and A. Pukhov, Phys. Rev. E 74, 046404 (2006).
10. D. An der Bruegge and A. Pukhov, Phys. Plasmas 17, 033110 (2010).
11. T. Baeva *et al.*, Phys. Plasmas **18**, 056702 (2011).

Simulations of synchrotron radiation effects in 10PW+ laser solid interactions

Contact: C.S.Brady@warwick.ac.uk

C. S. Brady
Department of Physics,
University of Warwick,
CV4 7AL, United Kingdom

T. D. Arber
Department of Physics,
University of Warwick,
CV37 9EG, United Kingdom

C. P. Ridgers
Plasma Institute,
University of York,
YO10 5DD, United Kingdom

A. R. Bell
Department of Physics,
University of Oxford,
OX1 3PU, United Kingdom

1 Introduction

Many of the most promising applications of short pulse lasers, such as ion accelerators (Salamin et al. [1]) or igniters for fast ignition (Mourou et al. [2]) require the use of lasers of greater intensity than those currently in existence. At the higher intensities planned for next generation lasers needed for these applications additional physics processes start to become comparable to those common to all plasma physics. The most important of these for 10PW lasers is likely to be the production of high energy photons by non-linear Compton scattering [3] and the associated radiation reaction force on the emitting electrons. Earlier work such as Ridgers et al. [4], Nakamura et al. [5] and Brady et al. [6] have shown that a high fraction of the energy of a next generation laser can be converted into high energy photons, demonstrating that understanding this process, and how it interacts with other plasma physics processes, is essential to understanding how to use 10PW lasers for both basic science and applications. A powerful method for simulating Compton scattering is the semi-classical method of Bell and Kirk [3]. In this method the control parameter that determines the probability of a given electron emitting a Compton scattered photon is $\eta = \gamma/E_S(E_\perp + \beta \times cB)$ where $E_S = m_e^2 c^3/q_e\hbar$ is the Schwinger electric field [7] $E_\perp$ is the local electric field perpendicular to the motion of the electron and the other symbols have their usual meanings. This parameter both encapsulates the strength of laser field required to give a high probability of emitting a high energy photon and the geometrical requirement that there should be a non-zero angle between the motion of an electron and the wave-vector of the laser with which it is interacting. This geometric requirement is easily demonstrated by considering the two limiting cases where a uniform plane linearly polarized laser and a single electron are either co-propagating or counter propagating. In this case, the expression for η can be simplified to $\eta = \gamma E/E_S(1 \pm \beta)$ where the positive and negative branches correspond to the counter-propagating and co-propagating cases respectively. Expanding in γ yields $\eta \approx \frac{E}{2\gamma E_S}$ for the co-propagating case and $\eta \approx (2\gamma - \frac{1}{2\gamma})\frac{E}{E_S} \approx 2\gamma\frac{E}{E_S}$ for the counter-propagating case. This shows that in the high intensity (high γ) limit η is larger than for the counter propagating case by a factor of γ^2. Therefore, in the interaction of a single laser and a target the simple ponderomotive pushing of electrons by the laser will not lead to gamma-ray production since the laser's wave-vector is in the same direction as the electron's motion; there has to be some plasma physics process which leads to a change in either electron motion or laser direction while still retaining high electron gamma factors. The two current basic models for how a 10PW or higher intensity linearly polarized laser would interact with a solid target to produce gamma-rays are skin depth emission (Ridgers et al. [4]) and Reinjected Electron Synchrotron Emission (RESE) (Brady et al. [6]). The further development and characterization of these emission mechanisms and how they affect other processes of interest in the plasma are currently active research areas.

Both of these mechanisms were described based on PIC simulations from the QED PIC code EPOCH [8] by simulating the interaction of a 10^{23}W/cm^2 with an aluminum target of either 1% relativistically corrected critical density for RESE or twice corrected critical density for skin depth emission. Here relativistically corrected critical density is defined as $n_{crit}^{correct} = \omega_{las}^2 \epsilon_0 \gamma m_e/e^2$. ω_{las} is the laser frequency γ is the gamma factor associated with the cycle averaged electron motion and the other symbols have their usual meanings. The simulated EM source was a 1 micron linearly polarized laser with a 6th order super-Gaussian temporal profile with a characteristic width of 25fs and a Gaussian transverse profile with a characteristic scale of 2 microns. The EM source was initialized sufficiently close to the target that laser optic focussing effects were not important.

2 Skin depth emission

The detailed 2D simulation results for skin depth emission show that the gamma ray energy is preferentially generated in a Gaussian blob with a transverse scale comparable to that of the laser (figure 1 a & c). There is a longitudinal modulation of the emission on the order of 10% (figure 1 b). The time profile of gamma ray emission rate is given in figure 2 and shows deep modulation on the laser period. The angular distribution of the emitted gamma rays (figure 3) shows that they are preferentially generated travelling forwards along the laser axis, indicating that they are generated by electrons propagating parallel to the laser axis. Breaking down the laser into forwards and backwards travelling components shows that there is a reflected component with about 45% of the intensity of the laser. Given these constrains it is possible to create a simple model for how skin-depth emission occurs.

The simple model for skin depth emission describes the required configuration for strong emission being given by reflecting the laser from a solid target with an electron number density much greater than the relativistically corrected critical density. The laser penetrates into the target a number of skin depths before reflecting and ponderomotively accelerates electrons forwards. These electrons then interact with the reflected laser to produce gamma-rays. The pool of electrons available for emission is continually replenished since the laser hole-bores into the target. The efficiency of this mechanism is limited by the restricted number of electrons within the skin depth and the reduction of the intensity of the laser as it penetrates into the skin. Detailed analysis of the efficiency of this mechanism are given in Ridgers et al. [4].

3 Reinjected Electron Synchrotron Emission (RESE)

The detailed 2D simulation results for RESE show that the gamma ray energy is also generated with a Gaussian transverse profile with a transverse scale that is initially similar to that of the laser (figure 4 a & c) but, due to the reduced efficiency of relativistic self focussing compared to the higher density skin depth emission target becomes wider as the laser propagates. There is a longitudinal modulation of the emission on the order of 30% (figure 4 b) with a wavelength that is not the same as the laser wavelength. The time profile of gamma ray emission rate is given in figure 5 and shows deep modulation on the breakdown period from Brady et al. [6] ($\tau_{BD} = \epsilon_0 E_0/(cen_e)$ where E_0 is the electric field of the incident laser, n_e is the electron number density of the unperturbed target and all other symbols have their usual meaning). The angular distribution of the emitted gamma rays (figure 6) shows that they are preferentially generated travelling towards the laser on the left hand boundary. The RESE breakdown events are strongly associated with the building up of a space charge field of comparable strength to the laser electron field due to the laser pushing electrons forward. Given these constrains it is possible to create a simple model for how RESE

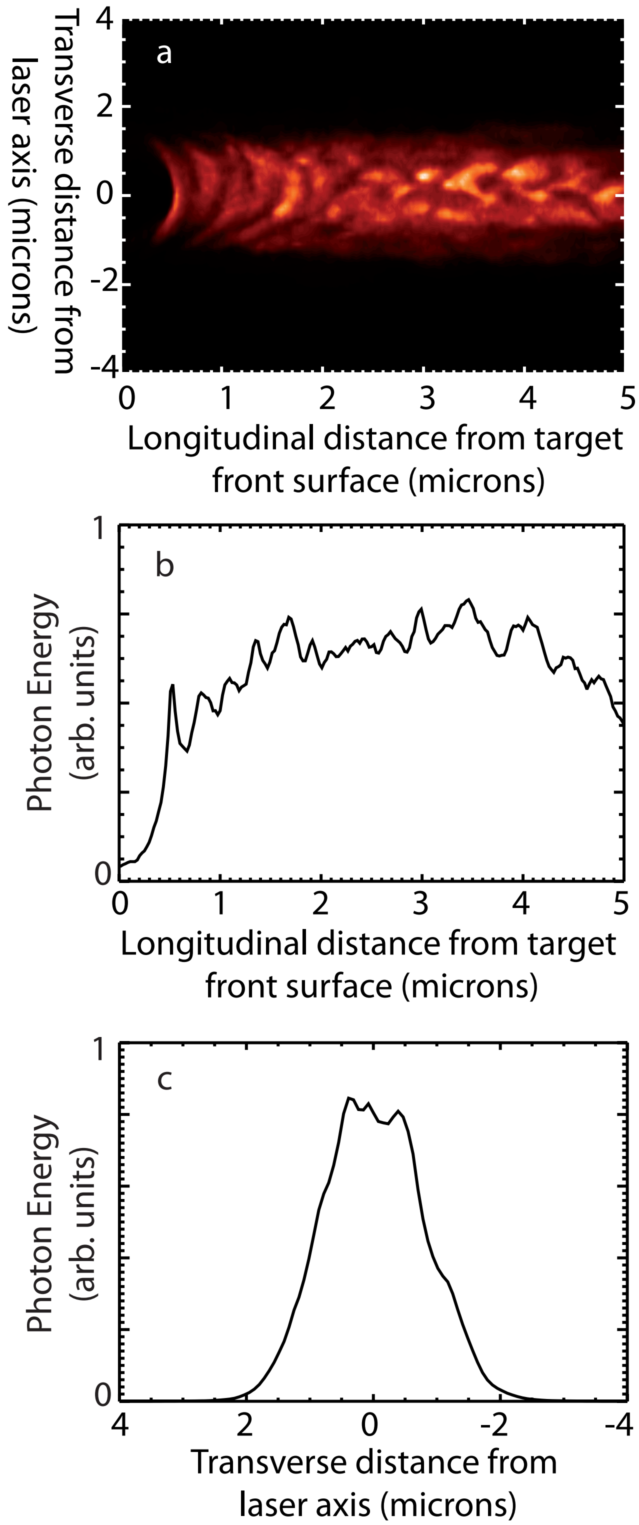

Figure 1: a) Spatial distribution of gamma ray energy production for skin depth emission. b) Longitudinal profile of gamma ray energy. c) Transverse profile of gamma ray energy.

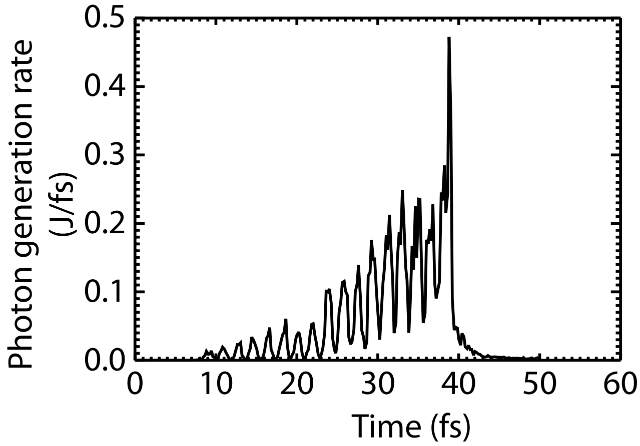

Figure 2: Energy generation rate vs time for skin depth emission.

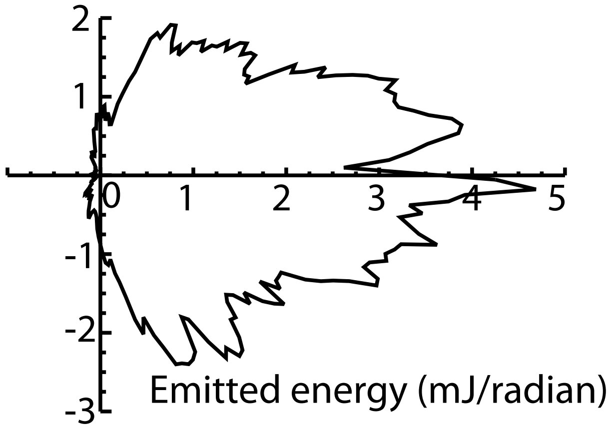

Figure 3: Angular distribution of generated photons in skin-depth emission, showing that electrons are preferentially generated propagating forwards.

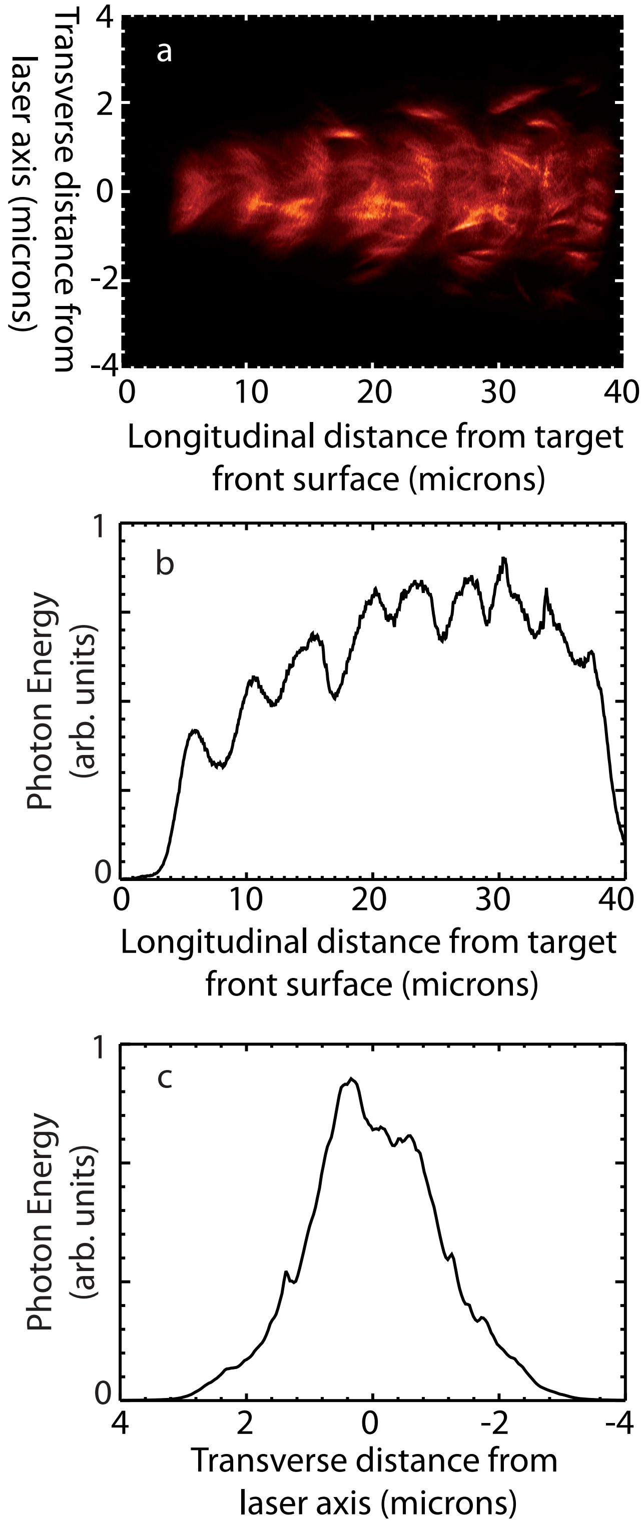

Figure 4: a) Spatial distribution of gamma ray energy production for RESE. b) Longitudinal profile of gamma ray energy. c) Transverse profile of gamma ray energy.

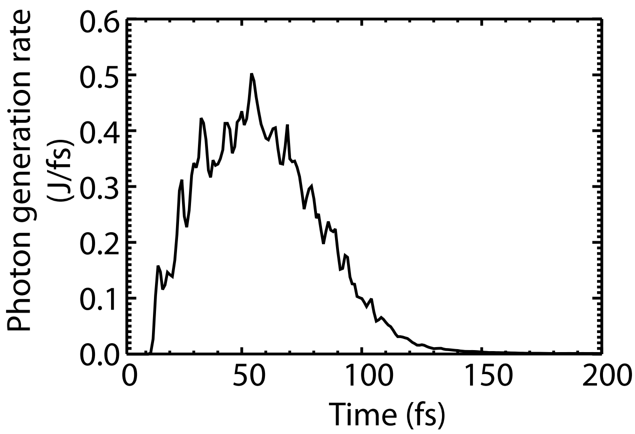

Figure 5: Energy generation rate vs time for RESE.

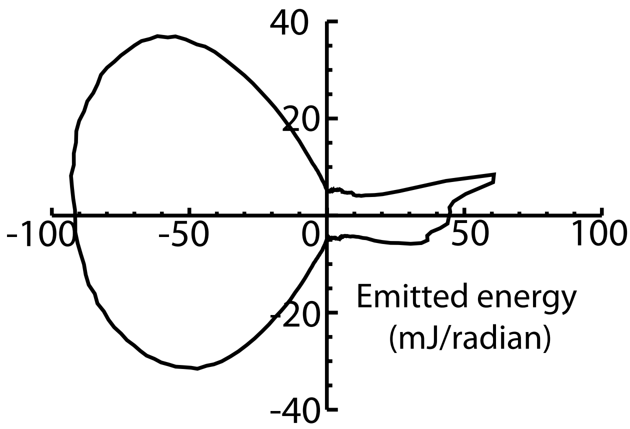

Figure 6: Angular distribution of generated photons in RESE, showing that electrons are preferentially generated propagating backwards.

occurs.

In RESE the situation is more complex. When the laser interacts with a target with a density much lower than relativistically corrected critical density it again ponderomotively accelerates electrons into the target but since the target is underdense the laser continues to propagate leading to the creation of a large space charge field. Eventually the force due to space charge field becomes comparable to the maximum $\mathbf{v} \times \mathbf{B}$ force due to the laser meaning that there is no net longitudinal force on an electron at the head of the laser and a breakdown event occurs. Newly encountered electrons "slip" backwards through the front of the laser into the region behind the laser head to a point behind the maximum in the laser $\mathbf{v} \times \mathbf{B}$. In this region the force due to the space charge field is necessarily greater than the laser's $\mathbf{v} \times \mathbf{B}$ and the electrons are accelerated backwards towards the laser leading to a high η factor and associated gamma-ray production. This mechanism is usually more efficient than skin-depth emission since the electrons continue to cascade backwards until they have neutralized enough of the space charge field to inhibit the acceleration mechanism. Once accelerated these electrons continue to travel backwards since both the Doppler shift of the laser and the high gamma factor associated with the electron's longitudinal motion reduces the $\mathbf{v} \times \mathbf{B}$ force attempting to slow the electron down. This leaves the main deceleration mechanism for the backwards travelling electrons as the radiation reaction force associated with the gamma-ray emission. The emission is characterized by the angular distribution of the produced gamma-rays which are preferentially emitted backwards.

4 Conclusions

Current research shows the existence of two basic mechanisms that can cause the conversion of laser energy into hard photons in a laser solid interaction. These two mechanisms are skin-depth emission which occurs in overdense plasmas and reinjected electron synchrotron emission (RESE) which occurs in underdense plasmas. These two mechanisms are distinctly different, with different angular distributions of emitted gamma rays and different temporal and spatial profiles of energy generation. These differences mean that experimental verification of these two distinct emission modes with next generation lasers is possible.

References

[1] Y. Salamin, Z. Harman, and C. H. Keitel. *Phys. Rev. Lett.*, 100:155004, 2008.

[2] G. A. Mourou, C. L. Labaune, M. Dunne, N. Naumova, and V. T. Tikhonchuk. *Plasma Physics and Controlled Fusion*, 49:B667, 2007.

[3] A. R. Bell and J. G. Kirk. *Physical Review Letters*, 101:200403, 2008.

[4] C. P. Ridgers, C. S. Brady, R. Duclous, J. G. Kirk, K. Bennett, T. D. Arber, A. P. L. Robinson, and A. R. Bell. *Phys. Rev. Lett.*, 108:165006, 2012.

[5] T. Nakamura et al. *Phys. Rev. Lett.*, 108:195001, 2012.

[6] C. S. Brady, C. P. Ridgers, T. D. Arber, A. R. Bell, and J. G. Kirk. *Phys. Rev. Lett.*, 109:245006, 2012.

[7] J. Schwinger. *Physical Review*, 82:664, 1951.

[8] C. S. Brady and T. D. Arber. *Plasma Physics and Controlled Fusion*, 53:015001, 2011.

Ultrafast processes: time-dependent R-matrix methods

Contact *abrown41@qub.ac.uk*

A. C. Brown, H. F. Rey and H. W. van der Hart

Centre for Theoretical Atomic, Molecular and Atomic Physics
Queen's University Belfast,
Belfast, BT7 1NN

Introduction

Recent developments in laser technology have facilitated an unprecedented increase in experimental methods for the analysis of structure and dynamics of matter [1]. The field of 'attosecond physics' (1 as = 1 x 10^{-18} s) has developed around the principle that a short pulse of light can elucidate fast dynamics; thus the synthesis, control and application of ultrashort laser pulses have become areas of intensive research. Recent experiments have allowed sub-cycle measurement of the ionisation rate in krypton [2], multielectron dynamics in xenon [3], and the 'birth time' of tunnel ionised electrons [4].

Central to this research is the process of harmonic generation (HG), wherein a photoionised electron is accelerated in the laser field before recolliding with its parent ion. Upon recollision the electron releases its energy as a photon whose energy is an odd harmonic of the driving laser. This produces an attosecond burst of light or- in the frequency domain- a harmonic 'comb' of frequencies (see Fig.1 for instance). HG is important for two reasons, first as a source of ultrashort coherent radiation and second as a measurement tool: the HG process maps the attosecond scale motion of electrons onto the emitted harmonic spectrum, and with careful analysis the structure and dynamics of the system can be reconstructed.

Therefore there is currently a great deal of interest in ultrafast science, and a consequent need for high quality theoretical data both to direct experiment and to develop our understanding of fundamental processes. In order to accurately model these processes we have developed time-dependent R-matrix (TDRM) theory [5]. The method has previously been applied successfully to assess ionisation dynamics [6], and has recently been extended to account for HG [7]. Here we report the application of the TDRM method to singly ionised argon, and demonstrate both multielectron and multichannel interferences in the harmonic generation process.

The continued development of R-matrix methods has most recently produced the R-matrix with time (RMT) method [8]. Combining techniques from TDRM and the HELIUM code [9], RMT enjoys increased efficiency and is ideally suited to large scale implementations on parallel computer architectures. RMT may be better suited to longer wavelength and higher intensity laser regimes than TDRM. It has recently been used to measure the time delay between photoionisation of $2s$ and $2p$ electrons from neon [10]. Here we report on the application of RMT to ionisation dynamics in carbon.

Time-dependent R-matrix methods

Both the TDRM and RMT method are non-perturbative, *ab initio* methods for the description of a general multi-electron atom or ion in a short, intense laser field. Both apply the standard R-matrix technique in which configuration space is partitioned into two regions with a shared boundary. In the inner region all interactions between all electrons are fully described. In the outer region, an ejected electron is well separated from the atomic core. Thus exchange effects are neglected and the electron moves under the action of the laser field and long range potential of the residual ion. This division allows R-matrix methods to describe multielectron effects, and makes them ideal candidates for parallel computation.

The RMT and TDRM methods use R-matrix basis set techniques to solve the time dependent Schrodinger equation in the inner region and a time propagator to express an updated wavefunction, $\varphi(t_{i+1})$, in terms of the solution at the previous time step, $\varphi(t_i)$. The methods differ in their choice of time propagator, and in their treatment of the outer region. TDRM employs a Crank-Nicolson scheme for time-propagation, and uses a basis set expansion to solve a set of coupled differential equations in the outer region. RMT, on the other hand, uses an Arnoldi time-propagator, and implements a finite difference grid to describe the wavefunction in the outer region. Details of the TDRM and RMT methods can be found in [5] and [8].

Harmonic generation

Harmonic generation arises from the laser induced dipole oscillation. The source of the harmonic radiation is the acceleration of the dipole, but, it is more common to express the harmonic spectrum in terms of the time-dependent expectation value of the dipole length operator:

$$\mathbf{d}(t) \propto \langle \psi(t)|\mathbf{z}|\psi(t)\rangle$$

where **z** is the total position operator along the laser-polarisation axis. The harmonic spectrum is then proportional to

$$\omega^4|\mathbf{d}(\omega)|^2$$

where ω is the frequency of the radiation and $\mathbf{d}(\omega)$ is the Fourier transform of $\mathbf{d}(t)$.

Effect of multiple thresholds on HG in Ar^+

We treat HG from an Ar^+ target in a 390-nm, 4 x 10^{14} Wcm^{-2} laser pulse. Singly ionised argon provides an ideal test of the multielectron and multichannel capabilities of the TDRM method. The three lowest lying, $3s^23p^4$ ionisation thresholds are each within ~2 eV of each other (See Tab. 1), and the higher lying, $3s3p^5$ thresholds allow the contribution of $3s$ electrons. Thus we may expect interference between the $3s$ and $3p$ electrons, and between ionisation channels associated with the close lying thresholds.

Table 1 Ionisation thresholds of Ar^+

Configuration	Term	Energy (eV)
$3s^23p^4$	$^3P^e$	0.0000
	$^1D^e$	1.7370
	$^1S^e$	4.1244
$3s3p^5$	$^3P^o$	14.2138
	$^1P^o$	17.8565

We can open and close ionisation channels by including different combinations of thresholds in the calculation. In the absence of any multichannel effects we would expect that the total harmonic yield should equal the sum of the yields from individual threshold calculations. However, as Fig. 1 shows, this is not the case: a simple addition of individual contributions overestimates the harmonic yield by as much as an order of magnitude in several harmonic peaks. Thus multichannel effects must be included in calculations of HG.

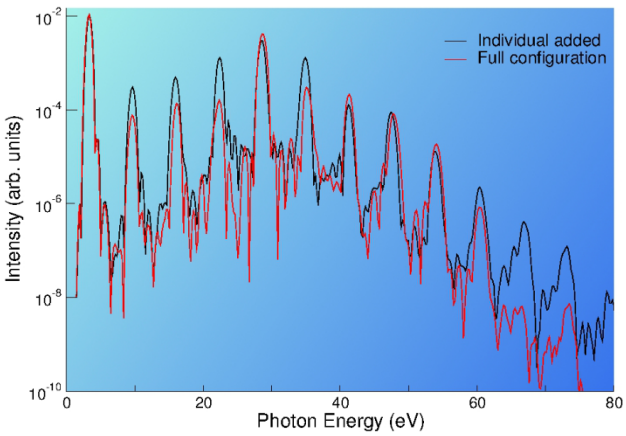

Figure 1 The harmonic yield for Ar^{+} calculated with (red) and without (black) multichannel interference. Multichannel interference leads to order of magnitude in some low energy harmonic peaks.

Furthermore, we can demonstrate the influence of multielectron interference on HG by the inclusion of the $3s3p^5$ thresholds in the calculation. Ionisation towards these thresholds requires the emission of a $3s$ electron, while ionisation towards $3s^23p^4$ involves a $3p$ electron. The interference of these two electrons may have an impact on the harmonic yield [7]. Figure 2 demonstrates this behaviour: including the $3s3p^5$ thresholds in the calculation leads to an order of magnitude reduction in the harmonic spectrum in the energy range of the $3s3p^5$ Rydberg series converging on to these thresholds (~30-50 eV).

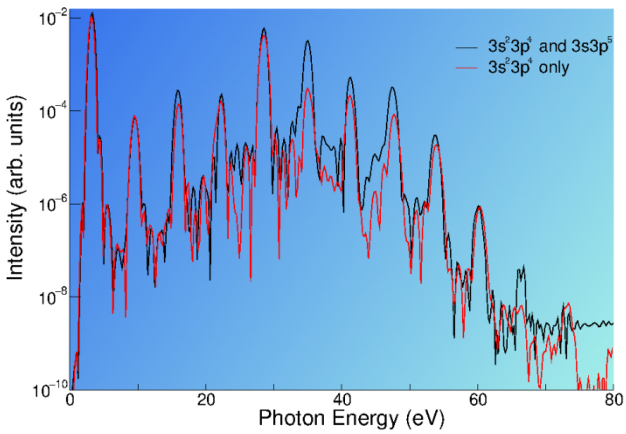

Figure 2 The harmonic yield from Ar^{+} calculated with (red) and without (black) multielectron interference. Interference between 3*s* and 3*p* electrons leads to order of magnitude suppression of harmonic generation in the energy range of the $3s3p^5$ Rydberg series.

Multiphoton ionisation of carbon

In order to investigate the capabilities of the RMT approach, we have embarked on a detailed investigation of multiphoton ionisation of carbon at a laser wavelength of 390-nm. Multiphoton ionisation of C has recently been studied at IR wavelengths, including dynamics after electron detachment from the initial C^- ion [11]. These dynamics occur on the ps timescale, and are much slower than the dynamics associated with multiphoton ionisation, which occur on the fs timescale. Thus, a non-relativistic approach to describe strong-field dynamics in C is appropriate.

Carbon provides a new challenge to the RMT approach. Many residual-ion states are of importance, and hence the size of the calculations is significantly larger than previous calculations. In addition, the C ground state has $^3P^e$ symmetry, as opposed to the $^1S^e$ ground state of noble-gas atoms. The RMT method is designed to describe general atoms, and hence the approach must be able to describe a variety of initial states.

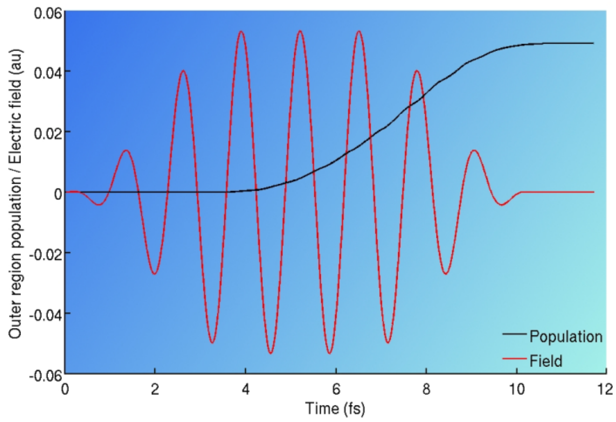

Figure 3 The ionisation yield from C in a 390-nm, 10^{14} Wcm^{-2} pulse as a function of time (black) and the electric field of the laser pulse (red).

The parameters of the calculations are as follows. C is described using the basis set developed by Taylor and Burke [12], which incorporates 8 residual-ion states associated with the $2s^22p$, $2s2p^2$ and $2p^3$ configurations. The laser pulse has a three-cycle $\sin^2$ turn-on, two cycles at peak intensity of 10^{14} Wcm^{-2}, and a three-cycle $\sin^2$ turn-off. In order to obtain a high degree of convergence in the population in the outer-region channels at the end of the calculations, we use a maximum angular momentum $L_{max} = 53$. This value of L_{max} leads to 638 channels in the outer region, and hence the calculations are substantial in size.

As a first demonstration of the results obtained in the present study of C, Fig. 3 shows the population in the outer region as a function of time, as well as the electric field associated with the laser pulse. The figure shows a delay between the peak of the laser pulse and the maximum increase in the population of the outer region. This delay is caused by the size of the inner region which is 25 a_0; I.E. ejected wavepackets are only included in the outer-region population if they are at least a distance of 25 a_0 away from the nucleus. Further analysis of the individual channels demonstrates that 88% of the outer-region population is left in channels associated with the $2s^22p$ $^2P^o$ ground state of C^+ and 11% in the first excited state of C^+, $2s2p^2$ $^4P^e$.

Acknowledgements

ACB acknowledges financial support from DELNI through the programme for government. HFR is supported by the Marie Curie Initial Training Network, CORINF. HvdH is supported by the ESPRC through grant number EP/G055416/1. The authors would like to thank Dr Jonathan Parker for valuable discussions.

References

1. P. B. Corkum and F. Krausz, *Nat. Phys*. **3** 381 (2007)
2. A. Wirth *et al. Science*, **334** 195 (2011)
3. A. D. Shiner *et al. Nat. Phys.* **7** 464 (2011)
4. D. Shafir *et al. Nature,* **484** 343 (2012)
5. M. A. Lysaght, *et al. Phys. Rev.* **A**, **79** 053411 (2009)
6. M. A. Lysaght, *et al. Phys. Rev. Lett.* **102** 193001 (2009)
7. A. C. Brown, *et al. Phys. Rev. Lett.* **108** 063006 (2012)
8. L. R. Moore, *et al. J. Mod. Opt.* **58** 1132 (2011)
9. J. S. Parker, *et al. Phys. Rev. Lett.* **96** 133001 (2006)
10. L. R. Moore, *et al. Phys. Rev.* **A**, **84** 061404 (2011)
11. H. Hultgren, *et al. Phys. Rev.* **A, 87** 031404R (2013)
12. P. G. Burke and K. T. Taylor, *J. Phys. B: At. Mol. Phys*. **12** 2971 (1979)

Recent developments in Lorentz-Abraham-Dirac fluid theory

Contact *d.burton@lancaster.ac.uk*

D.A. Burton
Physics Department, Lancaster University
& The Cockcroft Institute, Daresbury, UK

1 Introduction

Contemporary advances in ultra-intense laser facilities have driven the recent surge of interest in the collective behaviour of charged matter in extreme conditions, and a particularly vexing topic in that context concerns the coupling of an electron to its own radiation field. An accelerating electron emits electromagnetic radiation, and the energy and momentum carried away by the electromagnetic field must be accounted for. In most practical cases, the Lorentz force on an electron, due to an applied electromagnetic field, is considerably larger than the force due to the electron's emission and the effect of the recoil due to the emitted radiation is negligible or can be adequately represented using simple physical reasoning. Although such arguments avoid the difficulties that plague more comprehensive analyses, the parameter regimes promised by forthcoming ultra-intense laser facilities ensure that more fundamental considerations are now of practical necessity. For example, ELI [1] is expected to operate with intensities $10^{23}\mathrm{W/cm}^2$ and electron energies in the GeV range, at which level the radiation reaction force becomes comparable to, and can even exceed, the applied force due to the laser field. This article is a brief introduction to a recently established method for modelling the collective behaviour of charged matter including radiation reaction. Further details and applications may be found in Refs. [2,3].

One of the most notorious equations in physics was developed by Dirac [4] to describe a classical point electron's radiative self-force. The Lorentz-Abraham-Dirac (LAD) equation is a fully relativistic description of a structureless point particle in an applied electromagnetic field F_{ab} and has the form

$$\frac{d^2x^a}{d\lambda^2} = -\frac{q}{m}F^a{}_b\frac{dx^b}{d\lambda} + \tau\Delta^a{}_b\frac{d^3x^b}{d\lambda^3} \tag{1}$$

with q the particle's charge, m the particle's rest mass, $\tau = q^2/6\pi m$ in Heaviside-Lorentz units with $c = \epsilon_0 = \mu_0 = 1$, and the tensor $\Delta^a{}_b$ is

$$\Delta^a{}_b = \delta^a_b + \frac{dx^a}{d\lambda}\frac{dx_b}{d\lambda}. \tag{2}$$

For an electron, $q = -e < 0$. The Einstein summation convention is used throughout the present article, indices are raised and lowered using the metric tensor $\eta_{ab} = \mathrm{diag}(-1,1,1,1)$ and lowercase Latin indices range over $0,1,2,3$. The particle's 4-velocity $dx^a/d\lambda$ is normalized as follows:

$$\frac{dx^a}{d\lambda}\frac{dx_a}{d\lambda} = -1 \tag{3}$$

where λ is the particle's proper time.

Dirac derived (1) for an electron by appealing to the conservation condition on the stress-energy-momentum tensor (see Ref. [5] for a recent discussion of the derivation). Dirac's approach requires a regularization of the electron's singular contribution to the stress-energy-momentum tensor followed by a renormalization of the electron's rest mass. The procedure leads to the third-order term in (1), which is the source of the famous pathological behaviour exhibited by solutions to the LAD equation (see Ref. [6] for a recent discussion).

The standard approach to ameliorating the problems with the LAD equation is to replace the third-order terms in (1) (radiation reaction force) with the derivative of the first term on the right-hand side of (1) (the applied Lorentz force). This procedure is justifiable if the radiation reaction force is a small perturbation to the Lorentz force, and it yields the Landau-Lifshitz (LL) equation:

$$\begin{aligned}\frac{d^2x^a}{d\lambda^2} =& -\frac{q}{m}F^a{}_b\frac{dx^b}{d\lambda} - \tau\frac{q}{m}\partial_c F^a{}_b\frac{dx^b}{d\lambda}\frac{dx^c}{d\lambda}\\ &+ \tau\frac{q^2}{m^2}\Delta^a{}_bF^b{}_cF^c{}_d\frac{dx^d}{d\lambda}.\end{aligned} \tag{4}$$

Unlike the LAD equation, the LL equation is second order in derivatives in λ and its solutions are free from pathologies.

Recent years have seen a substantial growth of interest in kinetic theories incorporating radiation reaction (see, for example, Refs. [7, 8]), and almost all such theories are based on the LL equation from the outset. However, the briefest of glances at (1) and (4) suggests that a degree of mathematical clarity (with concomitant physical insight) is likely to be gained by starting with a kinetic theory based on the LAD equation. Of course, procedures for extracting physically acceptable behaviour from the LAD kinetic theory must be introduced during the analysis.

Remarkably, until recently [2], very little has appeared in the literature concerning a fully relativistic many-body system governed by the LAD equation. In addition, what can be found [9] appears to lead to physically inconsistent results (see Ref.[2] for a discussion of this point). Perhaps one of the reasons why the LAD equation appears to have been neglected in the physics literature is the necessary, but unconventional, introduction of the notion of a 'phase' space encoding acceleration as well as velocity and spacetime events. By employing the appropriate geometrical machinery, we recently showed [2] how to construct a Vlasov equation based on the LAD equation.

2 Kinetic theory

As shown in Ref. [2], the LAD equation may be written in first-order form as

$$\frac{dx^a}{d\lambda} = \dot{x}^a, \tag{5}$$

$$\frac{dv^\mu}{d\lambda} = a^\mu, \tag{6}$$

$$\frac{da^\mu}{d\lambda} = \ddot{x}^a\ddot{x}_a v^\mu + \frac{1}{\tau}\left(a^\mu + \frac{q}{m}F^\mu{}_a\dot{x}^a\right) \tag{7}$$

in terms of the proper velocity $\boldsymbol{v} = (v^1, v^2, v^3)$ and acceleration $\boldsymbol{a} = (a^1, a^2, a^3)$ in a 10-dimensional 'phase' space (x^a, v^μ, a^ν) where lowercase Greek indices range over $1, 2, 3$. The shorthand $\dot{x}^0 = \sqrt{1+\boldsymbol{v}^2}$, $\ddot{x}^0 = a^\mu v_\mu/\sqrt{1+\boldsymbol{v}^2}$, $\dot{x}^\mu = v^\mu$, $\ddot{x}^\mu = a^\mu$ have been used, and the parametrization in terms of $\boldsymbol{v}$ and $\boldsymbol{a}$ has been chosen to satisfy the constraints $\dot{x}^a\dot{x}_a = -1$, $\ddot{x}^a\dot{x}_a = 0$ arising from (3) and its first derivative with respect to λ. Greek indices are raised and lowered using the Kronecker delta $\delta_{\mu\nu}$.

From a geometrical perspective, the Vlasov equation may be understood as the preservation of a differential form of maximal degree along the flow of single-particle orbits. A 1-particle distribution $f = f(x, \boldsymbol{v}, \boldsymbol{a})$ may be naturally extracted from that differential form [2] leading to

$$Lf + \frac{3}{\tau}f = 0 \tag{8}$$

where L is the Liouville operator

$$L = \dot{x}^a\frac{\partial}{\partial x^a} + a^\mu\frac{\partial}{\partial v^\mu} + \left[\ddot{x}^a\ddot{x}_a v^\mu + \frac{1}{\tau}\left(a^\mu + \frac{q}{m}F^\mu{}_a\dot{x}^a\right)\right]\frac{\partial}{\partial a^\mu}. \tag{9}$$

The second term on the left-hand side of (8) may be understood as a consequence of losses due to radiation (for more details see Ref. [2]).

Maxwell's equations are

$$\partial_a F_{bc} + \partial_c F_{ab} + \partial_b F_{ca} = 0, \tag{10}$$

$$\partial_a F^{ab} = q\, N^b + J^b_{\text{ext}} \tag{11}$$

with $\partial_a \equiv \partial/\partial x^a$ and N^a the number 4-current of the electron fluid,

$$N^a(x) = \int \dot{x}^a f(x, \boldsymbol{v}, \boldsymbol{a})\,\frac{d^3v\, d^3a}{1+\boldsymbol{v}^2} \tag{12}$$

where $\boldsymbol{v}^2 = v^\mu v_\mu$. The presence of the factor $1+\boldsymbol{v}^2$ in (12) and the second term in (8) are related, as discussed in Ref. [2], and J^a_{ext} is an external current.

Almost all solutions to (8) will exhibit pathological behaviour inherited from the LAD equation. However, physically acceptable solutions may be extracted from (8) using the ansatz [2]

$$f(x, \boldsymbol{v}, \boldsymbol{a}) = \sqrt{1+\boldsymbol{v}^2}\,g(x, \boldsymbol{v})\,\delta^{(3)}\big(\boldsymbol{a} - \boldsymbol{A}(x, \boldsymbol{v})\big) \tag{13}$$

where $\delta^{(3)}$ is the 3-dimensional Dirac delta and $g(x, \boldsymbol{v})$, $A(x, \boldsymbol{v})$ are assumed to have a power-series dependence on τ:

$$g(x, \boldsymbol{v}) = \sum_{n=0}^{\infty} g_{(n)}(x, \boldsymbol{v})\,\tau^n, \tag{14}$$

$$\boldsymbol{A}(x, \boldsymbol{v}) = \sum_{n=0}^{\infty} \boldsymbol{A}_{(n)}(x, \boldsymbol{v})\,\tau^n. \tag{15}$$

The subspace $(x, \boldsymbol{v}) \mapsto (x, \boldsymbol{v}, \boldsymbol{a} = \boldsymbol{A}(x, \boldsymbol{v}))$ contains physical solutions to the LAD equation and $g = g(x, \boldsymbol{v})$ is a 1-particle distribution on 7-dimensional event-velocity space. The factor $\sqrt{1+\boldsymbol{v}^2}$ ensures that g is normalized in the expected manner; plugging (13) into (12) yields the usual expression for the number 4-current in relativistic fluid theory:

$$N^a(x) = \int \dot{x}^a g(x, \boldsymbol{v})\,\frac{d^3v}{\sqrt{1+\boldsymbol{v}^2}}. \tag{16}$$

Equations (13, 8) lead to the coupled system of equations

$$\dot{x}^a\frac{\partial A^\mu}{\partial x^a} + A^\nu\frac{\partial A^\mu}{\partial v^\nu} = A^a\,A_a\,v^\mu + \frac{1}{\tau}(A^\mu + \frac{q}{m}F^\mu{}_a\dot{x}^a), \tag{17}$$

$$\dot{x}^a\frac{\partial g}{\partial x^a} + \sqrt{1+\boldsymbol{v}^2}\frac{\partial}{\partial v^\mu}\left(\frac{g\,A^\mu}{\sqrt{1+\boldsymbol{v}^2}}\right) = 0 \tag{18}$$

for g and $\boldsymbol{A}$, with $A^0 = v^\mu A_\mu/\sqrt{1+\boldsymbol{v}^2}$.

Analysis of (17, 18) shows that neglecting $\mathcal{O}(\tau)$ terms in (14, 15) leads to the usual relativistic Vlasov equation without the self-force. Neglecting $\mathcal{O}(\tau^2)$ leads to the kinetic theory of the LL equation as found in, for example, Refs. [7,8]. Furthermore, it may be shown that the entropy 4-current s^a defined as [3]

$$s^a = -k_B\int \dot{x}^a\,g\ln(g)\,\frac{d^3v}{\sqrt{1+\boldsymbol{v}^2}} \tag{19}$$

satisfies

$$\partial_a s^a = -\tau\frac{k_B}{m}\left(\mathcal{J}_a(\mathcal{J}^a + J^a_{\text{ext}}) + 4\frac{q^2}{m^2}\mathcal{T}_{ab}\mathcal{S}^{ab}\right) + \mathcal{O}(\tau^2) \tag{20}$$

where

$$\mathcal{J}^a = q\int \dot{x}^a g|_{\tau=0}\,\frac{d^3v}{\sqrt{1+\boldsymbol{v}^2}}, \tag{21}$$

$$\mathcal{S}^{ab} = m\int \dot{x}^a\dot{x}^b g|_{\tau=0}\frac{d^3v}{\sqrt{1+\boldsymbol{v}^2}}, \tag{22}$$

$$\mathcal{T}^{ab} = \left(F^{ac}F^{b}{}_{c} - \frac{1}{4}\eta^{ab}F_{cd}F^{cd}\right)\Big|_{\tau=0}. \tag{23}$$

The vector field $\mathcal{J}^a$ is the electric 4-current of the electron fluid, $\mathcal{S}^{ab}$ is the stress-energy-momentum tensor of the electron fluid and $\mathcal{T}^{ab}$ is the stress-energy-momentum tensor of the electromagnetic field F_{ab}, without the effects of radiation reaction.

Equation (20) was previously introduced in [7] in a different form, but its physical interpretation and mathematical elegance were less apparent there. The scalar field $\mathcal{T}_{ab}\mathcal{S}^{ab} \geq 0$ because $\mathcal{T}_{ab}\,\dot{x}^a\dot{x}^b \geq 0$, whereas $\mathcal{J}^a$ is timelike (or zero) and so, in the absence of the external current J^a_{ext}, the terms on the right-hand side of (20) naturally split into two contributions according on their signs. The scalar field $\mathcal{J}_a\mathcal{J}^a$ drives heating, whereas the scalar field $\mathcal{T}_{ab}\mathcal{S}^{ab}$ drives cooling.

3 Fluid theory

Kinetic theories are not always the most convenient tools for analytical investigation of the collective dynamics of charged matter (whether or not they include the radiative self-force). Furthermore, extensive computational resources are usually required to numerically solve the integro-differential systems of equations found in such theories.

In practice, the 1-particle distribution f will usually contain more information than is needed and one may replace the Vlasov equation with a fluid theory that encodes f using a subset of its velocity-acceleration moments. In general, macroscopic fluid theories are more analytically amenable and less computationally demanding than their kinetic counterparts, and their relationship with experiment is more immediate.

Implementing (13) is not straightforward if the final PDE system is to exhibit manifest Lorentz covariance. However, it turns out that LAD-induced pathological behaviour may be ameliorated without (13); instead, a procedure analogous to the extraction of the LL equation from the LAD equation is used.

Using the notation first introduced in Ref. [10], the *natural* moments of f are tensor fields on spacetime defined as

$$S^{a_1\ldots a_\ell:b_1\ldots b_n}(x) = \int \dot{x}^{a_1}\ldots\dot{x}^{a_\ell} \times \ddot{x}^{b_1}\ldots\ddot{x}^{b_\ell} f(x,\boldsymbol{v},\boldsymbol{a})\frac{d^3v\,d^3a}{1+\boldsymbol{v}^2}. \tag{24}$$

Indices associated with velocity are located to the left of the colon in $S^{a_1\ldots a_\ell:b_1\ldots b_n}$, whereas those associated with acceleration are located to the right of the colon. An absence of indices will be denoted by $\emptyset$ as follows:

$$S^{\emptyset} = \int f\,\frac{d^3v\,d^3a}{1+\boldsymbol{v}^2}, \tag{25}$$

$$S^{a_1\ldots a_\ell:\emptyset} = \int \dot{x}^{a_1}\ldots\dot{x}^{a_\ell} f\,\frac{d^3v\,d^3a}{1+\boldsymbol{v}^2}, \tag{26}$$

$$S^{\emptyset:b_1\ldots b_n} = \int \ddot{x}^{b_1}\ldots\ddot{x}^{b_n} f\,\frac{d^3v\,d^3a}{1+\boldsymbol{v}^2}. \tag{27}$$

Natural moments with an immediate physical interpretation include the number 4-current $N^a = S^{a:\emptyset}$ and stress-energy-momentum tensor $mS^{ab:\emptyset}$ of the electron fluid. The scalar field $S^{\emptyset}$ is the relativistic enthalpy.

The Vlasov equation (8) may be recast as the infinite hiearchy of tensor equations

$$\partial_a S^{a:\emptyset} = 0, \tag{28}$$

$$\partial_a S^{ab:\emptyset} - S^{\emptyset:b} = 0, \tag{29}$$

$$\partial_a S^{a:b} - S^{b:c}{}_{c} - \tau^{-1}\left(S^{\emptyset:b} + \frac{q}{m}F^{b}{}_{c}S^{c:\emptyset}\right) = 0, \tag{30}$$

$$\partial_a S^{abc:\emptyset} - S^{b:c} - S^{c:b} = 0, \tag{31}$$

$$\partial_a S^{ab:c} - S^{\emptyset:bc} - S^{bc:d}{}_{d} - \tau^{-1}\left(S^{b:c} + \frac{q}{m}F^{c}{}_{d}\,S^{bd:\emptyset}\right) = 0, \tag{32}$$

$$\partial_a S^{a:bc} - S^{b:cd}{}_{d} - S^{c:bd}{}_{d} - \tau^{-1}\left(2S^{\emptyset:bc} + \frac{q}{m}F^{b}{}_{d}\,S^{d:c} + \frac{q}{m}F^{c}{}_{d}\,S^{d:b}\right) = 0, \tag{33}$$

$$\ldots \tag{34}$$

on spacetime, where ... indicates equations whose first term $\partial_{a_1}S^{a_1\ldots a_\ell:b_1\ldots b_n}$ satisfies $\ell + n > 3$. Furthermore, the identities $\ddot{x}^a\dot{x}_a = 0$ and $\dot{x}^a\dot{x}_a = -1$ lead to the constraints

$$S^{a}{}_{a}{}^{:\emptyset} = -S^{\emptyset}, \tag{35}$$

$$S^{a:}{}_{a} = 0, \tag{36}$$

$$S^{ab}{}_{b}{}^{:\emptyset} = -S^{a:\emptyset}, \tag{37}$$

$$S^{a}{}_{a}{}^{:b} = -S^{\emptyset:b}, \tag{38}$$

$$S^{ab:}{}_{a} = 0, \tag{39}$$

$$S^{a:}{}_{ab} = 0, \tag{40}$$

$$\ldots \tag{41}$$

where ... indicates equations containing natural moments with rank greater than 3.

For practical purposes, a finite set of equations must be chosen from the infinite sequences (28-34), (35-41) and this may be achieved by introducing the bulk velocity U^a, bulk acceleration A^a

$$U^a = S^{a:\emptyset}/S^{\emptyset}, \tag{42}$$
$$A^a = S^{\emptyset:a}/S^{\emptyset} \tag{43}$$

and the *centred* moments

$$R^{a_1\dots a_\ell:b_1\dots b_n}(x) = \int \bigg(\dot{x}^{a_1} - U^{a_1}(x)\bigg)\dots \times \bigg(\dot{x}^{a_\ell} - U^{a_\ell}(x)\bigg)\bigg(\ddot{x}^{b_1} - A^{b_1}(x)\bigg)\dots \times \bigg(\ddot{x}^{b_n} - A^{b_n}(x)\bigg) f(x,\boldsymbol{v},\boldsymbol{a})\,\frac{d^3a\,d^3v}{1+\boldsymbol{v}^2} \tag{44}$$

followed by the assumption that all centred moments of a particular rank or greater are negligible.

The rank 1 centred moments $R^{a:\emptyset}$, $R^{\emptyset:a}$ trivially vanish due to the definitions of U^a, A^a, $S^{a:\emptyset}$, $S^{\emptyset:a}$. Setting all centred moments of rank 2 or greater to zero is equivalent to demanding that the electron distribution has zero spread in velocity and acceleration, and this assumption collapses (28-34), (35-41) to the LAD equation for U^a (see Ref. [10] for details).

A fluid modelling a collection of electrons whose distribution has a small, but non-negligible, spread about the bulk velocity and bulk acceleration is more subtle to construct. Following an approach analogous to the scheme introduced by Amendt [11] for non-radiating fluids, we introduce the scalar field $\epsilon = \sqrt{1 + U^aU_a}$ and hypothesize that $R^{a_1\dots a_\ell:b_1\dots b_n} = \mathcal{O}(\epsilon^{\ell+n})$ with $S^{\emptyset} = \mathcal{O}(\epsilon^0)$, $U^a = \mathcal{O}(\epsilon^0)$, $A^a = \mathcal{O}(\epsilon^0)$. Thus, $R^{ab:\emptyset} = \mathcal{O}(\epsilon^2)$, $R^{a:b} = \mathcal{O}(\epsilon^2)$, $R^{\emptyset:ab} = \mathcal{O}(\epsilon^2)$ and inspection reveals that the total number of independent components of (28-33) matches the total number of independent components of the variables $S^{\emptyset}$, U^a, A^a, $R^{ab:\emptyset}$, $R^{a:b}$, $R^{\emptyset:ab}$ if all $\mathcal{O}(\epsilon^3)$ terms in (28-33) are set to zero. However, in general, it is not possible to find solutions to the resulting field equations that also satisfy the constraints (35-40) with all $\mathcal{O}(\epsilon^3)$ terms set to zero in those constraints. Instead, inspired by previous work on non-radiating fluids [12], we impose the weaker condition that (35-40) need only be satisfied to $\mathcal{O}(\epsilon^3)$, which leads to

$$R^a{}_a{}^{:\emptyset} + S^{\emptyset}(1 + U^aU_a) = \mathcal{O}(\epsilon^3), \tag{45}$$
$$R^{a:}{}_a + S^{\emptyset}U^aA_a = \mathcal{O}(\epsilon^3), \tag{46}$$
$$U^bR^a{}_b{}^{:\emptyset} = \mathcal{O}(\epsilon^3), \tag{47}$$
$$U^aR_a{}^{:b} = \mathcal{O}(\epsilon^3), \tag{48}$$
$$U^aR^{b:}{}_a + A_aR^{ab:\emptyset} = \mathcal{O}(\epsilon^3), \tag{49}$$
$$U^aR^{\emptyset:}{}_{ab} + A_aR^{a:}{}_b = \mathcal{O}(\epsilon^3). \tag{50}$$

A *warm* fluid model including the radiative self-force is obtained by setting to zero all terms that are $\mathcal{O}(\epsilon^3)$ in (28-33), and solutions to the resulting system of PDEs are sought that satisfy (45-50) [3]. Pathological behaviour inherited from the LAD equation can be removed from the resulting system of PDEs by following the same iterative procedure used to derive the LL equation (4) from the LAD equation (1).

Acknowledgements

The author is a member of the ALPHA-X consortium funded under EPSRC grant EP/J018171/1, and is supported by the Cockcroft Institute of Accelerator Science and Technology (STFC grant ST/G008248/1).

References

[1] http://www.extreme-light-infrastructure.eu/

[2] A. Noble, D.A. Burton, J. Gratus and D.A. Jaroszynski, J. Math. Phys. **54**, 043101 (2013)

[3] D.A. Burton, A.C. Carr, J. Gratus and A. Noble, Proc. SPIE **8779**, 1X (2013)

[4] P.A.M. Dirac, Proc. Roy. Soc. A **167**, 148 (1938)

[5] M.R. Ferris and J. Gratus, J. Math. Phys. **52** 092902 (2011)

[6] R.T. Hammond, Phys. Rev. A **81** 062104 (2010)

[7] M. Tamburini *et al.*, Nucl. Instrum. Methods A **653**, (1) 181 (2011)

[8] G. Lehmann and K.H. Spatschek, Phys. Rev. E **85**, 056412 (2012)

[9] R. Hakim and A. Mangeney, J. Math. Phys. **9** 116 (1968)

[10] A. Noble, *et al.* Proc. SPIE **8079** 0L (2011)

[11] P. Amendt, Phys. Fluids **29** 5 1458 (1986)

[12] H. Weitzner in *Relativistic Fluid Dynamics*, Lecture Notes in Mathematics **1385** (ed. A. Anile, Y. Choquet-Bruhat) p. 211, Springer-Verlag (1987)

The role of collisionless electrostatic shocks in laser-plasmas

Contact: rac@st-andrews.ac.uk

R.A. Cairns
School of Mathematics and Statistics
University of St Andrews
St Andrews, Fife, KY16 9SS, United Kingdom

R. Bingham, P. Norreys and R. Trines
Central Laser Facility,
STFC Rutherford Appleton Laboratory,
Didcot, OX11 0QX, United Kingdom

Some recent experiments on the interaction of high power lasers with plasmas have shown evidence of shock-like structures with very high electric fields existing over very short distances[1, 2]. Amendt et al [3] say that data from proton radiography in inertial confinement fusion capsules suggest the existence of fields of more than 10^{10} Vm^{-1} over distances of the order of 10-100 nm. In a more recent paper Amendt et al [4] suggest that barodiffusion (ie pressure-driven diffusion) may be a possible explanation, but this does not seem to produce very short length scales. Another relevant recent paper is that of Haberberger et al [5] who describe experiments in which collisionless shocks generate high energy proton beams with small energy spread. Here we show that a shock structure can be produced by having a finite ion temperature so that some ions are reflected by the potential maximum at the shock. This produces the asymmetry between the upstream and downstream sides which destroys the familiar symmetrical ion sound solitary wave. In a collisionless unmagnetized plasma the reflected ions simply travel upstream unimpeded. Early observations of electrostatic shocks were made by Taylor et al [7] showing the kind of structure we describe, a potential ramp followed by downstream oscillations, at low Mach numbers. Computer simulations by Forslund and Freidberg [8] later showed shocks, with more complicated dissipative structures at higher Mach number. More recent PIC simulations by Fiuza et al [9] also report more complex turbulent shocks at higher Mach numbers than the ones used in this paper. Some later work on this problem has been carried out by Smirnovskii [10, 11].

Consider collisionless ions flowing into a region where the potential increases from zero to some positive value $\phi_{\max}$. Taking the incoming ions to have a Maxwellian distribution with average velocity V the density where the potential is ϕ, normalised to the initial density of the incoming flow is $n_i(\phi, \phi_{\max})$

$$n_i = \frac{1}{\sqrt{2\pi}}\left[\int_0^\infty \exp\left[-\frac{\left(\sqrt{v^2+2\phi}-V\right)^2}{2}\right] dv + \int_0^{\sqrt{2(\phi_{\max}-\phi)}} \exp\left[-\frac{\left(\sqrt{v^2+2\phi}-V\right)^2}{2}\right] dv\right] \tag{1}$$

with ion velocities normalised to the thermal velocity $V_i = \sqrt{2\kappa T_i}$ and the potential to $m_i V_i^2/(Ze)$ with Z the ion charge state, and $\kappa = k/m_i$ where k is Boltzmann's constant and m_i is the ion mass. We assume that V is sufficiently large that the backward part of the Maxwellian in the shock frame is negligible. The second term here takes account of particles reflected from the potential maximum. For the electrons we assume thermal equilibrium in the potential, with the electrons flowing to produce charge equilibrium far upstream where the potential tends to zero, so that

$$n_e(\phi, \phi_{\max}) = n_i(0, \phi_{\max}) \exp\left(\frac{\phi}{T}\right) \tag{2}$$

where $T = ZT_e/T_i$.

We introduce the Sagdeev potential [6]

$$\Phi(\phi, \phi_{\max}) = \int_0^\phi \left[n_i(\phi', \phi_{\max}) - n_e(\phi', \phi_{\max})\right] d\phi' \tag{3}$$

so that Poisson's equation is

$$\frac{d^2\phi}{dx^2} = -\frac{\partial \Phi}{\partial \phi}, \tag{4}$$

analogous to the equation of motion of a particle in a potential.

The condition that the value of $\phi_{\max}$ be consistent with the system dynamics is that

$$\Phi(\phi_{\max}, \phi_{\max}) = 0, \tag{5}$$

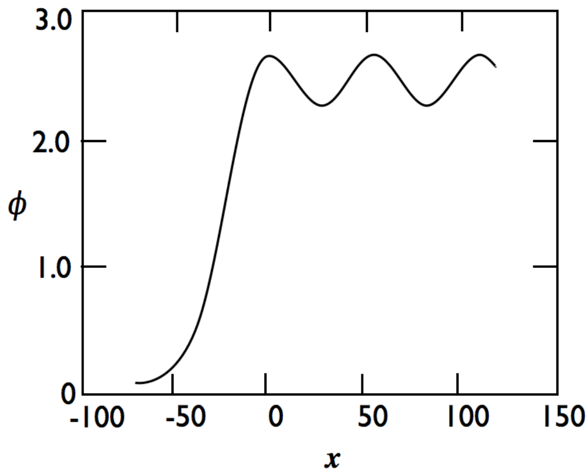

Figure 1: The potential for the D-T plasma with $T_e = 20$ and $V = 4.75$.

determining $\phi_{\max}$. The dimensionless parameters governing the system are V and T and it can soon be found that not all combinations of these yield a system in which the Sagdeev potential has a zero for positive ϕ and is negative in the interval $(0, \phi_{\max})$. We have found that a value of T of around 15 or more is needed. For this value of T it appears that an acceptable solution only exists in a narrow range of Mach numbers between about 1.13 and 1.19.

If the Sagdeev potential was the same downstream of the point where the potential reaches its maximum then we would just get a standard solitary wave solution, symmetric about this maximum. However, in the downstream region there is no reflected component and the second term in (1) is absent. This changes the Sagdeev potential and for suitable parameters produces structures with downstream oscillations.

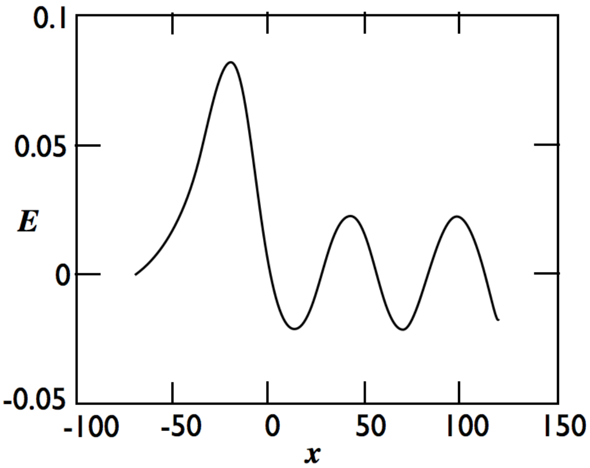

Figure 2: The normalized electric field corresponding to the potential of Figure 1

To explore the possible relevance to a laser fusion pellet compression we can do a calculation with a 50/50 mixture of deuterium and tritium upstream. With the potential and flow speed normalised in terms of the deuterium thermal velocity the ion density is half the expression in (1) plus a corresponding tritium contribution in which ϕ is replaced with $2\phi/3$ to take account of the higher mass. For $T = 20$ and $V = 4.75$, corresponding to a Mach number of 1.06, we get the solution shown in Figure 1. The corresponding electric field, normalized to $m_i V_i \omega_{pi}/(Ze)$, is shown in Figure 2.

Now let us relate these normalized values to physical parameters. If we assume that $Z = 1$, then we have for the electric field and length scale

$$\begin{aligned} E(V/m) &= 4.27 \times 10^{-3} E_{norm} T_i(keV)^{1/2} n_i(m^{-3})^{1/2} \\ L(m) &= 2.34 * 10^5 L_{norm} T_i(keV)^{1/2} n_i(m^{-3})^{-1/2}. \end{aligned} \tag{6}$$

If we look at the D-T result given above and assume an ion temperature of 500 eV and density 10^{28} m^{-3} then we get a peak electric field of 2.4×10^{10} V/m and, taking the normalized length of the main potential ramp to be 50, corresponding to a length of 83 nm. These parameters are in striking agreement with those quoted by Amendt et al [3].

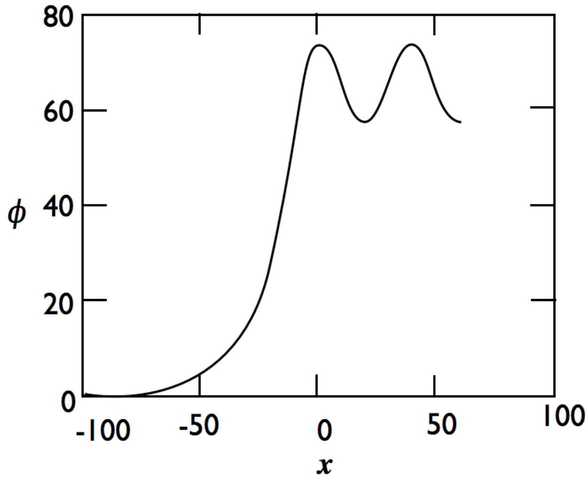

Figure 3: The potential for $T_e = 100$ and Mach number 1.35.

Now let us look at the results of Haberberger et al [5] mentioned above, where they attribute ion beams well collimated in energy to a shock wave in an expanding plasma. The electron temperature they find is about an MeV and we will assume that the already heated and expanding ions are at 10 keV, so that $T = 100$. The potential in this case, with a Mach number of 1.35 is shown in Figure 3.

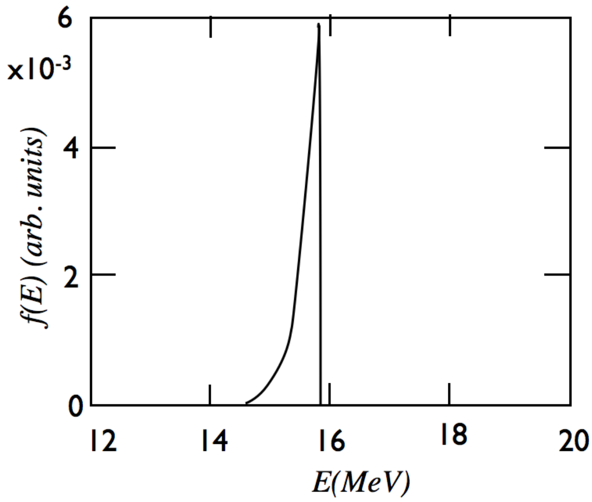

Figure 4: The energy spectrum of reflected ions for the parameters given in the text.

The normalized length scale is again about 50 which translates into a physical length of about 2 μm if we take $n = 10^{26}$ m^{-3} , while the peak electric field is around

1.3×10^{11} V/m, To compare with the experimental results, we look at the energy spectrum of the reflected ions. Adding the measured expansion velocity of $0.1c$ to the reflected ion velocity we get the spectrum shown in Figure 4.

This bears a striking resemblance to the experimental results, not only in the width of the spectrum and its energy but even in the detailed shape with a sharp edge on the high side. The density of reflected ions is about 8% of the background ion density, though this can go up down to less than 1% if the Mach number is reduced. The result given here appears to match the experiment much better than the computer simulation shown in the Haberberger et al [5] paper. One possible explanation is that the shock in the simulation has been launched with larger Mach number of about 2. This is well above the limit beyond which our laminar solutions do not exist (around 1.4), so it may be that what is being seen is some kind of turbulent shock, producing a much broader spectrum of fast ions.

In conclusion, we have given a simple analytic description of laminar shock structures in unmagnetized plasmas and shown that the theory, despite its simplicity, can provide an explanation of results from important recent experiments on high power laser plasma interactions.

This work was supported by the UK Engineering and Physical Science Research Council. RB thanks STFC Centre for Fundamental Physics for support.

References

[1] C.K. Li *et al.*, Phys. Rev. Lett **100**, 225001, (2008).

[2] J.R. Rygg *et al.*, Science **319**, 1223 (2008).

[3] P.A. Amendt *et al.*, Plasma Phys. and Control. Fusion **51**, 124048 (2009).

[4] P.A. Amendt *et al.*, Phys. Plasmas **18**, 056308 (2011).

[5] D. Haberberger *et al.*, Nature Physics **8**, 2130 (2012).

[6] R. Sagdeev, in *Reviews of Plasma Physics* **4**, ed. M.A. Leontovich (Consultants Bureau, New York, 1966).

[7] R.J. Taylor *et al.*, Phys. Rev. Lett. **24**, 206(1970).

[8] D.W. Forslund and J.P. Freidberg, Phys. Rev. Lett. **27** 1189 (1971).

[9] F. Fiúza *et al.*, Phys. Rev. Lett. **109**, 215001 (2012).

[10] I.R. Smirnovskii, J. App.Mech. and Tech. Phys. **39**, 335 (1998).

[11] I.R. Smirnovskii, Plasma Phys. Rep. **26**, 2446 (2000).

Creating hollow atoms with a petawatt laser

Contact *rjd517@york.ac.uk*

R. J. Dance, E. Wagenaars, O. Culfa, A. K. Rossall and N. C. Woolsey

York Plasma Institute
Department of Physics, University of York, York, YO10 5DQ

J. Colgan, J. Abdallah, Jr.

Theoretical Division, Los Alamos National Laboratory
Los Alamos, New Mexico, 87545, USA

S. A. Pikuz, A. Ya. Faenov,

I.Yu. Skobelev

Joint Institute for High Temperatures
Russian Academy of Sciences, Moscow 125412, Russia

N. Booth, K. L. Lancaster

Central Laser Facility
STFC Rutherford Appleton Laboratory, Didcot, Oxfordshire, OX11 0QX

R. J. Gray, P. McKenna

SUPA, Department of Physics
University of Strathclyde, Glasgow G40NG

T. Kaempfer, K. S. Schulze, I. Uschmann

Helmholtzinstitut Jena
Frobelsteig 1, D-07743, Jena Germany

A. G. Zhidkov

PPC Osaka University and JST CREST, 2-1, Yamadaoka, Suita, Osaka 565-0871, Japan

A. Ya Faenov

Quantum Beam Science Directorate
Japan Atomic Energy Agency, Kizugawa, Kyoto 619-0215, Japan

I. Uschmann

Institut fur Optik und Quantenelektronic, Friedrich-Schiller-Universitat Jena
Max-Wien Platz 1, D-07743 Jena, Germany

In recent publications we have presented measurements of unusual atomic spectra as a petawatt laser strikes an aluminium target [1,2]. The spectra are unusual as emission from ions with double K-shell vacancies dominate; this is qualitatively different to resonance line spectra typical of more standard laser-plasma experiments. The results imply that the laser interaction creates a large population of ions with completely empty innermost (principal quantum number, n = 1) atomic shells or K-shell with a double vacancy. Related observations have been made using the X-ray free electron laser LCLS at the Stanford Linear Accelerator by Vinko *et al*, [3].

The widely known K-α transition results from a single K-shell vacancy. In the field of intense laser-solid interactions, K-α emission is used extensively for the study of hot electron transport properties [4-6]. A K-shell vacancy can decay either via the radiationless Auger process, whereby a bound electron decays into the inner shell vacancy resulting in the ejection of a second electron, or via the radiative process where the bound electron decays into the vacancy resulting in emission of a photon. K-α emission results from radiative recombination of an L-shell (n = 2) electron into a single K-shell vacancy with the remainder of the atom intact. For cold Aluminium this transition has a wavelength of 8.36 Å [7]. The fluorescence yield for Al, the ratio of atoms decaying by radiative processes and those that do so by non-radiative Auger processes, is ~4% [8].

In intense laser-solid interactions, the main mechanism for production of K-α radiation is the collision of an energetic electron with an inner K-shell bound electron [9-11]. The observation of a KK-α implies a radiative transition as an L-shell electron moves to a K-shell with double vacancy. Creation of a double vacancy is only possible for sufficiently intense flux of exciting quanta. The single K-shell vacancy state has a lifetime of about 2 fs. To form a hollow atom it is necessary to remove a second bound inner electron within this lifetime.

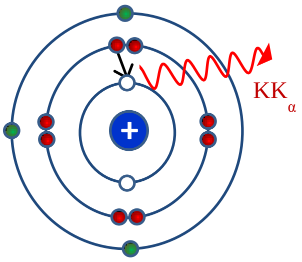

Figure 1 – Schematic of the aluminium KK hollow atom – double K-shell (n=1) vacancy and its radiative decay with the remainder of the L-shell wholly or partially intact.

Hollow atoms can be defined as atoms or ions which are ionised from the inside out [1], with multiple inner K- or L- shell electrons being ejected preferentially over the outer or valence electrons. Removal of only single or multiple K- or L- shell electrons renders atoms 'hollow' as described in Figure 1. We consider here the KK hollow atom state which is defined as a double K-shell vacancy, whilst the remainder of the electron shells are completely or partially intact.

The wavelength of the emission arising from the decay of a hollow atom is dependent on the degree of ionisation. As the level of ionisation increases, the transition wavelength shifts towards shorter wavelengths until a single bound electron remains. This corresponds to the hydrogenic ion. For example, the KK-α emission can result in a series of 11 peaks. For aluminium (Z = 13), with the longest wavelength (at approximately 7.7 Å) results from an ion with a complete L-shell to the shortest wavelength (at approximately 7.2 Å) for the hydrogenic ion. This transition is the familiar Lyman-α (Ly-α). The sequence, calculated use the Cowan atomic structure code [12] is given in Table 1, and displayed graphically in Figure 2.

Notation	Z*	Electrons remaining	Wavelength (Å)
L8M3	1	11	7.688
L8M2	2	10	7.685
L8M1	3	9	7.680
L8	4	8	7.675
L7	5	7	7.618
L6	6	6	7.555
L5	7	5	7.486
L4	8	4	7.413
L3	9	3	7.335
L2	10	2	7.624
L1 (Ly-α)	11	1	7.190

Table 1 – Notation used to distinguish the KK hollow atom configurations. Shown is average atomic number Z, number of electrons remaining in the atom, and wavelength of KK-α emission in that ion stage calculated by Cowan code [12].*

The notation is defined in Table 1, where L8M1 implies a filled L-shell (8 electrons) and a single electron in the n = 3 (M-shell). Vertical blue line in Figure 2 show the predicted KK-α wavelengths arising from the different ionisation stages of aluminium.

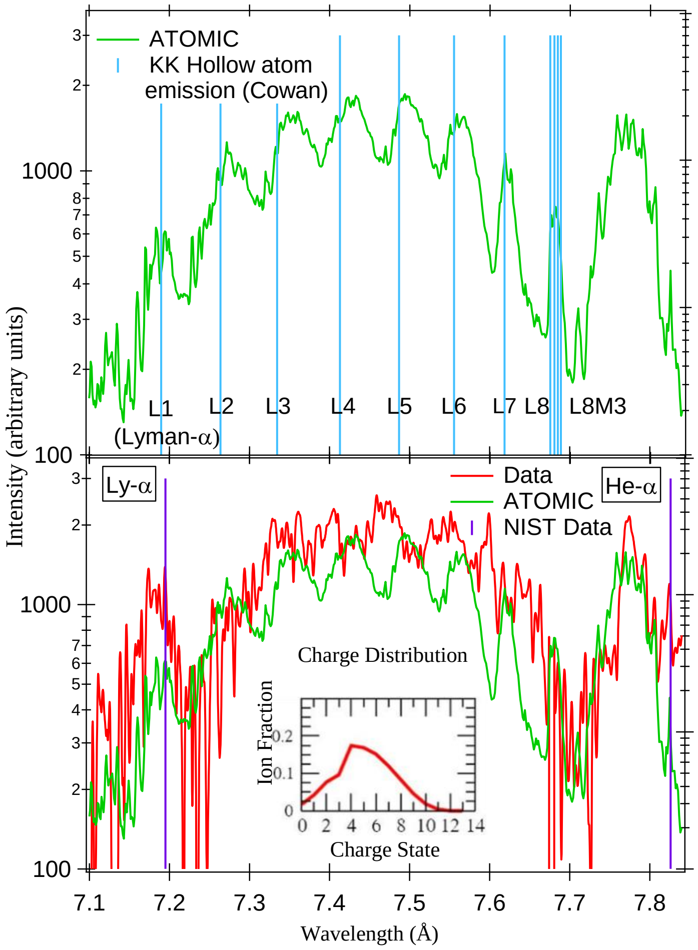

Figure 2 – (a) Top panel: ATOMIC code simulation of Aluminium K-shell emission, compared to expected wavelengths of hollow atom emission by the Cowan model (b) Bottom panel: Experimental data compared with the same ATOMIC simulation as in 2(a), with accepted NIST wavelengths for the Al He-α and Ly-α transitions[7].

Starting with only the outermost electron ($3p^1$) being ionised, the Al KK-α ($1s^0 2p^6$– $1s^1 2p^5$) hollow atom emission is shifted to shorter wavelengths as the atom is sequentially ionised, approaching the Ly-α spectral line at 7.19 Å. The wavelength of the KK emission decreases from around 7.7 Å by approximately 50-100 mÅ for each electron beyond the L8 electron, culminating with the Ly-α line at 7.19 Å as electrons are ionised. As the first four electrons are removed the shifts are small and cannot be resolved, meaning an observation of only 8 peaks would be expected from spectroscopic data.

Intense beams of energetic electrons (either as fast forward beam or the neutralizing, return current [13]) are characteristic of ultra-intense laser-solid interactions. These electron beams may be sufficiently intense to result in multiple inner-shell ionization.

Atomic physics modeling shows that inner shell ionization, see Figure 3, by x-ray photons rather than hot electrons is more probable. This indicates that for energies of 1 keV and above, KK hollow atoms are more efficiently created by x-ray photons. The integrated collision-radiative atomic calculations using the plasma atomic kinetics model ATOMIC [12] show that KK-α measurements reported by Colgan *et al.* [1] and Pikuz *et al.* [2] arise from intense x-ray radiation fields. In the same work, the authors show that intense electron beams result in KL hollow atoms [1,2].

At radiation and electron temperatures exceeding 1 keV, Figure 3 shows that radiation pumped KK hollow atoms are significantly more likely. Equally, for an electron beams more likely result in L-shell ionisation. For electrons, the ratio of

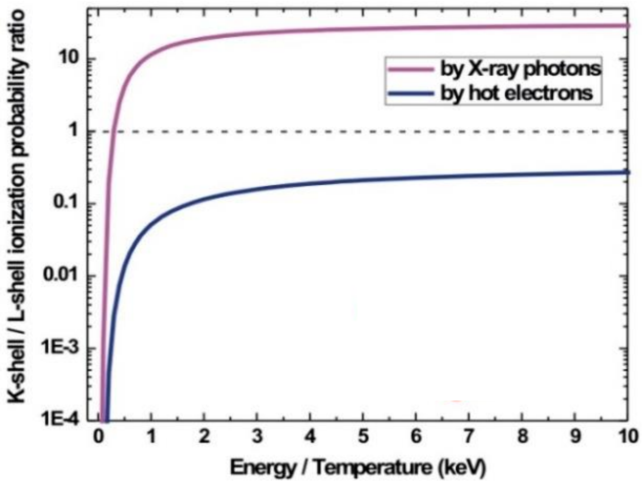

Figure 3 – Ionisation probability ratio from the K and L shells by photo-ionisation, or by electron collisional ionisation (blue). At energies >1keV, the probability of photo-ionisation is much greater than that of ionisation by hot electrons.

K/L shell ionisation remains below unity.

For ATOMIC simulations where neither contribution from hot electrons or from an external radiation field are included, the calculations show hollow atoms are not created. The inclusion of a 3 keV Planckian radiation field results in KK hollow atom production resulting in the prediction of strong emission in the 7.2-7.8 Å range. On inclusion of hot electrons, the most prominent effect is the production of KL hollow atoms. The spectral calculation, which combines the effects of the radiation field and hot electrons, is shown in Figure 2. The ATOMIC spectral calculation is compared to the Cowan calculation of KK-α spectral lines centres and experimental measurement in Figure 2(a) and 2(b) respectively. Both calculated and measured spectra show distinguishable KK-α emission peaks from individual Al hollow atom charge states. The grouping of the first four (unresolved) electron configurations is also inferred in the ATOMIC simulation, and measured spectra.

The K-shell ionisation potential for neutral Al is ~2 keV and as a result, one could be expect that the Al atom be fully ionised, and no spectral emission should be seen. However, due to the high (solid) density of this experiment, the rate of recombination (scaling as density squared) is high and atoms recombine very quickly, on femtosecond timescales. This measurement is most suitable for high density and contrast experiments.

The existence of an intense keV broadband radiation field is significant, and creation of KK hollow atoms indicates that its intensity must exceed 10^{18} Wcm^{-2}. This radiation originates from relativistic electrons interacting with the target-surface sheath fields (which we refer to as sheath field bremsstrahlung) and non-linear Thomson scattering in the laser field. The relativistic electrons form as a high-contrast petawatt laser strikes the aluminium target; electrons create large sheath fields at the front and rear surfaces of the target.

Electrons are reflected, or reflux, between these sheath fields, losing energy by bremsstrahlung and Thomson scattering with each pass of the target. This provides a plausible source for an intense radiation field. Only those photons or electrons that possess energy equal to or greater than the binding energy of a bound electron can cause its ionisation. The energy of individual laser photons in this experiment is approximately 1 eV, ruling out direct photoionisation [2].

Conclusions

We have described hollow atoms and shown that these result in multiple features between the typical spectral lines Ly-α and

He-α. These features are identified as emission of KK-α, resulting from the radiative transition between the $n = 2$ level to an empty $n = 1$ level with different degrees of ionization. Atomic kinetics calculations suggest that intense KK-α emission can occur in solid density aluminium when driven by keV Planckian radiation fields. In these extreme conditions, the high recombination rates at solid density continually repopulate bound atomic states. Strong KK-α emission has been observed in Vulcan petawatt experiments [1, 2]. This observation implies the existence of a keV radiation field with intensities exceeding 10^{18} Wcm^{-2}, approaching the Planckian limit [2]. Our analysis suggests the radiation field is driven by bremsstrahlung and Thomson scattering as relativistic electrons reflux in thin targets.

Acknowledgements

This work was supported by the UK Engineering and Physical Sciences Research Council, and the author would like to thank the staff and scientists of the CLF for their contribution and continued support of this work.

References

1. J. Colgan et al., Phys. Rev. Lett. 110, 125001 (2013)
2. S. A. Pikuz, High Energy Density Physics 9, 560-567 (2013)
3. S. Vinko et al., Nature Volume 482 (2012)
4. K. L. Lancaster et al. Phys. Rev. Lett. 98, 125002 (2007)
5. J. S. Green et al., Phys. Rev. Lett. 100, 015003 (2008)
6. R. B. Stephens et al., Phys. Rev. E 69, 066414 (2004)
7. National Institute of Standards and Technology Spectral Lines Database (http://www.nist.gov/pml/data/asd.cfm)
8. Centre for X-Ray Optics - X-ray Data Booklet, pp1-28
9. J. R. Davis Phys. Rev. E 69, 065402 (2002)
10. G. Christoforetti et al. Phys. Rev. E 87, 023103 (2013)
11. V. M. Ovchinnikov et al. Phys. Plasmas 18, 072704 (2011)
12. R.D. Cowan, Theory of Atomic Spectra, University of California Press, Berkeley (1981)
13. The Physics of Inertial Fusion, S. Atzeni and J. Meyer-Ter-Vehn, Clarendon Press Oxford (2004)

Advanced Models for the Effective Ionisation Energy in Dense Plasmas

Contact: R.A.Baggott@warwick.ac.uk

R.A. Baggott
Centre for Fusion, Space and Astrophysics, Department of Physics, University of Warwick, Coventry CV4 7AL, UK

D.O. Gericke
Centre for Fusion, Space and Astrophysics, Department of Physics, University of Warwick, Coventry CV4 7AL, UK

1 Introduction

In a dense plasma, the potential of the charge carriers will be screened by the presence of other free ions and free electrons. Screening effectively limits the range of the interaction between the particles and, thus, removes the long-range divergencies of the Coulomb potential occurring in many basic calculations [1]. As a result, screening modifies the equation of state as well as many transport and relaxation properties of a plasma.

Screening of the field of an ion also modifies the bound state structure associated with this ion. The main effect is a weakening of the bound states. Some bound states will even cease to exist if screening is strong enough [1]. Those states remaining will have their ionisation energies altered, that is lowered [2, 3, 4]. This change in ionisation energy is often called continuum lowering or ionisation potential depression (IPD). The IPD should be correctly quantified if the ionisation state of a dense plasma, and thus its properties, is to be predicted in equilibrium as well as for situations driven far out of nonequilibrium [5].

2 Basic description of Screening

In order to describe the screening of a potential, we start with the Poisson equation for the screened potential Φ in terms of the unscreened potential V. Sources for the initial field are densities of free electrons and ions

$$\nabla^2\Phi(\mathbf{r}) = -\frac{e^2}{\epsilon_0}\left[n_e(\mathbf{r}) - \Sigma_i z_i n_i(\mathbf{r})\right] + \nabla^2 V(\mathbf{r})\,, \qquad (1)$$

where i indexes different ion species.

The electrons often need to be treated using Fermi-Dirac statistics. Thus, their density in response to the effective potential is given by

$$n_e(\mathbf{r}) = n_e(\infty)\frac{\mathcal{F}(\beta_e(-\Phi(\mathbf{r})-\mu))}{\mathcal{F}(-\beta_e\mu)}\,, \qquad (2)$$

where

$$\mathcal{F}(\eta) = \frac{2}{\sqrt{\pi}}\int_0^\infty \frac{t^{\frac{1}{2}}\,dt}{e^{t-\eta}+1} \qquad (3)$$

is the Fermi integral of type $\frac{1}{2}$. The chemical potential, μ, is determined by

$$\mathcal{F}(-\beta_e\mu) = \frac{n_e(\infty)h^3}{2(2\pi m_e kT)^{3/2}}\,. \qquad (4)$$

The ions can be treated using Boltzmann statistics, giving

$$n_i(\mathbf{r}) = n_i(\infty)\,\exp\left[z_i\beta_i\Phi(\mathbf{r})\right]. \qquad (5)$$

Due to their much larger mass, the typical speed of an ion is much less than the average electron speed. This means that, for some applications, the ions will be effectively immobile over the relevant timescale [6]. In these cases, the ion contribution to the screening can be neglected: $e^{z_i\beta_i\Phi} \to 1$ and $n_i(r) = n(\infty)$.

The potential surrounding an ion is assumed to be spherical symmetric and the Poisson equation becomes

$$\frac{1}{r}\frac{d^2}{dr^2}\Phi(r) = \frac{e}{\epsilon_0}\left\{n_e\frac{\mathcal{F}(\beta_e(-\Phi(r)-\mu))}{\mathcal{F}(-\beta_e\mu)} - \Sigma_i z_i n_i \exp\left[z_i\beta_i\Phi(r)\right]\right\} + \frac{1}{r}\frac{d^2}{dr^2}V(r)\,. \qquad (6)$$

This equation must be solved subject to the boundary conditions

$$\Phi(r) \to V(r) \quad \text{as} \quad r \to 0\,, \qquad (7)$$
$$\Phi(r) \to 0 \quad \text{as} \quad r \to \infty\,. \qquad (8)$$

An analytic solution for the screened potential can be obtained if the free particles can be assumed to response linearly to the original field of the central ion. Moreover, one usually assumes that the spatial extent of the bound electrons is small compared to the length scale on which screening affects the system properties, i.e., the mean inter-particle distance or the screening length. Within this approximation, the bound electrons and nucleus to be treated as a compound particle effectively creating a Coulomb potential

$$V(r) = -\frac{\bar{Z}e^2}{4\pi\epsilon_0\, r}\,, \qquad (9)$$

where $\bar{Z}$ is the net charge of the ion.

Using the linear response treatment for a Coulomb potential with the effective charge $\bar{Z}$, we recover two of the earliest models for the screening of ions: considering nondegenerate electrons (classical limit) in Eq. (6) yields the Debye model [2]. For highly degenerate electrons that can be treated in the $T = 0$ limit, the ion-sphere model follows [3]. One of the most widely used screening models, developed by Stewart and Pyatt [4], smoothly interpolates between these two limiting cases.

3 Theory for Effective Ionisation Energies

Under the assumption that the bound electrons exist only at small volume around the ion, it is relatively easy to calculate the changes in the ionisation energy or IPD from the screened potential analytically. Taking the Schrödinger equation for a bound electron seeing the effective potential Φ

$$-\frac{\hbar^2}{2m_e}\,\nabla^2\Psi(\mathbf{r})+\Phi(\mathbf{r})\Psi(\mathbf{r})=E\,\Psi(\mathbf{r})\,, \tag{10}$$

we can apply an expansion of the potential Φ around $r=0$ [6]

$$\Phi\approx V(r=0)+\Delta E\,. \tag{11}$$

In this approximation, we find a constant shift to the binding energy for unscreened interactions whilst the wave function of the bound state is almost unchanged. Indeed, the new binding energies are $E_i-\Delta E$ for all bound states i. The IPD is therefore constant for all states and is given by

$$\Delta E=\left[\,\Phi(r)-V(r)\,\right]_{r\to 0}\,.$$

However, it is nowadays possible to produce plasmas experimentally, that exhibit screening lengths only a few times the bound state radius. For example, aluminium plasmas at solid density and a temperature of around 100 eV were produced by absorption of x-rays delivered by a free electron laser (FEL) [7]. For such conditions, the ionisation degree is roughly $\bar{Z}=3$, the Debye length is around 3.3 Bohr radii and the ion-sphere screening length around 3.0 Bohr radii. Higher ionisation levels result in even smaller screening lengths. On the other hand, the L-shell electrons occupy a volume that extends over more than a Bohr radius. We therefore need to allow for the finite extent of the bound states if we are to correctly quantify the change in bound state energies due to the surrounding plasma. The finite size of the bound states requires two changes to the derivation presented above: i) it is not sufficient to use a Coulomb potential for a charge $\bar{Z}$ as the unscreened potential and ii) one needs to reconsider how IPD is derived from the screened potential and, must calculate the new binding energy for the screened potential from the Schröedinger equation numerically.

To calculate the unscreened potential classically, we must consider the charge distribution due to the bound states. Moreover, there are also quantum mechanical effects to consider as the total wavefunction of the bound and free electrons must be anti-symmetric overall. Spin and position of the bound and the free electrons form a complete set of quantum-mechanical coordinates that effectively excluded the free electrons from regions where the bound state density is high.

The physics above can be cast into atomic pseudo-potentials that were developed in solid state physics to model the interaction between the complex of nucleus and core electrons and the valence electrons. They are designed to replace the nucleus and core electrons by a central potential without changing the wavefunctions of the valence electron (as obtained by the fully quantum-mechanical calculation) beyond some cut-off radius r_c [8]. Pseudo-potentials for ions have also been used with some success in modelling contributions of screening electrons for Thomson scattering in warm dense matter [9]. Here, we will apply the pseudo-potential approach to calculate the effect of IPD.

4 Results and Discussion

The use of atomic pseudo-potentials of arbitrary form does not allow for an analytic solution for the screened potential created by the central ion. We thus apply a numerical scheme here. First, atomic pseudo-potentials were created using the Opium package [10] for electronic configurations relevant to the ionisation of an aluminium ion with a charge state of $Z=3$: one configuration with a hole in the K-shell and one with an L-shell hole. For comparison, a Coulomb potential for a net charge of $Z=4$ was used.

In a second step, the related screened potentials were calculated from Eq. (6) that was discretised and solved under the boundary conditions given by Eqs. (7) and (8). The electron temperature was taken to be $T_e=70\,\mathrm{eV}$. The ions were assumed to be immobile which is a suitable assumption for matter under very short pulses as from FELs. Thus, we treat the ions in the limit $\beta_i\to 0$ which gives a uniform ion density (no screening). The average electron density far from the test ion was taken to be $n_e=1.8\times 10^{23}\,\mathrm{cm}^{-3}$. This density related to a plasma with a mean charge state of $\bar{Z}=3$ at solid density. The ion density was set by electro-neutrality of the system.

Figure 1 shows the three unscreened potentials used and the induced potentials, i.e. the difference between the unscreened and screened potentials, created by the response of the free electrons in the plasma to the field of the test ion. We find that the screening of the pseudo-potentials over the extent of the bound states is stronger than the one of the Coulomb potential with a similar net charge (negligible bound state extension). In particular, the difference is greatest near the outer edge of the bound states, where the nucleus is no longer perfectly screened by the bound electrons, but the free electron density is not yet large enough to cause significant quantum-mechanical exclusion.

Since the bound electrons are not placed at $r=0$ in the pseudo-potential approach, it is not appropriate to evaluate the induced potential at $r=0$ in order to find ΔE. As a first approximation, we evaluate the induced potential at the expected radius of a given orbital to get an estimate of ΔE for that orbital. For an electron in a 1s state, this approach gives $\Delta E=42.2\,\mathrm{eV}$ and for a 2p electron $\Delta E=39.1\,\mathrm{eV}$. For comparison, the

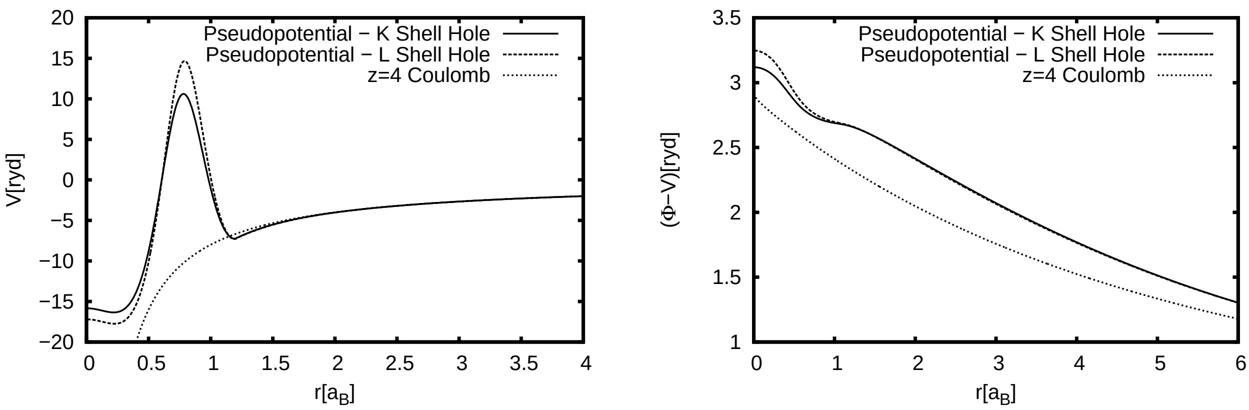

Figure 1: a) The three unscreened potentials used in the calculation. The point at which the pseudopotentials converge with the Coulomb potential gives an indication of the extent of the bound states. b) The induced potential, due to the free electrons and nearby ions which is calulated as $\Phi - V$. Note that there is significant variation of the induced potential over the extent of the bound states and beyond.

assumption of a Coulomb field with the same net charge of $Z = 4$ yields $\Delta E = 39.7\,\text{eV}$. We thus obtain larger IPD when considering the finite extent of the bound electrons than under the standard assumption of a pure Coulomb interaction with the free electrons.

5 Conclusion

The calculated screening of atomic pseudo-potentials in a hot, dense aluminium plasma is stronger than the one of the equivalent Coulomb potential. This effect could be attributable to the imperfect screening of the bare nuclear charge by the bound electrons when the finite extent of their wavefunction is considered.

For bound states with low quantum numbers n, our calculations of the change in the ionisation energy due to the surrounding plasma yields a higher value than that calculated by placing all the bound states at the origin. However, the induced potential varies appreciably over the extent of the bound state wavefunctions. Thus, the value of the induced potential at the peak of the wavefunction might not give the correct value for the IPD. More accurate values for the effective ionisation energies can be obtained by solving the Schrödinger equation for the screened potential obtained via the pseudo-potential approach presented here.

The pseudo-potential treatment does also introduce a dependence of the IPD on the orbital of the electron which would lead to a predicted change in the energy of emission lines relative to an isolated ion with the same electronic configuration. Such shifts of emission lines have now been observed experimentally in transitions well below the continuum edge [7, 11]. It is possible that a more rigorous calculation of the IPD from the screened potential via a solution of the Schödinger equation may partly reconcile this finding.

References

[1] D. Kremp, M. Schlanges and W.-D. Kraeft, *Quantum Statistics of Nonideal Plasmas* (Springer, Berlin 2005).

[2] P. Debye and E. Hückel, *Z. f. Phys.* **24**, 185 (1923).

[3] G. Zimmerman and R. More, *J. Quant. Spectrosc. Radiat. Transfer* **27**, 345 (1980).

[4] J.C. Stewart and K.D. Pyatt, Jr., *Astrophys. J.* **144**, 1203 (1965).

[5] M. Schlanges, Th. Bornath and D. Kremp, *Phys. Rev. A* **38**, 2174 (1988).

[6] M.S. Murillo and J.C. Weisheit, *Phys. Rep.* **302**, 1 (1998).

[7] S.M. Vinko *et. al.*, *Nature* **482**, 59 (2012).

[8] N.W. Ashcroft and N.D. Mermin, *Solid State Physics* (Brooks/Cole, London, 1976).

[9] D.O. Gericke, J. Vorberger, K. Wünsch and G. Gregori, *Phy. Rev. E* **81**, 065401 (2010).

[10] I. Grinberg, N.J. Ramer and A.M. Rappe, *Phys. Rev. B* **62**, 2311 (2000).

[11] O. Ciricosta *et. al.*, *Phys. Rev. Lett.* **109**, 065002 (2012).

Efficient laser pulse amplification by stimulated Brillouin scattering

Contact: raoul.trines@stfc.ac.uk

E. Guillaume, R. Trines, R. Heathcote, M. Galimberti, R. Bingham, P. Norreys
Central Laser Facility, STFC Rutherford Appleton Laboratory, Didcot, OX11 0QX, United Kingdom

K. Humphrey
University of Strathclyde, Glasgow, G1 1XQ, United Kingdom

H. Nakamura, G. Hicks, Z. Najmudin
Imperial College London, London, SW7 2BZ, United Kingdom

Y. Amano, H. Habara, K. Tanaka
Graduate School of Engineering, Osaka University, Osaka 565-0871, Japan

D. Doria, S. Kar, G. Sarri, M. Borghesi
Queens University Belfast, Belfast, BT7 1NN, United Kingdom

M. Skramic
University of Cambridge, Cambridge, CB2 1TQ, United Kingdom

E. Higson, J. Swain, K. Tang, J. Weston, P. Zak
University of Oxford, Oxford, OX1 3PU, United Kingdom

E.P. Alves, R.A. Fonseca, F. Fiúza, L.O. Silva
Instituto Superior Técnico, 1049-001, Lisbon, Portugal

Abstract

The energy transfer by stimulated Brillouin backscatter from a long pump pulse (15 ps) to a short seed pulse (1 ps) has been investigated in a proof-of-principle experiment. The two pulses were both amplified in different beamlines of a Nd:glass laser system, had a central wavelength of 1054 nm and a spectral bandwidth of 2 nm, and crossed each other in an underdense plasma in a counter-propagating geometry, off-set by 10°. It is shown that the amplification factor and the wavelength of the generated Brillouin peak depends on the plasma density, the intensity of the laser pulses and the competition between two-plasmon decay and stimulated Raman scatter instabilities, by comparison with particle-in-cell simulations. The highest obtained energy transfer from pump to probe pulse was 2.5%, at a plasma density of $0.17n_{cr}$, and this energy transfer increases significantly with plasma density. Therefore, our results suggest that much higher efficiencies can be obtained when higher densities (above $0.25n_{cr}$) are used.

1 Introduction

Exploring the intensity frontier is an exciting challenge for physicists. Advances in laser technologies, particularly those associated with increased power and decreased pulse duration, are of great interest due to their application to many fields in science and engineering. Present-day laser amplification and compression techniques are limited by the need to use (very) wide laser beams in order to prevent damage to the optical systems. Pulse compression methods using plasmas have been promoted as a way of overcoming the intensity limit of 10^{12} W cm^{-2} posed by solid-state optics. The enormous energy densities associated with focused high power lasers excite non-linear wave amplification in a medium that is already ionised. The plasma can support intensities of up to 10^{17} W cm^{-2}, i.e. 5 orders of magnitude larger than solid-state systems, before disruption to the medium occurs [1]. Laser pulse amplification in plasma rests upon an energy transfer between a relatively long duration pump pulse and a shorter seed pulse through the generation of either an electron plasma wave, known as Stimulated Raman Scattering (SRS), or through an ion - acoustic wave, known as Stimulated Brillouin Scattering (SBS). Experimental [2] and numerical [3, 4] results have already been demonstrated in the case corresponding to stimulated Raman scatter excitation.

As stimulated Brillouin scattering produces a frequency shift in the scattered wave spectra, it is necessary for the seed laser to be downshifted by an amount equal to the ion acoustic frequency in order for coupling between the laser beams to be realised. When utilising long duration beams, which naturally have a very narrow bandwidth, an adjustment to the seed laser is essential for coupling between the laser beams to ensure that the necessary frequency component for scattering is present in the seed. This creates an additional technical complexity to achieving Brillouin scattering in plasma. However, when the seed beam is sufficiently short, and its bandwidth is sufficiently wide, the necessary downshifted frequency to trigger Brillouin scattering of the pump pulse will already be available in the seed pulse, and no additional frequency modification will be needed.

In this paper, we report on experimental observations of Brillouin scattering using two beams incident from the same laser system, one long (15 ps) pump beam and one short (1 ps) seed beam counter-propagating with respect to one another through a volume of plasma, with no modifications made to the frequency of either pulse. These findings are corroborated by 1-D numerical simulations using the particle-in-cell code OSIRIS [5], confirming that for sufficiently short pulses the necessary Brillouin downshifted frequency is present in the laser bandwidth, therefore negating the requirement for a frequency downshift in the seed pulse to be performed before Brillouin scattering can be obtained. A pump-to-probe energy transfer of up to 2.5% has been obtained, which confirms earlier results by Lancia *et al.* [6], who obtained 2.25% in a similar experiment. We also found that the energy transfer efficiency increases consistently with density $0.017 < n_e/n_{cr} < 0.17$, while our simulation results show significant competition between stimulated Raman and stimulated Brillouin scattering at these densities. This both reduces the efficiency and indicates that much better results may be obtained for $n_e > 0.25n_{cr}$, where Raman scattering is no longer possible.

2 Theory

Stimulated Brillouin scattering in plasmas can be characterized as the scattering of a high frequency transverse electromagnetic wave by a low frequency ion-acoustic wave into a second transverse electromagnetic wave. This corresponds to the decay of an incident photon in the laser beam, with frequency ω_0 and wavenumber k_0 , into a phonon (ion-acoustic quantum) with frequency ω_{IAW} and wavenumber k_{IAW}, and a scattered photon, with frequency ω_s and wavenumber k_s which travels in approximately the opposite direction to the incoming laser photon. Following directly from linear theory [7] the frequency and wavenumber matching conditions, often invoked when studying the Brillouin instability, are:

$$\omega_0 = \omega_s + \omega_{\mathrm{IAW}} \tag{1}$$
$$k_0 = k_s + k_{\mathrm{IAW}} \tag{2}$$

where ω_{IAW} and k_{IAW} are the frequency and wavenumber of the ion acoustic wave, respectively, with $\omega_{\mathrm{IAW}} \ll \omega_0$. Since ω_{IAW} is so small, Brillouin scattering can operate at densities up to the critical density [8]. In addition to this, more energy can be transferred into the scattered wave via Brillouin scattering than for Raman scattering as less energy is coupled into the plasma wave. This makes the Brillouin mechanism particularly useful for applications such as laser amplification techniques [9, 6] and induced energy transfer between adjacent laser beams on facilities such as the National Ignition Facility [10, 11].

3 Experimental setup

The experiment was conducted on the Vulcan Nd:glass laser facility at the Rutherford Appleton Laboratory

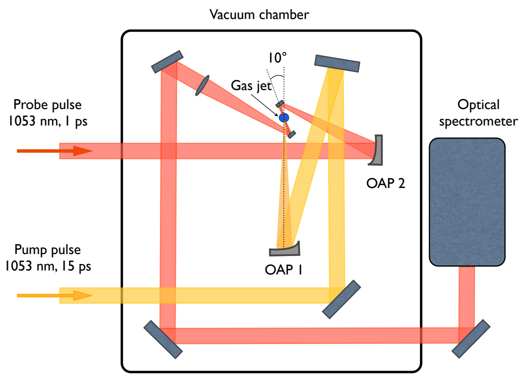

Figure 1: Schematic diagram of the experimental setup, described in the text.

[12]. This facility provided two linearly polarized laser pulses of $\lambda_0 = 1054$ nm central wavelength with a $\Delta\lambda_0 = 2$ nm bandwidth. The two laser beams diameters were reduced to 20 mm using pierced plastic plates, in order to have the correct spot size on target. Each laser pulse was focused onto target using $f/30$ off-axis parabolic mirrors, with $f = 612$ mm focal length, giving focal spots of 130 μm diameter. The pump beam contained between 570 and 860 mJ of energy, with a pulse duration $\tau_{pump} = 15$ ps, giving a pump intensity on target around 3×10^{14} W cm^{-2}. The seed beam contained between 38 and 477 mJ, with a pulse duration $\tau_{seed} = 1$ ps, giving a seed intensity on target between 2.5×10^{14} W cm^{-2} and 3.3×10^{15} W cm^{-2}. The laser pulses were injected in the target from opposite directions, with an angle of 10 degrees between the two counter propagating beams. This angle was used for safety reasons; while it leads to a small reduction in pulse growth, this was deemed acceptable. A 1.65 mm long overlap distance was achieved in this geometrical setup. The temporal delay between the pump and seed was adjusted so that the two ascending edges of the pulses crossed in the center of the gas target in order to maximize the interaction duration. This was achieved by using a streak camera looking at the overlap region. The laser pulses were focused in the center of a 5 mm long supersonic gas jet target, using either argon or deuterium. The gas target produced uniform plasmas when ionized, with background electron densities n_e varying between 1.7×10^{17} cm^{-3} and 1.7×10^{20} cm^{-3}. The plasma density was controlled by adjusting the backing pressure of the supersonic gas jet. The plasma is created by the interaction pulses themselves - without any ionization pulse needed - triggering multiphoton ionization of the gas and collisions between electrons and atoms. After the interaction, the seed pulse is collected and collimated after the interaction using silver mirrors and a 600 mm focal length lens, and steered into an optical spectrometer.

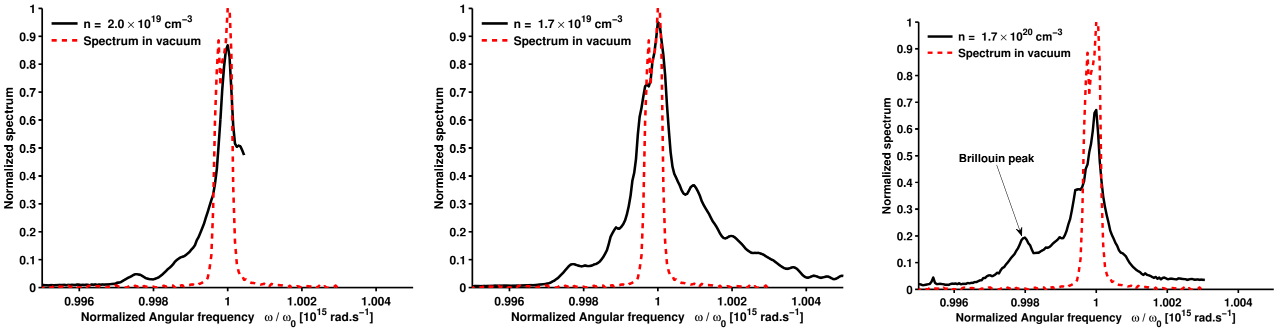

(a) (b) (c)

Figure 2: Experimental frequency spectra of a 1 ps laser pulse recorded after the propagation through a supersonic gas jet (normalized intensity versus normalized angular frequency). A reference spectrum, recorded with the gas jet turned off, has been included in each plot. Graph (a) is the spectrum recorded with only the seed beam at intensity 4.0×10^{14} W cm^{-2} interacting with the gas jet at $n_e = 2.0 \times 10^{19}$ cm^{-3}, without a counter propagating pump beam. Graph (b) was recorded with the two counter propagating beams interacting, the seed at intensity 3.6×10^{15} W cm^{-2} and the pump at 4.2×10^{14} W cm^{-2}, at $n_e = 1.7 \times 10^{19}$ cm^{-3}. Graph (c) was recorded with the seed at intensity 3.2×10^{14} W cm^{-2} and the pump at 3.2×10^{14} W cm^{-2}, at $n_e = 1.7 \times 10^{20}$ cm^{-3}. The generation of a down shifted peak can be observed through the interaction of the laser pulses and the gas jet, with its relative intensity compare to the fundamental peak strongly depending on the plasma density and the presence of a counter propagating pump pulse.

The light transmitted through the plasma in the direction of propagation of the seed beam was collected and collimated using a 600 mm focal length lens. The collimated beam was then steered out of the target chamber using flat silver mirrors, and focused onto the entrance slit of an optical spectrometer, equipped with a 150 lines/mm diffraction grating coupled with an Andor 16-bit CCD camera recording the spectra with a 0.1 nm resolution. A schematic diagram of the experiment can be seen in Fig. 1. Note that the transmitted seed was measured only for the case of seed and pump interacting with parallel horizontal polarizations.

4 Experimental results

The results of the experiment are shown in Fig. 2. The figure shows three optical spectra of the transmitted laser light taken at different plasma densities, with different laser configurations. Figure 2 (a) represents the transmitted spectrum passing through the gas jet, with the pump beam turned off. Figures 2 (b) and (c) show the transmitted spectra through the gas jet in the presence of the pump beam, for two different plasma densities (1.7×10^{19} cm^{-3} and 1.7×10^{20} cm^{-3}, respectively). The interaction with the gas jet and the pump beam clearly modifies the transmission spectrum of the seed. In the shot without a pump beam [Figure 2 (a)], the propagation of the seed pulse through the plasma causes the formation of a small secondary peak, at $\omega/\omega_0 = 0.9975$. Since the separation between those peaks is much smaller than the plasma frequency for this configuration, the peak cannot correspond to stimulated Raman scattering, and is presumed to correspond to spontaneous stimulated Brillouin scattering by the seed pulse. The addition of an energetic pump beam, while keeping the plasma density the same, significantly enhances this downshifted spectral peak, proving that we have obtained pump-to-seed energy transfer via stimulated Brillouin backscattering. By increasing the plasma density by an order of magnitude, one can observe a significant increase of the relative intensity and energy content of the peaks: the secondary peak is now only 3.5 times smaller than the fundamental. Note that for experimental shots with similar laser parameters, but with plasma densities between 1.7×10^{17} cm^{-3} and 1.8×10^{18} cm^{-3}, no secondary peaks could be observed.

The energy transfer efficiency is calculated as follows. For the laser shot depicted in Figure 2 (c), the pump energy was 675 mJ after passage through the 20 mm diameter aperture, while the seed pulse energy was 86 mJ. From the vacuum shot and the height of the Brillouin peak in Figure 2 (c), it can be deduced that the Brillouin peak contains about 20% of the original seed energy, or 17 mJ. This corresponds to a 2.5% energy transfer efficiency from pump to seed.

5 Simulations

The numerical simulations were conducted in 1-D using the fully relativistic particle-in-cell code OSIRIS [5] and were constructed to mirror the experimental parameters as closely as possible. For these simulations, the plasma electron temperature and the effective ionization degree of the atoms are needed. These quantities were caculated using the laser plasma simulation code MEDUSA, in 1-D planar geometry, using a corrected Thomas-Fermi

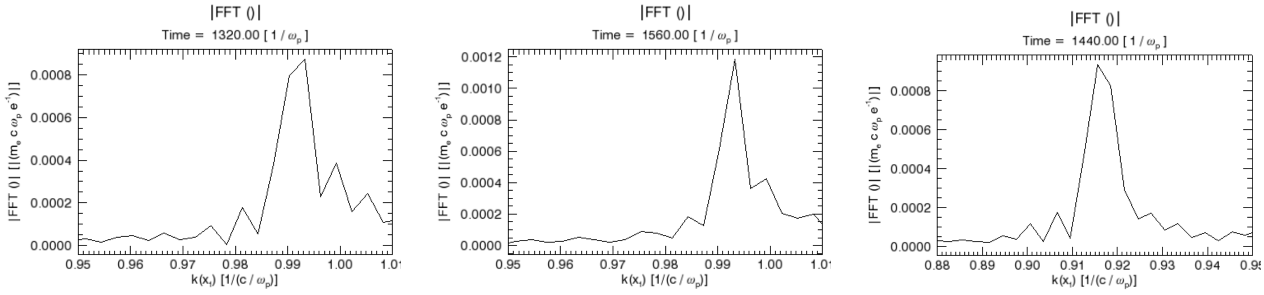

(a) (b) (c)

Figure 3: Simulated spectra corresponding to each of the experimental regimes examined in the previous part (normalized intensity versus normalized wave vector). Electron density varied from 1.7×10^{19} cm^{-3} to 1.7×10^{20} cm^{-3}. Graph (a) is the spectrum simulated with a single laser of intensity 6×10^{14} W cm^{-2} interacting into an neon-like argon plasma with an electron temperature of about 20 eV and density of 0.018 n_c. Spectrum (b) was calculated with the two counter propagating beams interacting in a deuterium plasma of density $0.015 \times n_c$, the seed at intensity 5.4×10^{15} W cm^{-2} and the pump at 6.2×10^{14} W cm^{-2}, with an electron temperature of 120 eV. Graph (c) was simulated with the seed at intensity 4.9×10^{14} W cm^{-2} and the pump at 4.9×10^{14} W cm^{-2}, in an argon plasma with an electron temperature of 5 eV and a density of 0.16 n_c.

equation-of-state model and an average atom model, and assuming collisional ionisation. For the shots shown in Figure 2, this yields $T_e = 130$ eV, 120 eV and ?? eV respectively and $Z^* = 5.5$, 1.0 and ??. These values were used to estimate the plasma electron density for each case, which was used in the OSIRIS simulations.

Three sets of simulation results corresponding to each of the three experimental regimes examined are presented, and were set up as follows. In simulation (a) a single laser of intensity 6×10^{14} W cm^{-2} was injected into an argon plasma of density 0.018 n_c with a mass ratio for ions to electrons of $m_i/m_e = 14688$. The plasma temperature ratio was set such that $ZT_e/T_i = 25$ where $Z = 5$ and $T_e = 20$ eV, assuming neon-like argon with the majority of the outer shell of electrons depleted. For simulation (b) two counter-propagating pulses were launched into a plasma of density $0.015 \times n_c$, in this case comprising of deuterium, with a mass ratio of ions to electrons where $m_i/m_e = 3672$ with the plasma ion and electron temperatures kept constant at 20 eV for the ions and 120 eV for the electron species. Laser intensities of 6.2×10^{14} W cm^{-2} and 5.4×10^{14} W cm^{-2} for the pump and seed, respectively, were used where the seed pulse was launched at the instant the pump laser had traversed the length of the plasma. In the case of simulation (c), two counter-propagating beams were used and their intensities were both set to 4.9×10^{14} W cm^{-2} and propagated through an argon plasma with a configuration such that $m_i/m_e = 73440$, $ZT_e/T_i = 5$ where $Z = 1$ and $T_e = 5$ ev and a density of 0.16 n_c. The following parameters are consistent throughout each of the three simulations presented : the pulses propagate through a plasma column of length $1410c/\omega_0$ with the pump pulse traveling from right to left through the simulation box, the pump pulse has a duration of 1.5 ps and the seed pulse a duration of 100 fs, each of the pulses are from a laser of wavelength 1 μm, the time step for integration is $\Delta t = 0.04\ \omega_p^{-1}$ where ω_p is the plasma electron frequency, and the spatial resolution of the simulations is of the order of the Debye length with 100 particles per cell. Due to computational limitations the pulse lengths and plasma column have been scaled down by a factor of ten from that of the parameters used to obtain the experimental results.

Upon examination of the spectra presented in Fig. 3 it can be seen that the results obtained by OSIRIS closely match the results obtained from the experimental observations of Brillouin scattering shown in Fig. 2. In each of the three cases examined numerically, however, it can be seen that the Fourier spectra obtained is slightly broader than that of the experimental results. This slight variation in the spectra is attributed to the fact that the simulations have no transverse dimensions as they were performed in 1D, hence putting numerical constraints on the solutions obtained as there can be no transverse variation of the laser intensity. Therefore the amplitude of any plasma wave driven by the laser will be overestimated which leads to an overestimation of spectral drifts and of the temperature recorded also.

6 Conclusions

These experimental observations of Brillouin scattering using two beams at the same wavelength are a promising confirmation of the observations by Lancia et al. [6] that Stimulated Brillouin amplification can be achieved with a single laser system, with no frequency downshift required in the seed pulse as is mandatory to perform Raman amplification. In addition, we have revealed that an increase in plasma density leads to an increase in energy transfer efficiency, because of the increased Brillouin growth rate and the disappearance of Raman scattering above $0.25n_{cr}$. The generation of a Brillouin peak using the natural bandwidth of the laser is confirmed by the 1-D PIC simulation results from OSIRIS. The same PIC simulations also revealed significant competition between Stimulated Raman and Stimulated Brillouin scattering, for densities between $0.017n_{cr}$ and $0.17n_{cr}$. The experiments revealed a substantial increase in the Stimulated Brillouing scattered signal with increasing plasma density, in line with the theoretically predicted increase of the growth rate. In light of these results, it is recommended that future Brillouin amplification experiments are carried out at plasma densities above $0.25n_{cr}$ to eliminate Stimulated Raman scattering altogether and benefit from the higher Brillouin scattering growth rate.

Acknowledgements

The authors would like to gratefully acknowledge the support of the staff of the Central Laser Facility for their help. They would also like to thank R. Kirkwood, S. Wilks, D. Meyerhofer, S. Craxton, J. Myatt and A. Solodov for useful discussions. This work was supported by the UK Science and Technology Facilities Council and by the Engineering and Physical Sciences Research Council. HN was supported by the Royal Society Newton International Fellowship and the Japan Society for the Promotion of Science.

References

[1] N. J. Fisch and V. M. Malkin, Phys. Plasmas **10**, 2056 (2003).
[2] J. Ren *et al.*, Phys. Plasmas **15**, 056702 (2008).
[3] R. M. G. M. Trines *et al.*, Nature Physics **7**, 87-92 (2011).
[4] R. M. G. M. Trines *et al.*, Phys. Rev. Lett. **107**, 105002 (2011).
[5] R. A. Fonseca *et al.*, Lect. Notes Comp. Sci. **2331**, 342-351 (2002).
[6] Lancia L. *et al.*, Phys. Rev. Lett. **104**, 025001 (2010).
[7] D. W. Forslund *et al.*, Phys. Fluids **18**, 1002 (1975).
[8] W. L. Kruer, *The Physics of Laser Plasma Interactions* (Westview Press, 2003).
[9] A. A. Andreev *et al.*, Phys. Plasmas **13**, 053110 (2006).
[10] P. Michel *et al.*, Phys. Plasmas **16**, 042702 (2009).
[11] P. Michel *et al.*, Phys. Plasmas **17**, 056305 (2010).
[12] C. N. Danson *et al.*, Nucl. Fusion **44**, S239 (2004).

Vacuum Birefringence Revisited

Contact: *theinzl@plymouth.ac.uk*

Thomas Heinzl
School of Computing and Mathematics
Plymouth University
Drake Circus, Plymouth PL4 8AA, UK

1 Introduction

The idea of probing light with light only makes sense in *quantum* electrodynamics where the appearance of virtual pairs results "in a polarisation of the vacuum and hence in an alteration of Maxwells equations" as stated by Heisenberg and Euler in 1936 [1]. The alterations make Maxwell's equations nonlinear and hence correspond to a self-interaction of the photons via fermion loops. At low energies the space-time structure of these loops is not resolved so that they are reduced to effective vertices. As the field equations become cubic the associated low-energy effective Lagrangian is quartic to lowest order in photon-photon interactions and represented by the Feynman diagram of Fig.1. This has first been discussed by Euler and Kockel [2] (see below), while the all-orders expression is the celebrated Heisenberg-Euler expression [1].

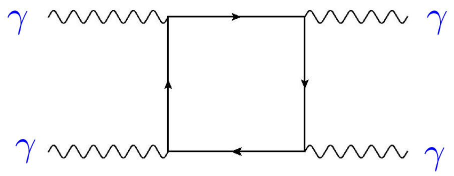

Fig.1: Light-by-light scattering to lowest order in QED.

One can say from the outset that the nonlinear effects (at low energies) must be small. Their size is basically encoded in the photon-photon scattering cross section which may be estimated using dimensional analysis together with Lorentz and gauge invariance. These principles dictate that the fourth order terms in the effective Lagrangian are of the form $(e\partial A/m)^4$ where e and m denote the electron charge and mass while A is the gauge potential. Hence the cross section for $\gamma\gamma \to \gamma\gamma$ (proportional to the amplitude of Fig.1 squared) goes like

$$\sigma \sim \left(\frac{e^4\omega^4}{m^4}\right)^2 \frac{1}{\omega^2} \sim \alpha^4\omega^6/m^8 \ , \quad \omega \ll m \ . \tag{1}$$

Here we have adopted natural units, $\hbar = c = 1$, and employed the fine structure constant $\alpha = e^2/4\pi$. ω denotes the photon frequency in the centre-of-mass (CM) frame. For optical photons (aka. visible light) we use $\omega = 1$ eV and estimate

$$\sigma \simeq 10^{-66} \text{ cm}^2 \ , \tag{2}$$

which is small even by particle physics standards. For higher energies the cross section can become as large as 10^{-30} cm^2 [3] but in this regime the available photon fluxes are too small. Hence, the scattering of real photons, though first predicted in 1934 [4], remains unobserved to this day. The current upper bound in the optical regime is $\sigma \le 1.5 \times 10^{-48}$ cm^2 [5].

Before we look at the effective Lagrangian in more detail let us discuss things from a (semi-)classical perspective. We imagine to use an X-ray beam to probe an optical laser focus, hence we consider the microscopic (quantum) process $\gamma_{\rm X} + \gamma_{\rm L} \to \gamma'_{\rm X} + \gamma'_{\rm L}$. (We will henceforth use subscripts X and L to denote X-ray and optical laser quantities, respectively.) The nonlinear interaction of Fig.1 then implies that probe photons will scatter off the photonic target. Using the language of optics we thus expect that the probe beam will experience typical phenomena such as reflection, deflection, refraction or diffraction. The task is then to extract these from the quantum picture encoded in Fig.1.

Let us assume that the background optical laser is described by a (possibly pulsed) plane wave with central wave vector $K = (\Omega, \mathbf{K})$ and electromagnetic fields $\mathbf{E}$ and $\mathbf{B}$, perpendicular to each other and of equal magnitude ($\mathbf{E}\cdot\mathbf{B} = 0$, $E = B$). This is probed by another wave (of X-ray frequency) with wave vector $k = (\omega, \mathbf{k})$ such that $\mathbf{k}\cdot\mathbf{K} = \omega\Omega\cos\theta$, see Fig.2.

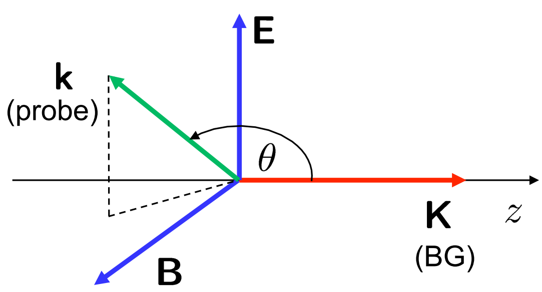

Fig.2: Kinematics of probing light with light.

We will often consider counter-propagating beams, i.e. a head-on (HO) collision where $\theta = \pi$. It is worth noting that in the CM frame probe and background have the same frequency,

$$\omega_{\rm CM} = \sqrt{\omega\Omega}\sin\theta/2 \ . \tag{3}$$

This becomes largest for HO collisions and results in $\omega_{\rm CM} \simeq 10^2$ eV for $\omega \simeq 1$ eV and $\Omega \simeq 10$ keV. So clearly, one stays safely in the low-energy regime, $\omega_{\rm CM} \ll m$.

Using the wave vectors and field strengths one can form two basic invariants, namely,

$$
\begin{aligned}
I_1 &\equiv k \cdot K \stackrel{\rm HO}{=} 2\Omega\omega \; , && (4)\\
I_2^2 &\equiv k_\mu T^{\mu\nu} k_\nu \stackrel{\rm HO}{=} 4\omega^2 E^2 \; . && (5)
\end{aligned}
$$

Field strengths are encoded in the second invariant I_2 built from the Maxwell energy momentum tensor, which for plane waves takes the form

$$
T^{\mu\nu} = F^{\mu\lambda} F_\lambda{}^\nu = (E^2/\Omega^2) K^\mu K^\nu . \qquad (6)
$$

I_2^2 may be regarded as the energy density 'seen' by the probe and hence must be positive, which is the content of a null energy theorem in general relativity [6]. Note that, for plane waves (or, more generally, null fields), the canonical field invariants vanish

$$
\begin{aligned}
\mathscr{S} &= -\frac{1}{4} F_{\mu\nu} F^{\mu\nu} = \frac{1}{2}(E^2 - B^2) = 0 \; , && (7)\\
\mathscr{P} &= -\frac{1}{4} F_{\mu\nu} \tilde{F}^{\mu\nu} = \mathbf{E} \cdot \mathbf{B} = 0 \; , && (8)
\end{aligned}
$$

with $\tilde{F}^{\mu\nu} = \epsilon^{\mu\nu\rho\sigma} F_{\rho\sigma}$ denoting the dual field strength. These 'null properties' represent another (formal) reason why plane waves are somewhat elusive, i.e. difficult to probe.

Let us make the invariants dimensionless by introducing the Sauter-Schwinger electric field [7, 8] ,

$$
E_S \equiv \frac{m^2}{e} \simeq 1.3 \times 10^{18} \text{ V/m} \; , \qquad (9)
$$

which is the typical magnitude of electric fields in QED. In such a field an electron gains an energy m across a Compton wavelength, $1/m$, and hence the probability of vacuum pair production becomes sizeable[1]. In QED it thus makes sense to measure electric fields in units of (9) which leads to the dimensionless field strength parameter,

$$
\epsilon \equiv E/E_S \; . \qquad (10)
$$

Similarly we measure laser and probe frequencies in terms of the electron rest mass, m,

$$
\nu_{\rm L} \equiv \Omega/m \; , \quad \nu_{\rm X} \equiv \omega/m \; . \qquad (11)
$$

In terms of the invariants (4) and (5) we thus find the useful relations [9]

$$
\begin{aligned}
I_1/m^2 &\stackrel{\rm HO}{=} 2\,\nu_{\rm X}\nu_{\rm L} \; , && (12)\\
\kappa \equiv e I_2/m^3 &\stackrel{\rm HO}{=} 2\,\epsilon\nu_{\rm X} \; , && (13)\\
a_0 \equiv e I_2/m I_1 &\stackrel{\rm HO}{=} \epsilon/\nu_{\rm L} \; . && (14)
\end{aligned}
$$

In the last identity (14) we have introduced the dimensionless laser amplitude

$$
a_0 := \frac{eE\lambda_L}{mc^2} = \frac{eE}{m\Omega} \qquad (15)
$$

in an invariant way [10]. It measures the energy gain (in units of mc^2) of an electron traversing a laser wave length, λ_L. Note, however, that the definition (14) is purely in terms of the 'photonic' invariants I_1 and I_2. The electron features solely in terms of the elementary charge, e, which connects back to (9).

2 Vacuum birefringence

Vacuum birefringence results from a change in polarisation when a probe photon with polarisation λ passes through a localised intense field region so that $\lambda \to \lambda'$. The relevant diagram (to lowest order) is a variant of light-by-light scattering (Fig.1) where two of the photons now correspond to an external field, denoted by the dotted lines in Fig.3.

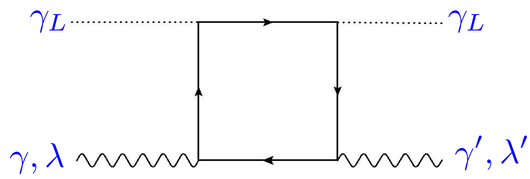

Fig.3: Vacuum birefringence from light-by-light scattering. γ_L denotes the BG laser photons.

Formally, this may be described in terms of the forwards scattering amplitude, $S_{\lambda\lambda'}$, for the process ($\gamma \to \gamma'$, $k \to k$, $\lambda \to \lambda'$). Equivalently, one may employ the vacuum polarisation tensor,

$$
\Pi^{\mu\nu} \equiv \epsilon_\lambda^\mu S_{\lambda\lambda'} \epsilon_{\lambda'}^\nu \; . \qquad (16)
$$

with ϵ_λ^μ and $\epsilon_{\lambda'}^\nu$ denoting the incoming and outgoing photon polarisation vectors, respectively. The associated probe photons correspond to a fluctuating field a while the polarisation tensor depends on the background photons through an external field A, $\Pi^{\mu\nu} = \Pi^{\mu\nu}[A]$. For general backgrounds, the polarisation tensor is difficult to calculate and normally not known in any detail. For slowly varying fields, however, i.e. at low energy, it may easily be read off from the Heisenberg-Euler effective Lagrangian [1] which, to leading order in the field strength expansion, reads

$$
\mathcal{L}_{\rm HE,LO} = \frac{1}{2}\,\rho\left(c_- \mathscr{S}^2 + c_+ \mathscr{P}^2\right) \; . \qquad (17)
$$

It depends only on the field invariants (7) and (8), with parameters $c_- = 4$, $c_+ = 7$ and

$$
\rho := \frac{4}{45}\frac{\alpha^2}{m^4} = \frac{\alpha}{45\pi}\frac{1}{E_S^2} \; . \qquad (18)
$$

Dimensional analysis requires that ρ has units of an inverse electric field squared as is indeed borne out by

[1] One of the challenges of strong-field physics is to create such a field across a *macroscopic* distance (say a laser focus) and not just over a Compton wavelength. For null fields, though, the pair creation amplitude vanishes with the invariants (7) and (8) [8].

the last identity. As stated above, the Heisenberg-Euler representation (17) is valid for energies small compared to the electron mass, m. Note that the Lagrangian (17) would vanish for null fields, but not for a linear combination thereof. We will exploit this latter property momentarily.

To proceed we assume that both fluctuating and background fields have energies below m (certainly a good approximation for optical and X-ray photons). This justifies to continue using (17) and split all fields there into background and fluctuation, $F \to F + f$, whence $A \to A + a$. The term quadratic in fluctuations is then $\mathcal{L}_2 = (1/2) a_\mu \Pi_2^{\mu\nu}[A] a_\nu$ with

$$\begin{aligned} \Pi_2^{\mu\nu} &= (1 + 4\rho\mathscr{S})(\Box g^{\mu\nu} - \partial^\mu \partial^\nu) \\ &- \rho\,(c_- F^{\mu\alpha} F^{\nu\beta} + c_+ \tilde{F}^{\mu\alpha} \tilde{F}^{\nu\beta}) \partial_\alpha \partial_\beta \ , \end{aligned} \quad (19)$$

where the invariant $\mathscr{S}$ now refers to background only. The second line defines the vacuum polarisation tensor. After Fourier transforming, it takes on the simple form [6]

$$\Pi^{\mu\nu}(A; k) = \rho\,(c_- F^{\mu\alpha} F^{\nu\beta} + c_+ \tilde{F}^{\mu\alpha} \tilde{F}^{\nu\beta}) k_\alpha k_\beta \ . \quad (20)$$

Note that this is homogeneous in k, $\Pi^{\mu\nu}(A; k) = C^{\mu\nu\alpha\beta}(A) k_\alpha k_\beta$. The polarisation tensor has two nontrivial eigenvalues given by the Lorentz traces of the two separate terms in (20),

$$\Pi_\pm \equiv c_\pm \rho\, I_2^2 \ , \quad (21)$$

with the invariant I_2^2 from (5), expressed in terns of the BG energy momentum tensor. These in turn imply two dispersion relations,

$$k^2 = -c_\pm \rho\, I_2^2 \le 0 \ . \quad (22)$$

We introduce the refractive index n by parameterising the probe wave vector as $k = \omega(1, n\hat{\boldsymbol{k}})$, whence $n = 1 - k^2/2\omega^2$ such that (22) implies two indices,

$$n_\pm = 1 + c_\pm \rho\, I_2^2 / 2\omega^2 \ . \quad (23)$$

For the kinematics of Fig.2 this may be evaluated as

$$n_\pm = 1 + \tfrac{1}{2}\, c_\pm \rho\, E^2 (1 - \cos\theta)^2 \overset{\text{HO}}{=} 1 + 2 c_\pm \rho\, E^2 \ , \quad (24)$$

where the last identity maximising the correction holds for head-on collisions.

In terms of the field strength parameter ϵ from (10) the refractive indices (24) may be expressed compactly as

$$n_\pm = 1 + \frac{11 \pm 3}{45\pi} \alpha \epsilon^2 \ . \quad (25)$$

The experimental signature already pointed out by Toll [11] is given by an ellipticity signal $\delta^2 = (\Delta\phi/2)^2$ stemming from the phase retardation $\Delta\phi = \omega d \Delta n$ between ordinary and extraordinary beams upon traversing a distance d inside the optical focus. Explicitly, one has from (25)

$$\Delta\phi = \frac{4\alpha}{15} \frac{d}{\lambda_{\text{X}}} \epsilon^2 \ . \quad (26)$$

If we take a focus length of $d = 10\ \mu$m, $\lambda_{\text{X}} = 0.1$ nm and $\epsilon^2 = 5 \times 10^{-8}$ (which corresponds to an intensity of about 10^{22} W/cm^2) we find an ellipticity signal

$$\delta^2 \simeq 3 \times 10^{-11} \ . \quad (27)$$

3 Gaussian beams

In the previous section both fluctuation and background, i.e. probe X-ray and optical laser beams, were assumed to be plane waves. Even if pulsed, hence of finite extent in their respective phase arguments ($k \cdot x \equiv \omega x^-$ and $K \cdot x \equiv \Omega x^+$), plane waves still suffer from (at least) two shortcomings: (i) they have infinite transverse extent, thus carry infinite energy, and (ii) they live forever, that is, at any given time there is a right-moving and a left-moving pulse to be found down their worldlines. Both flaws are remedied by using Gaussian beams – at the price of losing analytical power. The only way to proceed analytically nevertheless is to make the adiabaticity assumption that one can use the slowly-varying field results and treat the space-time dependence in a parametric way. This philosophy has been successfully adopted before [12, 13, 14].

Our use of Gaussian beams is based on the lucid discussions of [15] and, in particular, [16]. A Gaussian beam is characterised by both a longitudinal and a transverse length scale, z_0 and w_0, respectively. z_0 denotes the Rayleigh length and w_0 the waist radius. The two length parameters are not independent but related via

$$z_0 = \frac{w_0^2}{2\lambda} = \frac{k w_0^2}{2} \ . \quad (28)$$

For strong focussing, say to the diffraction limit, $w_0 = \lambda$, one has a minimum Rayleigh length of $z_0 = \pi\lambda$. Gaussian beams are obtained as solutions of the wave equation in the paraxial approximation, i.e. by systematically expanding in the ratio

$$\sigma \equiv \frac{w_0}{z_0} = \frac{2\lambda}{w_0} = \frac{2}{k w_0} \ , \quad (29)$$

variably referred to as the numerical aperture, inverse f-number [17] or beam divergence angle [18]. For a strongly focussed optical laser ($\lambda_{\text{L}} = 0.8\ \mu$m, $w_{0,\text{L}} = 1\ \mu$m) one finds a value of $\sigma = \lambda_{\text{L}}/\pi w_{0,\text{L}} = 0.25$. This suggests that there are substantial (order 25%) corrections to the paraxial approximation, as is to be expected for strong focussing.

Following [15, 16] we introduce the dimensionless coordinates

$$\rho \equiv \sqrt{x^2 + y^2}/w_0 \ , \quad \zeta \equiv z/z_0 \ . \quad (30)$$

To leading order in σ (the paraxial approximation proper) the electric and magnetic fields, $\mathbf{E} = E_x \hat{\mathbf{x}}$, $\mathbf{B} = B_y \hat{\mathbf{y}}$, of the optical laser are given by

$$E_x = B_y \equiv \mathrm{e}^{-i\Omega x^+} \psi_0 + c.c \ , \quad (31)$$

with the 'shape functions'

$$\psi_0(\rho,\zeta) \equiv \hat{E}\, f(\zeta)\, \mathrm{e}^{-\rho^2 f(\zeta)} , \quad (32)$$

$$f(\zeta) \equiv \frac{1}{1+i\zeta} = \frac{1}{1+\zeta^2} - i\frac{\zeta}{1+\zeta^2} , \quad (33)$$

where $\hat{E}$ denotes the field amplitude. One may check that $\mathbf{E}$ and $\mathbf{B}$ are divergence free up to terms of order σ. Hence, the electromagnetic field given by (31), to leading order in σ, is still null, i.e. $\mathscr{S} = \mathscr{P} = O(\sigma)$.

The intensity is the modulus of the Poynting vector, $\mathbf{S} = E_x B_y \hat{\mathbf{z}}$. Using the formula [19]

$$\langle \mathrm{Re}(A\mathrm{e}^{-i\phi})\mathrm{Re}(B\mathrm{e}^{-i\phi})\rangle = \frac{1}{2}\mathrm{Re}(AB^*) \quad (34)$$

to average over the phase $\phi = \Omega x^+$ one finds the intensity

$$\langle S\rangle = |\psi_0|^2/2 = \frac{\hat{I}}{1+\zeta^2}\, \mathrm{e}^{-2\rho^2/(1+\zeta^2)} \equiv I(\rho,\zeta) , \quad (35)$$

where we have defined the intensity amplitude $\hat{I} = |\hat{E}|^2/2$. Dividing by the Sauter-Schwinger value $I_S \equiv E_S^2$ we finally obtain a space-time dependent, dimensionless intensity distribution,

$$\epsilon^2(\rho,\zeta) \equiv \frac{\hat{\epsilon}^2}{1+\zeta^2}\, \mathrm{e}^{-2\rho^2/(1+\zeta^2)} . \quad (36)$$

In view of our adiabaticity assumption we can find the phase shift generalising (26) as the integral

$$\Delta\phi(\rho) = \frac{4\alpha}{15}\frac{z_{0,L}}{\lambda_X}\int_{\zeta_1}^{\zeta_2} d\zeta\, \epsilon^2(\zeta,\rho) . \quad (37)$$

We have taken the Rayleigh length $z_{0,L}$ as the longitudinal unit of length. If we integrate over this Rayleigh length, then $\zeta_1 = -\zeta_2 = -1/2$. It seems wise to extend the integration over all of the pulse which we approximate by integration from minus to plus infinity. In this case the integral can be done analytically upon substituting $\zeta = \tan u$ and employing formula 9.6.16 of [20]. This results in the rather simple expression

$$\Delta\phi(\rho) = \frac{4\pi\alpha}{15}\frac{z_{0,L}}{\lambda_X}\, \hat{\epsilon}^2 I_0(\rho^2)\, \mathrm{e}^{-\rho^2} \equiv \Delta_0\, I_0(\rho^2)\, \mathrm{e}^{-\rho^2} , \quad (38)$$

I_0 denoting a modified Bessel function. The profile (38) is displayed in Fig.4. Its full width at half maximum (FWHM) is given by the beam waist radius corresponding to $\rho = 1$.

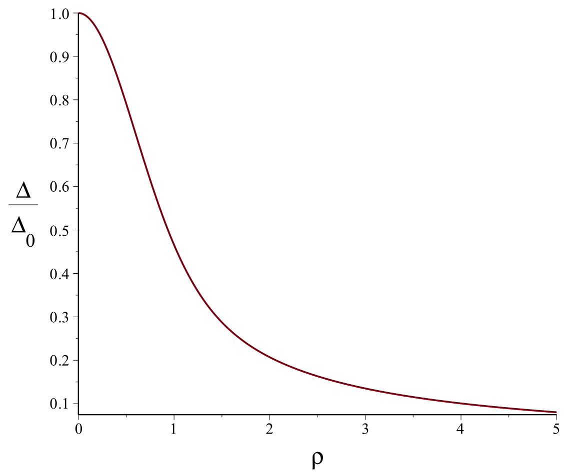

Fig.4: Transverse profile of the phase shift (38).

The phase shift (38) is experienced by a beam that passes at a distance (or impact parameter) ρw_0 from the optical beam (z) axis. Any collection of measurements will thus yield a phase shift averaged over dimensionless impact parameter ρ . Taking a uniform mean across the optical waist results in

$$\Delta_1 \equiv \frac{1}{\pi}\int_0^{2\pi} d\varphi \int_0^1 d\rho\, \rho\, \Delta\phi(\rho) \simeq 0.674\, \Delta_0 . \quad (39)$$

This amounts to assuming that the XFEL waist is much larger than the optical waist $w_{0,\mathrm{X}} \gg w_{0,\mathrm{L}}$ (so that the X-ray intensity is roughly constant across the optical waist) and that contributions outside the optical waist are negligible. It seems more realistic to assume $w_{0,\mathrm{X}} \simeq w_{0,\mathrm{L}}$ and average with a weight given by the transverse profile of the XFEL,

$$\Delta_2 \equiv 2\int_0^\infty d\rho^2\, \mathrm{e}^{-2\rho^2}\, \Delta\phi(\rho) = \frac{\Delta_0}{\sqrt{2}} \simeq 0.707\, \Delta_0 . \quad (40)$$

It is reassuring to note that the values (39) and (40) are close to each other and only yield a mild suppression of order one compared to on-axis probe rays with phase shift Δ_0. However, the ellipticity is quadratic in $\Delta\phi$, so that, in the end, one does lose a factor of about two upon replacing plane waves by Gaussian beams.

4 Discussion and Conclusion

With currently available technology one can achieve an ellipticity signal of order $\delta^2 \simeq 10^{-11}$, cf. (27) and the discussion of the previous section. Whether this small signal becomes observable depends on the progress in X-ray polarimetry. The current state of the art are polarisation purities of 2.4×10^{-10} and 5.7×10^{-10} for 6.457 and 12.914 keV X-rays, respectively [21]. The authors of this study are optimistic that a further improvement by an order of magnitude is possible without too much effort [22]. This suggests that vacuum birefringence could be observed in the near future at planned facilities such as the Helmholtz International Beamline for Extreme Fields (HIBEF) at DESY, Hamburg.

References

[1] W. Heisenberg and H. Euler, Z. Phys. **98**, 714 (1936) [physics/0605038].

[2] H. Euler and B. Kockel, Naturwiss. **23**, 246 (1935).

[3] B. de Tollis, Nuovo Cim. **35**, 1182 (1965).

[4] O. Halpern, Phys. Rev. **44**, 855 (1934).

[5] D. Bernard, F. Moulin, F. Amiranoff, A. Braun, J. P. Chambaret, G. Darpentigny, G. Grillon and S. Ranc *et al.*, Eur. Phys. J. D **10**, 141 (2000) [arXiv:1007.0104 [physics.optics]].

[6] G. M. Shore, Nucl. Phys. B **778**, 219 (2007) [hep-th/0701185].

[7] F. Sauter, Z. Phys. **69**, 742 (1931).

[8] J. S. Schwinger, Phys. Rev. **82**, 664 (1951).

[9] A. I. Nikishov and V. I. Ritus, Sov. Phys. JETP **19**, 529 (1964) [Zh. Eksp. Teor. Fiz. **46**, 776 (1963)].

[10] T. Heinzl and A. Ilderton, Opt. Commun. **282**, 1879 (2009) [arXiv:0807.1841 [physics.class-ph]].

[11] J. S. Toll, PhD thesis, Princeton, 1952, unpublished.

[12] C. Bamber, S. J. Boege, T. Koffas, T. Kotseroglou, A. C. Melissinos, D. D. Meyerhofer, D. A. Reis and W. Ragg *et al.*, Phys. Rev. D **60**, 092004 (1999).

[13] S. S. Bulanov, N. B. Narozhny, V. D. Mur and V. S. Popov, Phys. Lett. A **330**, 1 (2004) [hep-ph/0403163].

[14] A. Gonoskov, I. Gonoskov, C. Harvey, A. Ilderton, A. Kim, M. Marklund, G. Mourou and A. M. Sergeev, arXiv:1302.4653 [hep-ph].

[15] L. W. Davis, Phys. Rev. A **19**, 1177 (1979).

[16] Kirk T. McDonald, 1995; available as http://www.hep.princeton.edu/˜mcdonald/ accel/ gaussian.pdf

[17] Max Born and Emil Wolf, *Principles of Optics*, Cambridge University Press, Cambridge, 2002, seventh expanded edition, reprinted with corrections.

[18] Dieter Meschede *Optics, Light and Lasers*, Wiley-VCH, Weinheim, 2004.

[19] Hartmann Römer, *Theoretische Optik*, VCH, Weinheim, 1994 (in German).

[20] Milton Abramowitz and Irene A. Stegun, *Handbook of Mathematical Functions*, Dover, New York, 1972.

[21] B. Marx et al., Phys. Rev. Lett. **110**, 254801 (2013).

[22] I. Uschmann, private communication, June 2013.

Simulating driving Plasma Wakefield Acceleration with the Diamond Beam

Contact: james.holloway.10@ucl.ac.uk

James Alex Holloway
Department of Physics,
University College London,
WC1E 6BT, United Kingdom

R. Trines
Central Laser Facility,
Rutherford Appleton Laboratory,
OX11 0QX, United Kingdom

P. Norreys
Central Laser Facility,
Rutherford Appleton Laboratory,
OX11 0QX, United Kingdom

M. Wing
Department of Physics,
University College London,
WC1E 6BT, United Kingdom

Abstract

Full-scale, multi-dimensional particle-in-cell simulations to investigate the viability of using the Diamond Light Source 3 GeV electron beam to drive plasma wakefield acceleration have been performed. Micro-bunching the electron beam in the longitudinal direction using a short plasma cell was found to yield high amplitude wakefields (4 GV m^{-1}) in a second plasma cell. An ultra short high intensity laser pulse (E = 1 J, T = 50 fs) was used to heavily seed the self modulation instability to microbunch the Diamond beam. Once driven, the wakefield can be used to accelerate a witness electron beam to higher energies (up to 6 GeV in a single stage).

1 Introduction

Plasma Wakefield Acceleration is a novel particle accelerating technique that achieves high accelerating electric fields up to 1000 times greater than those achieved in conventional radio frequency accelerators [1, 2]. In RF accelerators, electric fields in excess of 100 MVm^{-1} can ionise the metal cavity wherein the particles are accelerated, destroying the accelerator. This limits the amount of energy gained per meter, which means that in order to further the energy frontier for lepton colliders one has to increase the distance over which beams are accelerated. This is not always financially feasible. In Plasma Wakefield Acceleration, the beam is accelerated within a plasma. Being ionised already, the plasma is resistant to further destruction and acts to shield the high amplitude electric fields.

Plasma Wakefield Acceleration requires a driver beam to generate the wakefield within the plasma. A witness beam of charged particles is then injected into the back of the wakefield where it gains energy as it co-propagates with the wakefield [3, 4, 5, 6]. For a charged particle beam to effectively drive a wakefield it has to be smaller than the plasma wavelength in both the propagation and transverse directions. Conventional beams tend to be larger than the plasma wavelength and must be treated. In the simulations presented, the electron beam generated in the booster section of the Diamond Light Source (referred to hereafter as the Diamond beam) at the Rutherford Appleton Laboratory is first longitudinally microbunched by a laser-driven high amplitude wakefield in a short plasma cell. It then goes on to drive a high amplitude wakefield itself in a second plasma cell over a longer distance than the laser pulse could achieve. These simulations will contribute to the proposal to perform a plasma wakefield acceleration experiment driven by the Diamond beam for driving an X-ray Free Electron Laser.

2 Microbunching electron beam

Parameter scans were performed on the high performance computer SCARF: Lexicon-2 over numerous parameters to optimise the set up; including the density of the plasma, width vs temperature of the Diamond beam, spacing and length of the two cells and various laser parameters. Initial simulations showed that a wakefield of 1.8 GVm^{-1} applied to the Diamond beam over several centimeters would fully microbunch the beam.

Figure 1 shows a shortened Diamond beam being microbunched over 4 cm of propagation by a laser-driven wakefield. A shortened Diamond beam was implemented as simulating the full beam was too computationally demanding for the parameter scan. The initial profile of the beam was a bi-Gaussian, as shown in the top of Figure 1. Electrons in focussing regions have formed the microbunches whilst electrons in the de-focussing regions have been transversely expelled (circular formations in the central plot). The microbunches are spaced lambda apart which is crucial for them to resonantly excite the wakefield in the second plasma stage. The microbunches have also had their peak number density enhanced as a result of co-propagating with focussing regions.

This treatment of the beam was achieved by driving a 1.8 GVm^{-1} wakefield (shown in Figure 2). This wakefield was driven by an ultra short high power laser pulse whoes parameters are given in Table 2. Figure 2 shows both the longitudinal electric field (top) and the transverse electric field (bottom). The focussing regions of the

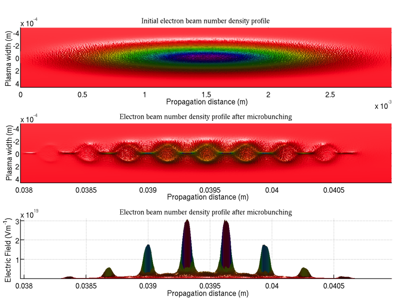

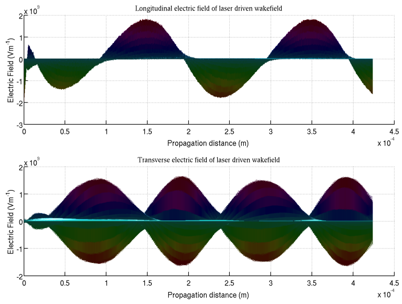

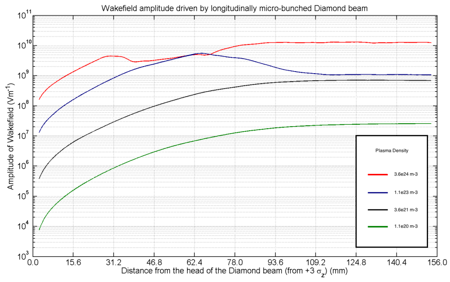

Figure 1: (Left) Short Diamond beam number density before propagating through the first plasma cell (top) and after (middle and bottom).

Figure 2: (Middle) Wakefield driven by ultra short laser pulse. The top plot shows the longitudinal electron fields of the wakefield whilst the bottom shows the transverse fields responsible for the microbunching of the short Diamond beam. Laser parameters found in Table 1.

Figure 3: (Right) Amplitude of wakefield driven by microbunched full Diamond beam for four plasma densities across the length of the microbunch train.

Table 1: Short Diamond beam parameters

Parameter	Value
E	3 GeV
σ_r	132 μ m
σ_z	600 μ m
ϵ	140 nm rad
N	2 nC

Table 2: Drive laser parameters

Parameter	Value
E	1 J
τ	50 fs
σ_r	$\sqrt{2}/k_p$
λ	1.06 μ m

wakefield, where the microbunches form, sit between the accelerating and decelerating regions. The rear of the microbunches experience the accelerating regions whilst the head experience the decelerating region. After co-propagation within these regions an energy spread is imparted upon the microbunches. This is another important quality of the treated beam as this energy spread can be used to longitudinally compress the microbunches using magnetic chicanes, further enhancing the beam's wakefield driving capability.

3 Driving a wakefield with microbunched beam

With the microbunching demonstrated for a short Diamond beam, a parameter scan of the plasma density of the second stage was performed. To model the modulated full length Diamond beam, a longitudinal sinusoidal modulation was applied to the bi-Gaussian envelope. As the plasma density was increased the plasma wavelength, and therefore the required spacing of the microbunches, decreased. For a self consistent scan, the period of the sinusoidal modulation was matched to the plasma wavelength, generating microbunches of the correct spacing.

Figure 3 shows the amplitude of the wakefields driven by the microbunched full length Diamond beam as a function of distance from the head of the beam - or first microbunch. The amplitude of the wakefields ramp up as successive microbunches resonantly excite the wakefields, achieving 4 GVm^{-1} at 3.6 x 10^{24} m^{-3} after 30 mm. However, it is seen that the growth of the wakefield is disrupted after this point. The wakefield growth in plasma density n_e = 1.1 x 10^{23} m^{-3} (blue line) does not seem to recover whereas the wakefield in the denser plasma (red line) seems to. Further investigation shows that this is caused by the plasma ions oscillating within the wakefield. Once the ions start to oscillate the system becomes that of a coupled oscillator i.e. chaotic motion ensues and the wakefield is destroyed. Although the red line seems to show high electric fields returning after the disruption, closer examination reveals that there were no distinct wakefields in which to accelerate charged particles.

Ion motion can be suppressed by decreasing the charge to mass ratio of the ion – typically accomplished by choosing a heavier element to ionise. Xenon was chosen for this simulation set as it is the heaviest non-radioactive noble gas. Ion motion can also be suppressed by shortening the chain of microbunches exciting the wake. This ramps up the wakefield more quickly and leaves less time for the ions to move. Longitudinal compression of the Diamond beam is not feasible, so ion motion limits the maximum wakefield driven by the Diamond beam to 4 GVm^{-1}.

From the presented simulations and others a parameter optimisation study of the laser driver and plasma has been performed and a high resolution large simulation of the full Diamond beam propagating through both plasma stages is currently underway. The aim of the optimisation study was to microbunch the Diamond beam with modest laser parameters whilst achieving the 4 GVm^{-1} wakefields in the second plasma stage.

4 Conclusion

Microbunching of a conventional electron beam using a laser driven wakefield over centimetres of propagation has been shown in simulations. Ion motion proves to limit the amplitude of the wakefield driven by a long, mirobunched beam. The microbunched Diamond beam has driven wakefields of 4 GVm^{-1} over a range of plasma densities. Treating conventional beams to become effective plasma wakefield drivers in this way could prove a financially feasible method of generating higher energy beams at current facilities, allowing current light sources to generate harder X-rays from the existing infrastructure.

References

[1] W.P.Leeman *et al.*, Nature Physics 2, 696 (2006).

[2] I.Blumenfeld *et al.*, Nature 445, 741 (2007).

[3] A. Modena, *et al.*, Electron Acceleration form the breaking of relativistic plasma waves. Nature377, 606-608 (1995).

[4] D. Gordon *et al.*, Observation of electron energies beyond the linear dephasing limit from a laser-excited relativistic plasma wave. Physical Review Letters. 80, 2133-2136 (1998).

[5] S. Mangles *et al.*, Monoenergetic beams of relativistic electrons from intense laser-plasma interactions. Nature 431, 535-538 (2004).

[6] C. G. R. Geddes *et al.*, High quality electron beams from a laser wakefield accelerator using plasma-channel guiding. Nature 431, 538-541 (2004).

[7] N. Barov *et al.*, Propagation of short electron pulses in plasma channel. Nature Physical Review Letters, 80, 81-84 (1998).

Effect of collisions on amplification of laser beams by Brillouin scattering in plasmas

Contact *kathryn.humphrey@strath.ac.uk*

K. Humphrey, D. Speirs

SUPA, Dept. of Physics, University of Strathclyde
Glasgow, G4 0NG, UK

R. Trines, P. Norreys, R. Bingham

STFC Rutherford Appleton Laboratory
Didcot, OX11 0QX, UK

R.A. Cairns

School of Mathematics and Statistics, University of St. Andrews
St. Andrews, Fife, KY16 9SS, UK

L.O. Silva, F. Fiúza

GoLP/Centro de Física dos Plasmas, Instituto Superior Técnico
1049-001 Lisboa, Portugal

Abstract

We report on particle-in-cell simulations of energy transfer between a laser pump beam and a counter-propagating seed beam using the Brillouin scattering process in uniform plasma including collisions. The results presented show that the ion acoustic waves excited through naturally occurring Brillouin scattering of the pump field are preferentially damped without affecting the driven Brillouin scattering process resulting from the beating of the pump and seed fields together. We find that collisions and the effects of Landau damping allows for a more efficient transfer of energy between the laser beams and a significant reduction in the amount of seed pre-pulse produced.

Introduction

The study of parametric instabilities with relevance to interacting laser beams in plasma is of interest to many applications. These include: using Brillouin scattering in plasmas as an amplification technique to generate short and intense light pulses, the study and understanding of complex laser plasma interactions and induced power transfer between adjacent laser beams as a means of controlling the symmetry of fuel capsule implosion for inertial confinement fusion experiments [1, 2]. Interest in this area has grown due to the potential of similar amplification techniques such as the production of picosecond, kilojoule and petawatt pulses via Raman scattering [3, 4, 5, 6] and the interaction of multiple laser beams, leading to cross beam energy transfer (CBET), in inertial confinement fusion experiments on the NIF [7, 8]. A study of laser amplification via SBS was conducted by Andreev et. al. [9], however this work ignored the effects of collisions. Due to the relatively high densities required, typically above one quarter of the critical density, to prevent other processes such as Raman scattering dominating the Brillouin scattering mechanism it is anticipated that collisions will play a significant role in this energy transfer process.

Simulations

The energy transfer between two counter-propagating laser pulses was simulated numerically in 1D using the fully relativistic OSIRIS particle-in-cell code [10] and was constructed as follows. A pump laser of intensity 10^{16} Wcm^{-2} corresponding to a laser wavelength of 1µm was injected in to a plasma column of length $650c/\omega_0$ with the realistic mass ratio for ions to electrons of $m_i/m_e = 1836$ used. The plasma temperature ratio of $ZT_e/T_i = 50$ where $Z = 1$ and $T_e = 500$eV was chosen in order to render Landau damping of the IAW negligible. In all cases the density was chosen slightly above the quarter critical level at $0.3n_c$ in order to mitigate mode competition from Raman scattering which occurs when the density is $0.25n_c$ or below. The seed pulse, of intensity 10^{15} Wcm$_{-2}$ and a full width at half maximum (FWHM) of 100ps with a sin^2 shape, was launched at the instant the pump pulse had traversed the length of the plasma. A frequency mismatch between the pump and seed laser pulses was also introduced, with the seed pulse frequency being downshifted by an amount equal to the ion acoustic frequency. The pulses are counter propagating through the plasma with the pump pulse travelling from right to left through the simulation box. The time step for integration is $\Delta t = 0.04\omega_0^{-1}$ and the spatial resolution of the simulations is of the order of the Debye length with 100 particles per cell. In the simulations where collisional processes were included these were calculated self-consistently by OSIRIS for a reference plasma density of $3\text{x}10^{20}$ cm^{-3} corresponding to a group speed of approximately 0.84c for both pulses.

Figure 1 shows the transverse electric field ω_p t = 1840 as the seed and pump fields interact via stimulated Brillouin scattering for the case where collisional effects are neglected. Energy transfer from the pump to the seed is observed, whilst the seed duration is approximately constant avoiding amplification via compression of the pulse. After approximately $1840\omega_p^{-1}$ the seed pulse reaches maximum amplitude, after which the energy transfer process begins to degrade and the pulse loses its integrity. It can clearly be seen that the pump field is significantly depleted behind the leading edge of the seed indicating that a significant fraction of the available energy in the pump field has been transferred to the seed. It is also noted, however, that there is a large proportion of seed pre-pulse generated when collisional effects are neglected which is particularly unfavorable for use in laser-plasma wave amplification. The formation of this pre-pulse is as a direct result of the pump/seed interaction as no pre-pulse formation is observed when a single laser pulse is utilized.

Analysis of the corresponding phase space plot for this process strongly indicates the excitation and growth of a number of IAW's associated with the Brillouin scattering mode. Figure 2 shows phase space plots for the plasma ion population at ω_p t = 1840, when the seed has reached maximum intensity. On the left hand side of the plot in figure 2 the IAW corresponding to the driven process, resulting from the beating of the seed and pump fields together, is seen to be excited and grow steadily until a time of t = $1840\omega_p^{-1}$, commensurate with the saturation of the energy transfer between the seed and pump. It can also be seen, however, that in addition to the excitation of the beat ion acoustic wave associated with the driven process a number of other, naturally occurring, IAW's are also excited. These waves can be seen to emanate from the RHS of the simulation volume and are due to the pump laser undergoing naturally occurring stimulated Brillouin scattering before the pump/seed pulse interaction. Without collisional damping, the threshold for stimulated Brillouin scattering is effectively zero which results in growth of ion acoustic waves and subsequent depletion of the pump wave before the pump and the seed overlap as the pump drives up ion-acoustic waves and generates a backward propagating scattered wave. This has an adverse effect on the pump/seed energy transfer efficiency.

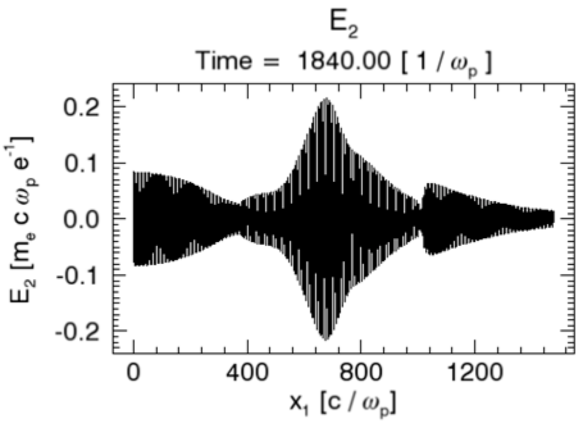

Figure 1. Transverse electric field profile at ω_p t = 1840 for a PiC simulation with collisional effects neglected.

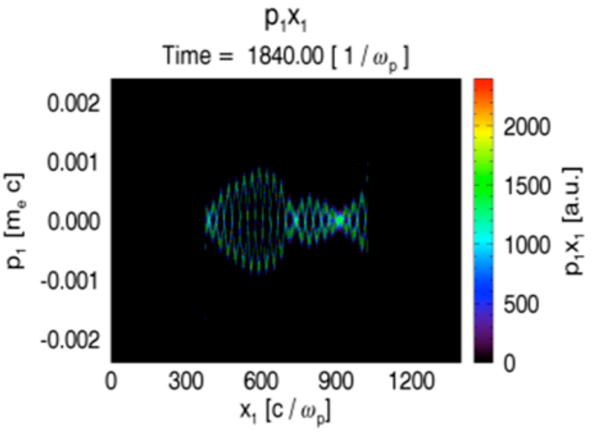

Figure 2. Ion phase space plot at ω_p t = 1840 for a PiC simulation with collisional effects neglected.

Analysis of the effect of including collisional processes into the simulation setup can be seen in figure 3. Upon comparison of the transverse electric field plot to the plot in figure 1, associated with the collisionless setup, it can be seen that there are some significant differences. It can be seen that the growth of the energy transfer process is slower; meaning the seed pulse takes longer to reach maximum amplitude. Due to this reduced growth, the resultant seed has a longer duration as it takes longer to deplete the pump field. As a result of this the pulse has split into a number of beamlets, resulting in a marginal decrease in the final seed amplitude from that of the collisionless case. The efficiency of the process is found to be 10% higher and this is attributed to the fact that the Brillouin scattering process resulting from the pump field is no longer able to prematurely deplete the energy available for transfer to the seed pulse causing degradation in the energy transfer process. Again it is seen that the portion of the pump laser field which has interacted with the seed pulse is significantly depleted indicating that the energy transfer mechanism remains efficient with the thermal effects included in the code. Of particular interest is the significant reduction in the volume of seed pre-pulse generated from stimulated Brillouin scattering when the collisional processes are accounted for. The introduction of collisions therefore provides a significant improvement in the contrast of the laser beam with a very small sacrifice in the resultant laser amplitude, compared with the same pump length, for amplified pulses resulting from stimulated Brillouin scattering.

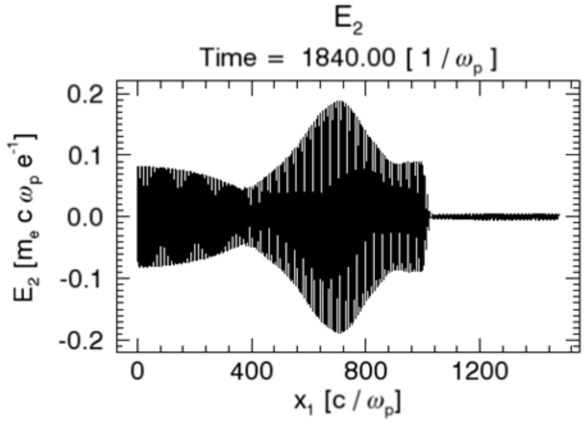

Figure 3. Transverse electric field profile at ω_p t = 1840 for a PiC simulation with collisional effects included

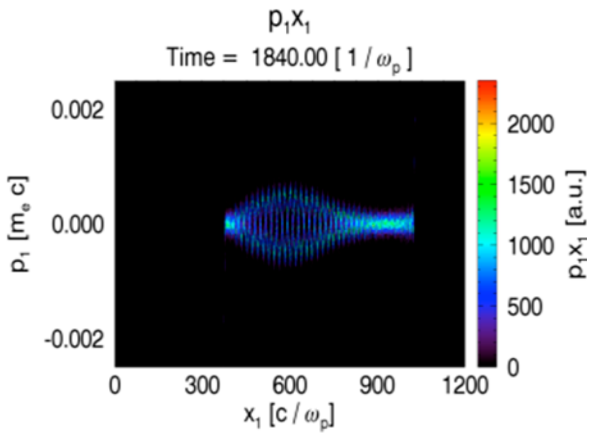

Figure 4. Ion phase space plot at ω_p t = 1840 for a PiC simulation with collisional effects included.

The most significant difference between the two cases can be observed from figure 4, when compared directly with the plot at the same time iterations in figure 2, where it can be seen that the naturally growing IAW's previously seen on the RHS of the simulation box have vanished. This is due to the fact that by including collisional processes into the simulation we encounter a threshold for the normal three-wave scattering process that prevents mode competition between the beat-wave driven and naturally occurring Brillouin scattering mechanisms. In the absence of collisions there is no such threshold meaning that both the naturally occurring three-wave Brillouin scattering and the beat wave Brillouin scattering process are present. By damping the unwanted normal three-wave Brillouin process, resulting from the scattering of the pump field before the pump/seed laser interaction, premature depletion of the pump laser can be minimized ensuring that the energy available for exchange between the pump and seed lasers is maximized. In addition to the difference in growth rates of the IAW's generated from both the collisionless and collisional simulations, an analysis of the individual IAW oscillations generated from both studies of Brillouin scattering show that in both cases particles are accelerated, indicating the initial signs of wave breaking causing the onset of the saturation of the energy transfer mechanism [20].

Conclusions

In summary we have investigated the effect of collisional processes on the energy transfer between laser pulses by stimulated Brillouin scattering. We have shown that, for a constant pump to probe ratio, collisional effects damp the normal three-wave Brillouin scattering process ensuring that the pump laser is unable to scatter before interaction with the seed pulse. In addition we have observed the introduction of collisions results in an increase in the efficiency of stimulated

Brillouin scattering and a significant increase in the contrast of the resultant seed laser beam. These are significant new results and this work has important consequences for the future of ultra-high intensity laser systems and their applications towards pulse energy transfer and amplification.

Acknowledgements

The authors would like to thank the OSIRIS consortium for the use of OSIRIS and the STFC Centre for Fundamental Research for their support. Simulations were carried out on the Scarf-Lexicon Cluster (STFC RAL).

References

1. J. Lindl et al., Phys. Plasmas **11**, 339 (2004).
2. S. H. Glenzer et al., Nature Phys. **3**, 716 (2007).
3. R. M. G. M. Trines et al., Phys. Rev. Lett. **107**, 105002 (2011).
4. R. M. G. M. Trines et al., Nature Phys. **7**, 87 (2011).
5. G. Shvets et al., Phys. Rev. Lett. **81**, 4879, (1998).
6. V. M. Malkin et al., Phys. Rev. Lett. **82**, 4448, (1999).
7. W. L. Kruer et al., Phys. Plasmas **3**, 382 (1996).
8. R. K. Kirkwood et al., Phys. Rev. Lett. **76**, 2065 (1996).
9. A. Andreev et al., Phys. Plasmas **13**, 053110 (2006).
10. R. A. Fonseca et al., In P.M.A. Sloot et al., editors, ICCS 2002, LNCS **2331**, pp. 342-351 (2002).

An R-matrix with pseudo-states (RMPS) approach for single photon double ionization of the He-like Li^+ ion

Contact *b.mclaughlin@qub.ac.uk*

Brendan M McLaughlin[1] **and James F McCann**[1]

[1]*Center for Theoretical Atomic and Molecular Physics (CTAMOP), School of Mathematics and Physics, Queen's University Belfast, Belfast BT7 1NN, UK*

Connor P Ballance[2]

[2]*Physics Department, 206 Allison Laboratory, Auburn University, Auburn AL 36849-5311, USA*

Introduction

The R-matrix with pseudo-state (RMPS) method [1] to model single photoionization processes, benchmarked against dedicated synchrotron light source measurements [2,3], is exploited and extended to single photon double ionization cross-sections for the He-like, Li^+ ion. We investigate these processes from both the ground state and the excited 1s2s $^{1,3}S$ metastable levels of this He-like system. Comparisons of the results from the R-matrix plus pseudo-state (RMPS) method are made with other approaches such as time-dependent close-coupling (TDCC) [4], B-splines [5] and the convergent close-coupling (CCC) [6]. Excellent agreement with other theoretical approaches is achieved. For the ground state the peak of the cross section is ~ 2 kilo-barns (Kb) [7], that for the 1s2s ^1S state is ~ 6 Kb and ~ 1 Kb for the corresponding 1s2s ^3S state [8]. All the cross sections for single photon double ionization are extremely small, being in the region of 2 Kb - 10 Kb, or less, rendering their experimental determination extremely challenging [8].

Theory

Photoionization cross-section calculations were performed in *LS*-coupling on the two-electron He-like Li^+ ion using the R-matrix methodology. We use an efficient parallel version of the R-matrix codes. Only a brief summary of the calculations are presented here. The ionization cross sections are determined by summing over all excitations above the ionization threshold, including all single-electron excitations to the pseudo-states as well as doubly excited states. In the present work we use 65 and 80 levels respectively of the residual Li^{2+} ion states using the R-matrix with pseudo-state (RMPS) method introduced by Burke and co-workers for the close-coupling calculations.

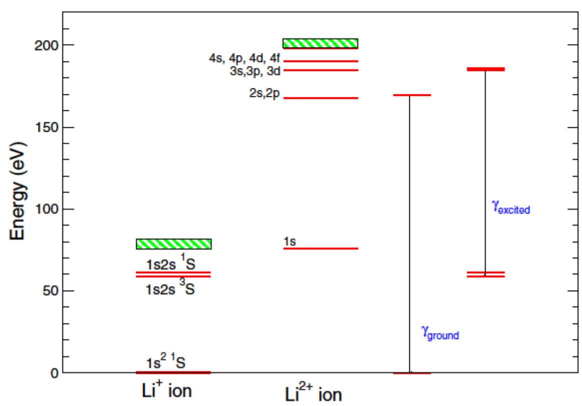

Figure 1: Energy-level diagram illustrating some of the levels for the Li^+ and Li^{2+} ions. The energies are from the NIST tabulations. γ_{ground} and $\gamma_{excited}$ are the lowest photon energies used to calculate the cross-sections for the ground 1s2 ^1S and 1s2s $^{1,3}S$ two excited metastable states respectively.

The basis sets consist of up to n=4 spectroscopic orbital's and nl = 5l....18 l, (where l=0, 1, 2, 3, and 4, i.e. *s, p, d, f* and *g* angular momentum) correlation/pseudo orbital's of Li^{2+} to represent the target wavefunctions. Basis set RMPS1 has n=4 spectroscopic orbital's and nl = 5l....15l correlation/pseudo orbital's, whereas for basis set RMPS2, we have expanded the pseudo-state representation of the continuum as, nl = 5l....18l correlation/pseudo orbital's along with retaining the n=4 spectroscopic orbital's in the basis. All of these hydrogenic orbitals were determined using the AUTOSTRUCTURE program for the Li^{2+} ion.

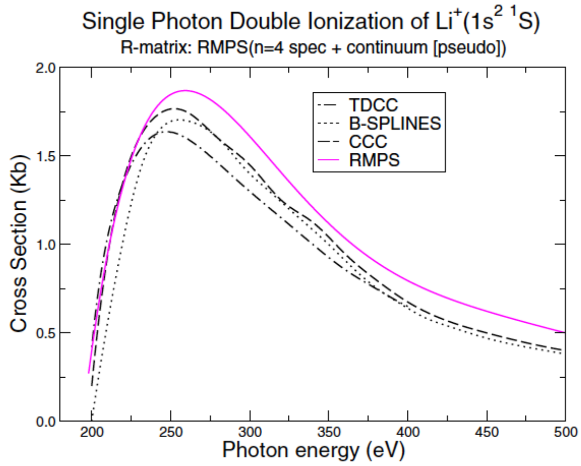

Figure 2: Theoretical cross sections (Kb) for the single-photon double-ionization of Li^+ ions from the ground-state for the photon energy range 200 eV to 500 eV. Results from the present R-matrix plus pseudo-states (RMPS: solid line), the time-dependent close-coupling (TDCC: dot-dashed line), convergent close-coupling (CCC: dashed line) and B-splines (dotted line) methods are included for comparison purposes.

For photoionization of this He-like system, 120-continuum orbitals were used and double-electron promotions from specific base configuration sets described the (Li^{2+} + e^-) scattering wavefunction in the RMPS calculations. In our previous work on single photon, single electron ionization [2,3] an energy mesh size of 13.6 μeV was required to resolve all the fine resonances in the PI cross sections for resonances lying below the single ionization threshold. Here, since we are interested in processes above the ionization threshold a broader mesh size was used of 0.02 Rydbergs (272 meV). For the ionization processes studied here we use models differing only in the size of the basis included in the close-coupling calculations, as a means of checking the convergence of our results. These basis sets we designate as follow; RMPS1, in which we restrict the pseudo-state basis to nl = 5l....15l and RMPS2, where we extend the pseudo-state basis to nl = 5l....18l, thus allowing for checks to be made on convergence of the method. For the case of a two-electron system and the single photon double detachment process in H^-, we note that a smaller pseudo-state basis set (n=1 - 4 physical, 5 - 14 pseudo-states, with *s, p, d, f* and *g* angular momentum) within the RMPS approach [9] reproduced cross section results obtained using an extended pseudo-state basis (n=1 - 4 physical, 5 - 38 pseudo-states, with *s, p, d* and *f* angular momentum) within the Intermediate Energy R-matrix Method (IERM) method [10].

Results

In figure 2 it can be seen that the present RMPS results are in closer agreement with the convergent close-coupling (CCC) approach and the B-splines methods at all energies above 250 eV and merge to the CCC and B-splines results at photon impact energies above about 500 eV.

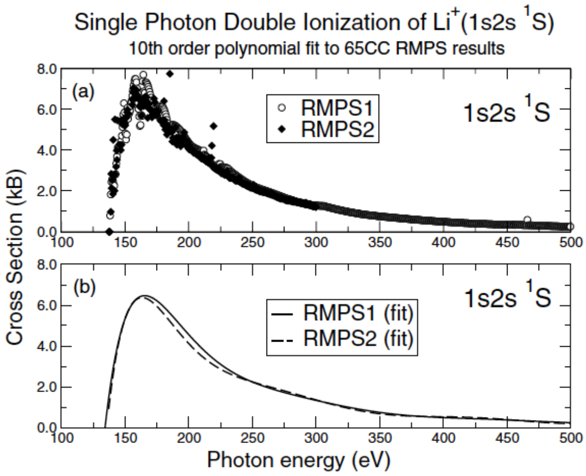

Figure 3: Theoretical cross sections (Kb) for the single-photon double-ionization from the $Li^+(1s2s\ ^1S)$ metastable state for the photon energy range 100 eV to 500 eV are illustrated. (a) R-matrix with pseudo-states (RMPS) method from two the different basis size RMPS1 and RMPS2 are shown to illustrate the convergence. (b) 10th-order polynomial best fits to the raw data from the 65-state model are shown, solid line, basis RMPS1, and the 80-state, dashed line, basis RMPS2.

Double ionization calculations were performed varying the size of the basis set used in the close-coupling approach for the single photon double ionization from the $Li^+(1s2s\ ^1S)$ metastable state. In figures 3 (a) and 3(b), cross section results from different basis set size, designated respectively as RMPS1 and RMPS2 are shown. We find that the results from the larger basis set gave similar results to those from the smaller basis.

From the results presented in figure 4, for the case of single photon impact double ionization, the singlet metastable state cross section is about a factor of 6 larger at the peak (in cross section) than that from the corresponding triplet metastable state. We note that cross sections obtained from both the RMPS and TDCC methods tend to the same value at impact energies of about 500 eV and beyond, for each of the individual $1s2s\ ^{1,3}S$ metastable states but to different limits.

Conclusions

State-of-the-art theoretical methods were used to study the single photon double ionization of Li^+ ions within the R-matrix with pseudo states (RMPS) approach. Due to the lack of experimental data on these processes we compare the results of our study with those from previous theoretical studies using a variety of different methods in order to gauge the accuracy and quality of our work. Given the validation with experiment of our previous RMPS cross section results on ground state, photo-absorption of Li^+ ions for this He-like system [2,3], and the close agreement with the convergent close-coupling (CCC), the time-dependent close-coupling (TDCC), and B-splines methods, for the ground and excited states, we expect that the present results for single photon double ionization to be of comparable quality as to those for single photoionization. We hope that this current work might provide a stimulus for future experimental work on this complex [8].

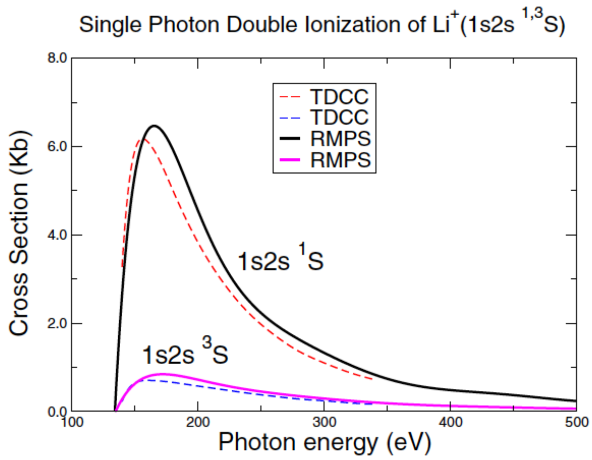

Figure 4: Theoretical cross sections (Kb) for the single-photon double-ionization from the $Li^+(1s2s\ ^{1,3}S)$ metastable states for the photon energy range 100 eV to 500 eV, RMPS method (solid line) along with the time dependent close-coupling TDCC method (dashed line).

Acknowledgements

B. M. McLaughlin acknowledges support by the National Science Foundation through a grant to the Institute for Theoretical Atomic and Molecular Physics (ITAMP) at the Harvard-Smithsonian Center for Astrophysics under the visitor's program where this work was completed. ITAMP is supported by a grant from the National Science Foundation. Thanks are due to Queen's University Belfast for the award of a visiting research fellowship. The computational work was carried out at the National Energy Research Scientific Computing Center in Oakland, CA, USA and on the Kraken XT5 facility at the National Institute for Computational Science (NICS) in Knoxville, TN, USA. The Kraken XT5 facility is a resource of the Extreme Science and Engineering Discovery Environment (XSEDE), which is supported by National Science Foundation Grant No. OCI-1053575.

References

1. C. P. Ballance et al, *J. Phys. Conf. Ser.* **388** 012005 (2012).
2. S. W. Scully et al, *J. Phys. B: At. Mol. Opt. Phys*. **39** 3957 (2006).
3. S W. J Scully et al, J. *Phys. Conf. Ser.* **58** 387 (2007).
4. J. Colgan and M. S. Pindzola, *Int. Rev. At. Mol. Phys*. **1** 161 (2010).
5. H. van der Hart and L. Feng, *J. Phys. B: At. Mol. Opt. Phys.* **34** L601 (2001).
6. A. S. Kheifets and I Bray, *Phys. Rev. A* **58** 4501 (1998).
7. B. M. McLaughlin and C. P. Ballance, *J. Phys. Conf. Ser* **194** 022088 (2009).
8. B. M. McLaughlin, *J. Phys. B: At. Mol. Opt. Phys.* **46** 075204 (2013).
9. S. Miyake et al, *Astrophys. J.* **709** L168 (2010).
10. M. P. Scott, A. J. McKinnen and M. W. McIntyre, *Phys. Rev. A* **86** 032707 (2012).

Radiation damping of an electron in an intense laser pulse

Contact: adam.noble@strath.ac.uk

Adam Noble
Department of Physics,
SUPA & University of Strathclyde,
Glasgow, G4 0NG, UK

Yevgen Kravets
Department of Physics,
SUPA & University of Strathclyde,
Glasgow, G4 0NG, UK

Samuel Yoffe
Department of Physics,
SUPA & University of Strathclyde,
Glasgow, G4 0NG, UK

Dino Jaroszynski
Department of Physics,
SUPA & University of Strathclyde,
Glasgow, G4 0NG, UK

1 Introduction

Classical electrodynamics can often be regarded as the union of two theories: Maxwell's equations, which describe the evolution of electric and magnetic fields, and the Lorentz force, which determines how charges and currents respond to electromagnetic fields. However, the boundary between these two sectors is hazy, since the charges and currents act as sources to the very fields acting on them. Simultaneously solving for both the fields and the sources is not only mathematically intricate, it presents serious conceptual difficulties, illustrated most clearly for the motion of a point electron.

The fields due to a point charge are singular on the worldline of that charge, so cannot be incorporated directly into the Lorentz force to obtain an equation of motion. However, a careful analysis by Dirac [1] shows that the singularity merely serves to renormalize the electron's mass, and the regular part of the field adds to the external fields, yielding

$$\ddot{x}^a = -\frac{q}{m}F^a{}_b\dot{x}^b + \tau\Delta^a{}_b\dddot{x}^b. \tag{1}$$

Here, q and m are the charge and mass and $\tau := q^2/6\pi m \simeq 6\times10^{-24}$ s the characteristic time of the electron. F_{ab} are components of the external electromagnetic field, $\Delta^a{}_b := \delta^a_b + \dot{x}^a\dot{x}_b$ is the $\dot{x}$-orthogonal projection, and an overdot denotes differentiation with respect to proper time s. We use the Einstein summation convention and raise and lower indices with the metric tensor $\eta_{ab} = \mathrm{diag}(-1,1,1,1)$.

The Lorentz-Abraham-Dirac (LAD) equation (1) suffers severe problems. It exhibits "runaway" solutions in which the electron rapidly accelerates toward the speed of light. Such solutions can be eliminated, but at the cost of violating causality. As such, many alternatives to (1) have been sought.

The most commonly used description of radiation reaction is that introduced by Landau and Lifshitz (LL) in their textbook [2], which arises from treating the radiation reaction force in (1) as a small perturbation, and discarding terms quadratic and higher in τ, leading to

$$\ddot{x}^a = -\frac{q}{m}F^a{}_b\dot{x}^b - \tau\frac{q}{m}\dot{x}^c\partial_cF^a{}_b\dot{x}^b + \tau\frac{q^2}{m^2}\Delta^a{}_bF^b{}_cF^c{}_d\dot{x}^d. \tag{2}$$

This equation suffers none of the pathologies of (1), and has recently been placed on a firmer mathematical foundation [3, 4]. However, since it depends quadratically on the external fields, we can rapidly pass from regimes where radiation reaction is negligible to situations where it dominates, and the perturbative treatment becomes unreliable. It is in general impossible to compare solutions of (2) to those of (1), so we need an alternative test of the former's applicability.

2 Ford-O'Connell equation

It is generally accepted that the pathologies of (1) result from the point-particle model of the electron. An alternative equation of motion was derived by Ford and O'Connell (FO), by assuming that the electron could be described by a minimal form factor consistent with causality [5]. In an external force per unit mass f, it reads

$$\ddot{x}^a = f^a + \tau\Delta^a{}_b\dot{f}^b. \tag{3}$$

If f is independent of $\dot{x}$, this is equivalent to the perturbative procedure that led to (2), albeit with a different interpretation. However, for the velocity-dependent Lorentz force, it leads instead to the equation

$$M^a{}_b\ddot{x}^b = -\frac{q}{m}(F^a{}_b + \tau\dot{x}^c\partial_cF^a{}_b)\dot{x}^b, \tag{4}$$

where $M^a{}_b := \Delta^a{}_b + \tau G^a{}_b$, with $G^a{}_b = \frac{q}{m}\Delta^a{}_cF^c{}_d\Delta^d{}_b$. It can be shown [6] that, as a matrix acting on $\dot{x}$-orthogonal vectors, M has determinant

$$\det M = 1 + \frac{\tau^2}{2}G^{ab}G_{ab}, \tag{5}$$

which is always positive, so (4) can be solved for the acceleration, and is a viable equation of motion.

It is reasonable to ask why we should be interested in the FO equation. If the electron has the particular structure assumed in its derivation, then it is the exact equation of motion, in the classical limit. If the electron has any other structure (including pointlike), FO is just one more approximation. However, since it is an intermediate step in the derivation from LAD of LL, it can provide information on the validity of the latter, beyond the usual simple arguments. In particular, from (5) LL should only be reliable when

$$\frac{\tau^2}{2} G^{ab} G_{ab} \ll 1. \tag{6}$$

Although this is a necessary rather than a sufficient condition for the validity of LL, it is a scalar condition, and hence can be unambiguously applied, unlike the rather vague requirement that M should be "close to" the unit matrix.

3 Motion in a laser pulse

Radiation reaction is likely to play an important role in upcoming experiments involving the interactions of intense laser pulses with high energy electrons. For this reason, we wish to compare the results of LL and FO in such a scenario. If they agree, this supports their use in such calculations. If they disagree, the predictions of FO might or might not accurately represent the physics, but LL must be wrong.

For simplicity, we model the laser pulse as a plane wave,

$$\frac{q}{m} F_{ab} = \mathcal{E}(\phi)(\epsilon_a n_b - \epsilon_b n_a), \tag{7}$$

where ϵ is the polarization, $n_a = (1, \mathbf{n})$ the (null) propagation direction, and $\frac{m}{q}\mathcal{E}$ the electric field. $\phi := n_a x^a$ is the only spacetime dependence of field, and the polarization and propagation directions satisfy

$$\epsilon \cdot \epsilon = 1, \quad \epsilon \cdot n = 0, \quad n \cdot n = 0. \tag{8}$$

For definiteness we have assumed linear polarization, though the analysis is readily generalized.

In the absence of radiation reaction, well-known solutions exist [7] describing the motion of an electron in the field (7). Analytical solutions describing LL radiation reaction are also available [8, 9].

In the plane wave (7), the FO equation becomes

$$\ddot{\phi} = -\tau \frac{\mathcal{E} + \tau\dot{\phi}\mathcal{E}'}{1 + \tau^2 \mathcal{E}^2 \dot{\phi}^2} \mathcal{E} \dot{\phi}^3, \tag{9}$$

$$\ddot{\xi} = -\dot{\phi} \frac{\mathcal{E} + \tau\dot{\phi}\mathcal{E}'}{1 + \tau^2 \mathcal{E}^2 \dot{\phi}^2} (1 + \tau \mathcal{E} \dot{\xi} \dot{\phi}), \tag{10}$$

where $\xi = \epsilon_a x^a$, a prime denotes differentiation with respect to ϕ and we have assumed the motion takes place in the spatial plane spanned by ϵ and n. The other dynamical component of $\dot{x}$, $\psi = m_a x^a$ with $m_a = (1, -\mathbf{n})$, can be obtained from the normalization condition $\dot{x} \cdot \dot{x} = -1$, which becomes

$$1 = \dot{\phi}\dot{\psi} - \dot{\xi}^2. \tag{11}$$

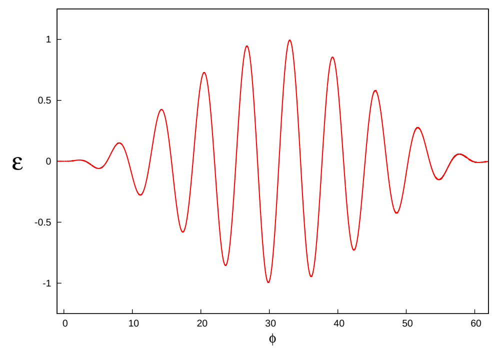

Figure 1: Longitudinal pulse profile (14) for $a_0 = 1$.

It follows that the electron's energy, normalized to mc^2, is given by

$$\gamma = \frac{1}{2}(\dot{\phi} + \dot{\psi}) = \frac{1 + \dot{\phi}^2 + \dot{\xi}^2}{2\dot{\phi}}. \tag{12}$$

Neglecting terms quadratic or higher in τ, (9, 10) reduce to the LL equation, as expected. Indeed, it is clear that the denominator in these equations is precisely $\det M$, so the condition (6) becomes

$$\mathcal{T} := \tau \mathcal{E} \dot{\phi} \ll 1. \tag{13}$$

We are interested in exploring regimes where (13) is violated. To this end, we make the following choice of longitudinal laser profile:

$$\mathcal{E} = \begin{cases} a_0 \sin(\phi) \sin^2(\phi/20) & \text{for } 0 < \phi < 20\pi, \\ 0 & \text{otherwise.} \end{cases} \tag{14}$$

This pulse, illustrated in Fig. (1) for $a_0 = 1$, represents a 10-cycle pulse modulated by a $\sin^2$-envelope. a_0 is the usual intensity parameter ("normalized vector potential"). Units of time have been chosen so that the central frequency is unity: for a laser with $\hbar\omega = 1.55$ eV, this corresponds to $\tau = 1.5 \times 10^{-8}$.

To illustrate the effects of radiation reaction, we consider two cases of an electron colliding head-on with a pulse described by (14). We have the freedom to vary the initial electron energy γ_{in} and the intensity a_0.

In Fig. (2), we plot the Lorentz factor γ for an electron of moderate initial energy $\gamma_{\text{in}} = 100$ colliding with a pulse with intensity parameter $a_0 = 100$. This represents the limit of currently attainable laser intensities. It is clear that, while the radiation reaction has a significant effect on the dynamics, FO and LL are in good agreement. This is unsurprising as (13) is well satisfied in this regime.

To explore a regime where (13) is violated, we consider the highest energy electrons produced in the laboratory ($\gamma_{\text{in}} = 10^5$), colliding with the most intense lasers currently under development ($a_0 = 1000$). In Fig. (3) we

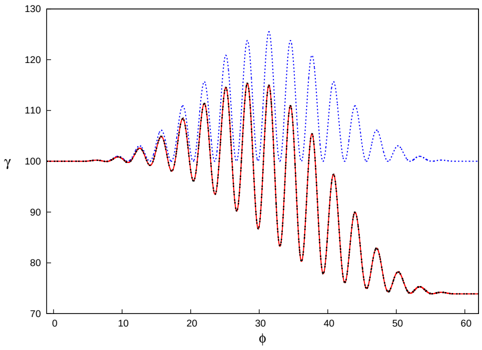

Figure 2: γ against ϕ for an electron of initial energy $\gamma_{\rm in} = 100$ colliding with a pulse of intensity $a_0 = 100$. Dotted blue curve without radiation reaction; solid red curve, with LL radiation reaction; double dotted black curve, with FO radiation reaction.

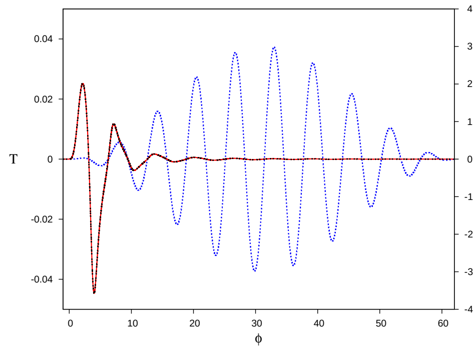

Figure 4: $\mathcal{T}$ against ϕ with and without radiation reaction. Dotted blue curve, right axis, without radiation reaction; solid red curve, left axis, with LL radiation reaction; double dotted black curve, left axis, with FO radiation reaction.

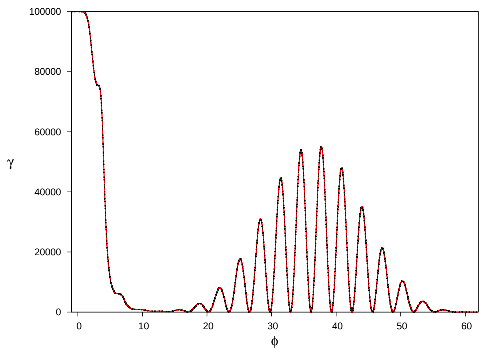

Figure 3: γ against ϕ for an electron of initial energy $\gamma_{\rm in} = 10^5$ colliding with a pulse of intensity $a_0 = 1000$. Solid red curve, with LL radiation reaction; double dotted black curve, with FO radiation reaction.

plot the Lorentz factor γ for this case. It is clear that the evolution is dominated by radiation reaction. However, though (13) appears to be violated, agreement between FO and LL remains excellent. How are we to explain this?

The condition (13) is based on the instantaneous values of ϕ and $\mathcal{E}$. However, the stated values for $\gamma_{\rm in}$ and a_0, which suggested this condition would be violated, refer to the *initial energy* and the *peak intensity*. It is clear from Fig. (3) that the electron loses most of its energy to radiation in the first two cycles, before it has entered the region of high intensity. In Fig. (4), we plot the parameter $\mathcal{T}$ as the electron traverses the pulse. If radiation reaction were ignored, $\mathcal{T}$ would indeed exceed unity; with radiation reaction, it never gets higher than about 0.03 (note the different scales on the two axes). It thus seems that the act of radiating away its energy ensures that the electron remains in a regime where LL is the appropriate equation of motion.

4 Conclusion

The question of how a charged particle interacts with the radiation it emits has vexed physicists for more than a century. Advances in laser technology are turning this problem into a matter of urgent practical concern.

We have explored the Ford-O'Connell description of radiation reaction, and found it a viable equation of motion. It has the advantage that it does not treat the radiation reaction force perturbatively, and can be used to verify the accuracy of the more commonly used Landau-Lifshitz equation.

By analysing the motion of a high energy electron interacting with an ultra-intense laser pulse, we have seen that the energy lost to radiation in the low intensity region of the pulse is sufficient to ensure it never enters a regime where the Landau-Lifshitz perturbative treatment of radiation reaction becomes invalid.

Acknowledgements

We are grateful for support from EPSRC, SUPA and the Cockcroft Institute.

References

[1] PAM Dirac, Proc. R. Soc. A **167** 148 (1938).

[2] LD Landau and E. M. Lifshitz, *The Classical Theory of Fields* (Pergamon, London, 1962).

[3] H Spohn, Europhys. Lett. **50** 287 (2000).

[4] SE Gralla, AI Harte and RM Wald, Phys. Rev. D **80**, 024031 (2009).

[5] GW Ford and RF O'Connell, Phys. Lett. A **157**, 217 (1991).

[6] Y Kravets, A Noble and DA Jaroszynski, to appear.

[7] JW Meyer, Phys. Rev. D **3**, 621 (1971).

[8] A Di Piazza, Lett. Math. Phys. **83**, 305 (2008).

[9] C Harvey, T Heinzl and M Marklund, Phys. Rev. D **84**, 116005 (2011).

The inclusion of gamma-ray photon emission and pair production in simulations of high power laser matter interactions

Contact *christopher.ridgers@york.ac.uk*

C.P. Ridgers

Department of Physics, University of York
Heslington, York, YO10 5DD, UK

C.S. Brady

Centre for Fusion, Space & Astrophysics, University of Warwick, Coventry, CV4 7AL, UK

J.G. Kirk

Max Planck Institut fur Kernphsik
Postfach 10 39 80, 69029, Heidelberg, Germany

T. Blackburn

Clarendon Laboratory, University of Oxford
Parks Road, Oxford OX1 3PU, UK

T.D. Arber

Centre for Fusion Space & Astrophysics, University of Warwick
Coventry, CV4 7AL, UK

A.R. Bell

Clarendon Laboratory, University of Oxford
Parks Road, Oxford, OX1 3PU, Oxford

Introduction

Current high power lasers focus light to such extreme intensities ($>10^{21}$Wcm^{-2}) that electron dynamics in the laser fields can be strongly affected by nonlinear quantum electrodynamics (QED) effects [1]. When an electron is accelerated by such strong laser fields it radiates a significant fraction of its energy as gamma-ray photons. Therefore, the radiation reaction force [2] becomes important in determining the electron's dynamics. Furthermore, the emitted gamma-ray photons can go on to produce electron-positron pairs by interacting with the laser fields. These pairs can emit further photons and the process can run away in a cascade of pair production, similar to that which occurs in pulsar magnetospheres [3].

The importance of QED effects is controlled by the parameter $\eta=E_{RF}/E_s$ [4]. Here E_{RF} is the electric field of the laser in the electron's rest-frame and $E_s=2\pi m_e c^2/e\lambda_c$ is the characteristic field of QED [5]. If QED effects are to be significant one requires $\eta>0.1$. For a 1PW laser pulse with peak intensity 10^{21}Wcm^{-2}, the ratio of the laser field to the critical field $E_L/E_s\sim10^{-4}$. However, QED effects can still be important in the case of a highly relativistic electron, with Lorentz factor $\gamma>>1$, counter-propagating relative to the laser pulse. In the case where $\gamma>>a_0$ ($a_0=eE_L/m_e c\omega_L$ is the strength parameter of the laser wave) $E_{RF}=2\gamma E_L$. For $\gamma>1000$, $\eta>0.1$ is reached. Electron beams of energy >500MeV are regularly created in laser plasma interactions by laser wakefield acceleration [6]. Therefore the nonlinear QED effects described above can be probed in experiments on current 1PW laser systems such as GEMINI, which is a two-beam facility. A typical experiment would use one beam to generate the energetic electrons by laser wakefield acceleration in a gas-jet. The second pulse would be focused to collide with this electron beam. An example simulation of such an experiment is shown in figure 1.

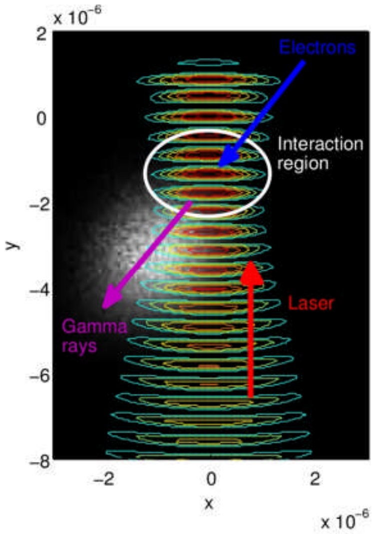

Figure 1. EPOCH QED-PIC (see below for a description of QED-PIC) simulation of a monoenergetic (1GeV) electron bunch propagating at 30^o relative to a counter-propagating laser pulse of peak intensity (10^{21}Wcm^{-2}) and FWHM 30fs.

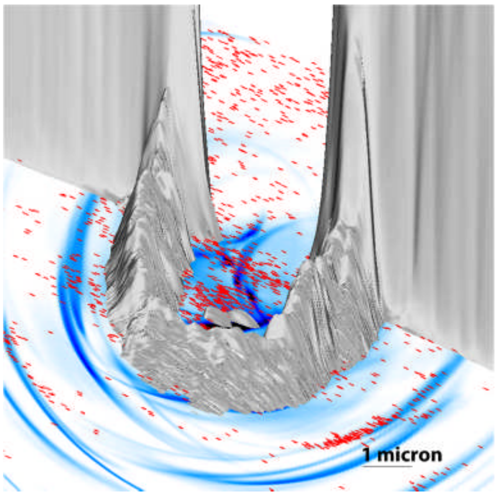

Figure 2. EPOCH QED-PIC simulation of a 12.5PW laser-pulse, FWHM 30fs, striking a solid aluminium target (3D grey). 10% of the laser energy is converted to gamma-ray photons (blue) and a pure electron positron plasma of peak density 10^{20}cm^{-3} is generated. Adapted from [8].

Next generation multi-petawatt laser systems will focus to sufficient intensity to reach $E_L/E_s\sim1/a_0$. The laser pulse imparts energy $\sim a_0$ to the electrons in the plasma generated in the focus. In this case the laser pulse itself can accelerate the electrons in the plasma to high enough energy to reach $\eta>0.1$ and no external acceleration, as was provided by laser wakefield acceleration in the previous case, is required. The QED processes therefore occur in a plasma environment. Here the plasma physics processes set the electromagnetic fields and so the emission rates. Conversely, the emission processes alter the plasma currents and so modify the plasma physics processes. As a result the plasma physics processes and QED emission processes must be considered self-consistently and the state is best described as a QED plasma [7,8]. The results of an example QED-plasma simulation are shown in figure 2. Here, simulations predict that when a 12.5PW laser strikes a solid aluminium target, 10% of the laser energy is converted to gamma-ray photons and a pure electron-positron plasma of density 10^{20}cm^{-3}, seven orders of magnitude denser than currently achievable with lasers [9], is generated.

QED-PIC

In order to simulate QED interactions in laser plasma experiments the important QED emission processes have been included in the particle-in-cell (PIC) code EPOCH. The resulting code will be denoted as a QED-PIC code for brevity. The important emission processes are nonlinear Compton scattering and multiphoton Breit-Wheeler pair production. In the former process an electron or positron emits an energetic gamma-ray photon on interaction with the laser fields. In the latter a gamma-ray photon generates a pair in the laser fields.

The rates of these processes are calculated in the strong-field QED framework [10] where the laser (& plasma) electromagnetic fields are treated as a classical background field. We make the following assumptions about this background field. The ratio of the photon formation length to the laser wavelength is equal to $1/a_0$. We consider interactions where a_0>>1 and so the laser fields can be assumed constant on the length-scale over which emission occurs: the background fields are *quasi-static*. In addition The laser fields are much less than E_s and so the background field is *weak*. Figure 3 shows the domain of laser strength parameter and laser photon energy over which these assumptions are valid, demonstrating that they are valid over the regime of interest for multi-petawatt laser plasma interactions.

Under the quasi-static and weak-field assumptions the rates of photon and pair emission are [4] (in the strong-field QED framework):

$$\lambda_\gamma(\eta) = \frac{\sqrt{3}\alpha_f c}{\lambda_c}\frac{\eta}{\gamma}h(\eta) \qquad \lambda_\pm(\chi) = \frac{2\pi\alpha_f c}{\lambda_c}\frac{m_e c^2}{\hbar\omega_\gamma}\chi T_\pm(\chi)$$

$$\eta \approx \frac{\gamma}{E_s}|\mathbf{E}_\perp + \boldsymbol{\beta}\times c\mathbf{B}| \qquad \chi = \frac{\hbar\omega_\gamma}{2m_e c^2}|\mathbf{E}_\perp + \hat{\mathbf{k}}\times c\mathbf{B}|$$

$$h(\eta) = \int_0^{\eta/2}\frac{F(\eta,\chi)}{\chi}d\chi \qquad T_\pm(\chi) \approx 0.16\frac{K^2_{1/3}(2/3\chi)}{\chi}$$

Here $\boldsymbol{\beta}=\mathbf{v}/c$ is the velocity of the electron, $\mathbf{E}_\perp$ is the background electric field perpendicular to the motion of the electron or photon respectively, $\mathbf{B}$ the magnetic field. $\mathbf{k}$ is the wavenumber of the gamma-ray photon and $F(\eta,\chi)$ is the quantum-corrected synchrotron function [4]

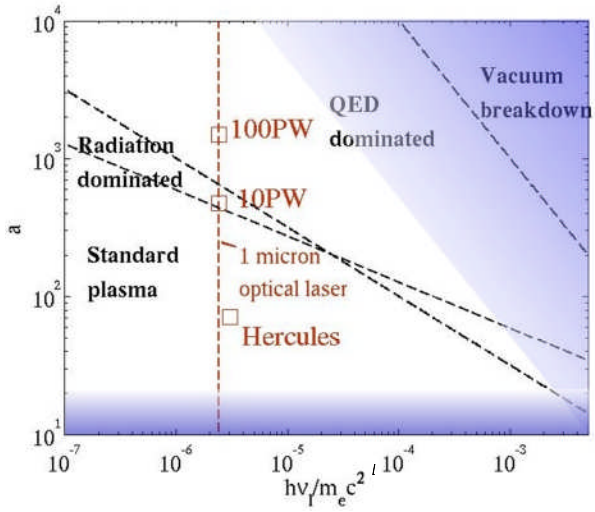

Figure 3. Universal diagram for next-generation laser matter interactions in terms of the strength parameter of the laser wave a_0 and the laser photon frequency h ν. 'Radiation dominated' implies that the radiation reaction force is important in determining the electron's dynamics; 'QED dominated' that quantum corrections to the radiation reaction force and pair production are important [12]. In the 'vacuum breakdown' regime the QED critical field is reached. The quasi-static approximation breaks down in the lower blue shaded region and the weak-field approximation in the upper shaded region. The current most intense laser system 'Hercules' and expected regions of operation of 10PW and 100PW lasers are shown. The model is valid in the important regimes of next-generation laser-matter interactions.

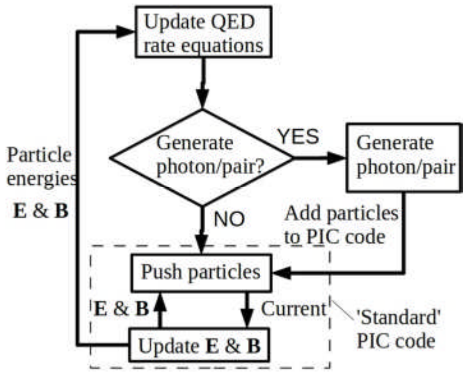

Figure 4. Schematic of a QED-PIC code. The "standard' PIC part of the code is shown

These rate equations are solved by a Monte-Carlo algorithm which captures the quantum stochasticity of the emission [11]. As the laser & plasma fields are treated as classical background fields this Monte-Carlo code is straightforwardly coupled to a PIC code. The resulting QED-PIC code is shown schematically in figure 4.

Conclusions

QED effects can be important in determining the electron dynamics in current high intensity laser matter interaction sin specially arranged experiments, such as the collision of an electron beam and high energy laser pulse. These QED effects will dominate the physics of next-generation multi-petawatt interactions. We have described a scheme for including the important QED emission processes in a PIC code. The resulting QED-PIC code provides an essential tool for understanding laser-matter interactions at today's intensity frontier and beyond.

References

1. A.R. Bell & J.G. Kirk, Phys. Rev. Lett., **101**, 200403 (2008); A.M. Fedotov *et al*, Phys. Rev. Lett., **105,** 080402 (2010)
2. P.A.M. Dirac, Proc. R. Soc. A, **167**, 148 (1938)
3. P. Goldreich & W.H. Julian, Astrophys. J., **157**, 869 (1969)
4. T. Erber, Rev. Mod. Phys., **38**, 626 (1966)
5. F. Sauter, Z. Phys, **69**, 742 (1931); W. Heisenberg & H. Euler, Z. Phys., **98**, 714 (1936); J. Schwinger, Phys. Rev. **82**, 664 (1951)
6. W.P. Leemans *et al*, Nature Phys., **2**, 696 (2006)
7. E.N. Nerush *et* al, Phys. Rev. Lett., **106**, 035001 (2011); C.P. Ridgers *et al*, Phys. Rev. Lett, **108**, 165006 (2012); C.S. Brady, Phys. Rev. Lett., **109**, 245006 (2012);
8. C.P. Ridgers *et al*, Phys. Plasmas, **20**, 056701 (2013)
9. H. Chen *et al*, Phys. Rev. Lett., **105**, 015003 (2010)
10. W.H. Furry, Phys. Rev., **81**, 115 (1951)
11. R. Duclous *et al*, Plas. Phys. Control. Fusion, **53**, 015009 (2011); N.V. Elkina *et al*, Phys. Rev. ST. AB., **14**, 054401 (2011)
12. The demarcations between these regimes are calculated for the case of a single electron at the **B**=0 node of a standing wave produced by counter-propagating, circularly polarized plane electromagnetic waves.

Generation of Super-Ponderomotive Electrons via Direct Laser Acceleration with Longitudinal Electrostatic Fields.

Contact: alex.robinson@stfc.ac.uk

A.P.L.Robinson
Plasma Physics Group,
Central Laser Facility,
STFC Rutherford-Appleton Lab,
Harwell Oxford,
OX11 0QX, UK

A.V.Arefiev
Institute for Fusion Studies,
The University of Texas,
Austin,
Texas 78712,
USA.

1 Introduction

The generation of highly energetic electrons is perhaps one of the most critical aspects of ultra-intense laser-plasma interactions. It underpins a wide range of topics in the field including Fast Ignition (FI) inertial confinement fusion (ICF) [1], proton and ion acceleration [2], x-ray generation, positron production, and even the emerging area of 'strong field' physics [3]. It is therefore important to develop a good understanding of the mechanisms that produce these highly energetic electrons.

In highly underdense plasmas, one can set up powerful wake-fields [4] using laser pulses which can accelerate electrons to energies well in excess of the characteristic energies associated with an electron oscillating in the laser field itself (i.e. $\gamma_{wake} \gg a_0$ and $\gamma_{wake} \gg a_0^2/2$). However this requires one to establish a coherent wake-field over considerable distances (highly feasible in gas jet targets), which is not really possible in the near-critical pre-plasmas associated with solid targets. Also, as one wants to produce copious numbers of energetic electrons in dense target interactions, the wake-field mechanism becomes limtied due to beam-loading.

This lead those interested in pre-plasma region of dense targets to consider Direct Laser Acceleration (DLA) mechanisms as an alternative route to producing highly energetic electrons. The most heavily studied of these is probably the betatron resonance mechanism [5]. Other DLA mechanisms are possible however, and in this article we will report on our recently proposed mechanism [6] which involves longitudinal (i.e. coaxial with the laser propagation direction) electrostatic field.

2 Theory

Consider the dynamics of a single electron in an essentially 1D configuration in which it interacts with a plane electromagnetic wave [7] described by the vector potential, $\mathbf{A} = [0,0,A] = [0,0,A_0\cos(\omega_L\tau)]$, where $\tau = t - x/c$ and ω_L is the wave frequency. The electric and magnetic fields are related to the vector potential via $\mathbf{E} = -\partial_t\mathbf{A}$ and $\mathbf{B} = \nabla\times\mathbf{A}$, so the electric field of this wave is polarized in the z-direction. We also consider the case where a longitudinal electric field, E_x, is present. The equations of motion of the electron that need to be considered are:

$$\frac{dp_x}{dt} = -eE_x + ev_zB_y, \tag{1}$$
$$\frac{dp_y}{dt} = 0, \tag{2}$$
$$\frac{dp_z}{dt} = -eE_z - ev_xB_y, \tag{3}$$
$$\frac{d\gamma}{dt} = -\frac{ev_zE_z}{m_ec^2} - \frac{ev_xE_x}{m_ec^2}. \tag{4}$$

From the definition of τ, one can differentiate to obtain, $d\tau/dt = 1 - v_x/c$, and this can then be used to write the field components as $E_z = -\partial_\tau A$, $B_y = (1/c)\partial_\tau A$. These can then be used to obtain, $p_z = eA$, from Eq. 3, which is one of the key integrals of motion. In the absence of E_x, another integral of motion is obtained from Eq.s 1 and 4, namely $\gamma - p_x/m_ec = 1$ (assuming that the electron is initially at rest). Using this, one obtains $p_x = e^2A^2/2m_ec$ in the $E_x = 0$ case (i.e. the 'free electron' case). If, however, $E_x = -E$ (where E is a positive constant over some region) then we instead have,

$$\frac{d}{d\tau}\left(\gamma - \frac{p_x}{m_ec}\right) = -\frac{eE}{m_ec}, \tag{5}$$

and from this we can see that $\gamma - p_x/m_ec < 1$. We can now re-write Eq. 1 as,

$$\frac{dp_x}{dt} = \frac{1}{R}\frac{e^2A}{m_ec}\frac{dA}{dt} + eE, \tag{6}$$
$$R = \gamma - \frac{p_x}{m_ec} = 1 - \frac{eE}{m_ec}\int d\tau. \tag{7}$$

From Eqs. 6 one can see that the effect of the accelerating electric field will not only be direct acceleration of the electron (similar to wakefield acceleration), but it will also be a reduction of the dephasing rate R. As a result, the electron will gain additional energy from the laser field above that obtained in the free electron case, i.e. it can produce super-ponderomotive electrons. Equation 6 also emphasizes that the '$\mathbf{j}\times\mathbf{B}$' force is not entirely separated from the longitudinal electric force, as the two are linked through the dephasing rate.

To emphasize the additional energy gain, suppose that the electron experiences only a limited acceleration due to E being confined to a s very short spike. Before passing through the spike, $R = 1$, and after passing through the spike $R = 1 - \Delta$, where $\Delta = eE\Delta\tau/m_e c$, but R now remains constant after the spike (where $E = 0$). Eq. 6 can now be directly integrated to obtain,

$$\frac{p_x}{m_e c} = \frac{1}{1-\Delta}\frac{a_0^2}{2}. \quad (8)$$

As $\Delta > 0$, clearly $p_x/m_e c > a_0^2/2$, i.e. the electron is now super-ponderomotive. If Δ is a large fraction of unity, then the electron may achieve energies which a few times in excess of the vacuum limit. Clearly we have a mechanism that can produce super-ponderomotive electrons.

3 Simulations

In actual laser-plasma interactions, we do not have to suppose the existence of a hypothetical additional electric field, as the charge displacement that is naturally caused by the laser pulse will give rise to longitudinal electric fields. On the otherhand, these interactions are highly complex and other adverse effects may affect the proposed mechanism. For example, if the longitudinal electric field does not accelerate the electrons in the direction of the laser pulse, then its effect will be instead to reduce the electron momentum. Clearly self-consistent numerical calculations are required to fully assess the importance of this mechanism in real interactions.

We therefore carried out a parametric study using 1D Particle-In-Cell (PIC) simulations (using the CLF PPG's ELPS code [8, 9, 10]) of 100 fs flat-topped laser pulses with a_0 =3–20 and $\lambda = 1\mu$m interacting with uniform plasma slabs with densities ranging from 0.01–0.5 n_c. We separately tracked the amount of each macroparticle's axial momentum that was due to ev_zB_y and $-eE_x$. A super-ponderomotive macroparticle with a high fraction of its momentum due to ev_zB_y can only have obtained it from the anti-dephasing mechanism. We observed that, across most of the investigated parameter space, a substantial fraction ($>$ 30%) of the electron energy was converted into super-ponderomotive electrons. About 40–60% of the axial momenta of super-ponderomotive electrons was due to ev_zB_y, which shows that the anti-dephasing mechanism is critically important in the generation of these electrons. Figure 1 shows the electron phase space in the form of the momentum fraction due to ev_zB_y against p_x for $a_0 = 20$ and n_e =0.1 n_c at 300 fs. This phase space plot therefore shows both a substantial number of electrons that are super-ponderomotive and that a large fraction of this is due to ev_zB_y, hence the anti-dephasing mechanism must be highly significant in these interactions.

We have also carried out 2D PIC simulations in which we also observed the generation of highly energetic electrons (above the free electron limit) which we believe can only be attributed to the mechanism described here. These simulations will be reported on in detail elsewhere.

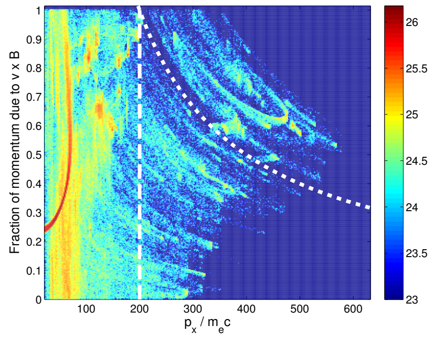

Figure 1: Electron phase space in 1D PIC simulation at 300 fs (see text) shown as p_x versus the fraction of each macroparticle's momentum due to ev_zB_y acceleration only. The dashed vertical line indicates the 'ponderomotive limit', i.e. $m_e c a_0^2/2$, and the dash-dot line represents the point at which the portion due to ev_zB_y is equal to $m_e c a_0^2/2$.

4 Conclusion

We have described a generic mechanism whereby electrostatic fields in plasma, which occur naturally due to charge displacement by the laser pulse, can alter the dephasing rate of electrons in the laser field and launch them on trajectories which achieve super-ponderomotive energies (i.e. $p_x/m_e c > a_0^2/2$). Numerical simulations appear to confirm that this mechanism can be signifcant even in quite simple laser-target configurations. The role of this mechanism in generating highly energetic electrons in the pre-plasmas of solid targets should therefore receive further consideration.

References

[1] M.Tabak et al. Ignition and high gain with ultrapowerful lasers. *Phys.Plasmas*, 1(5), 1994.

[2] S.A.Gaillard et al. *Phys.Plasmas*, 18:056710, 2011.

[3] C.P.Ridgers et al. *Phys.Rev.Lett.*, 108:165006, 2012.

[4] S.P.D.Mangles et al. *Nature*, 431:535–538, 2004.

[5] A.Pukhov, Z.-M.Sheng, and J.Meyer ter Vehn. *Phys.Plasmas*, 6:2847, 1999.

[6] A.P.L.Robinson, A.V.Arefiev, and D.Neely. *Arxiv*, page arXiv:1303.02330, 2013.

[7] T.J.M.Boyd and J.J.Sanderson. *The Physics of Plasmas*. Cambridge University Press, 2003.

[8] A.P.L.Robinson et al. *New J.Phys.*, **10**:013021, 2008.

[9] A.P.L.Robinson, D.Neely, P.McKenna, and R.G.Evans. Spectral control in proton acceleration with multiple laser pulses. *Plasma Phys.Control.Fusion*, **49**:373, 2007.

[10] A.P.L.Robinson et al. *Plasma Phys. Control. Fusion*, **51**:024004, 2009.

Control of Relativistic Electron Beams for Fast Ignition using Elliptical Magnetic Mirrors

Contact: holger.schmitz@stfc.ac.uk

H. Schmitz
Central Laser Facility,
STFC, Rutherford Appleton Laboratory,
HSIC, Didcot, Oxon, OX11 0QX, UK

A. P. L. Robinson
Central Laser Facility,
STFC, Rutherford Appleton Laboratory,
HSIC, Didcot, Oxon, OX11 0QX, UK

Introduction

In order for Fast Ignition to be successful it is extremely important that the energy of the fast electrons is deposited in a small region inside the compressed fuel. Before reaching the fuel core the electrons need to travel for distances of 50–100μm from the point of acceleration by the laser pulse. Thus it is vital that the electrons remain collimated. It is known, however, that the electron beam starts to diverge drastically for laser intensities above $10^{19}\,\mathrm{W\,cm^{-2}}$ [1, 2]. This substanitally decreases the coupling efficiency. The Fast Ignition concept therefore relies on the ability to understand and control the propagation and collimation properties of the fast electron beam.

We present a novel target geometry to guide fast electrons based on self generated magnetic fields at resistivity gradients [3]. When the magnetic field is restricted to a thin layer the electron trajectories will be symmetric with respect to the normal vector. We can, therefore, use mirror optics to design a target geometry that focuses the fast electrons towards the compressed fuel core [4].

In a first step, we provided a proof of concept using 2.5 dimensional collisional PIC simulations of an elliptical mirror. By embedding an elliptical region of high-Z material within a low-Z cladding we show that the magnetic fields generated at the interface indeed collimate the electrons. This is in contrast to earlier investigations where electrons were merely channelled in the high-Z material.

In a second step we performed large scale hybrid simulations with realistic length and time scales [5]. It is found that, under these conditions, the energy deposited in the dense fuel core increases by a factor of 3 to 4 compared to the benchmark case.

PIC Simulations

The simulations were carried out using the relativistic parallel PIC code EPOCH in a domain of 20μm by 20μm represented by a 3072x3072 grid. The target was modeled by a planar slab of 10μm thickness located 7.5μm from the left boundary of the simulation domain. The electron density inside the target was chosen to be $3.011 \times 10^{23}\mathrm{cm}^{-3}$ corresponding to $300 n_{\mathrm{crit}}$ and thus modelling a realistic solid density. The initial electron temperature was set to 100eV. The ions in the bulk of the target have a mass of $m_{\mathrm{bulk}} = m_p$ and a charge of $Z = 1$. An elliptical region in the centre of the target was made from high-Z ions with $m_{\mathrm{highZ}} = 10 m_p$ and $Z = 5$. The ellipse was centred on the rear surface of the target with one focus located on the front surface. This geometry is expected to focus the fast electron beam to a spot at about 10μm behind the target. In a reference run, the high-Z region had a slab geometry with a thickness of 5μm. The target is irradiated by a laser with a vacuum wavelength of $\lambda_0 = 1.05\mu$m, a maximum intensity of $I_0 = 5 \times 10^{19} W\,cm^2$, and a spot size of 5$\mu$m.

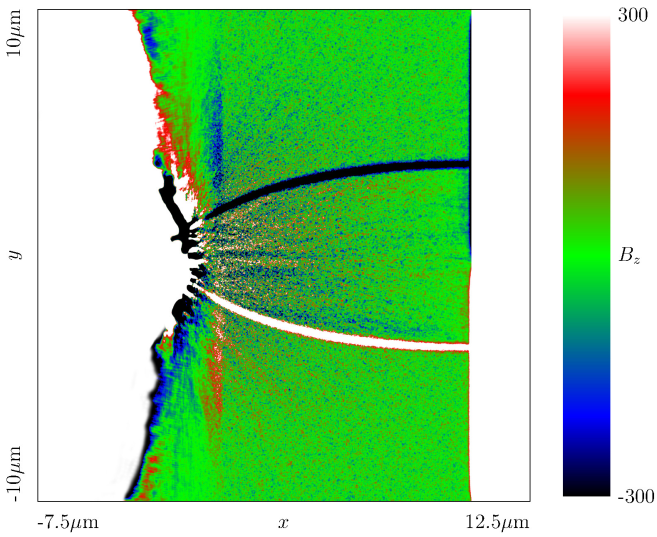

Figure 1: Averaged z-component of the magnetic field at time $t = 100$fs. The large fields to either side of the target have been masked out.

During the course of the simulation an initial fast growth of the out-of-plane magnetic field, between $t =$ 50fs and $t =$ 80fs, is observed. After the initial rapid growth magetic diffusion sets in leading to a slower growth phase after $t =$ 100fs. Figure 1 shows the out-of-plane magnetic field at 100fs into the simulation. The figure clearly shows large magnetic fields as the material interface, with maximum values up to 44MG which are localized to a very thin layer. As a result of the strong magnetic fields, the fast electrons are reflected off the material interface and are well confined inside the high-Z structure.

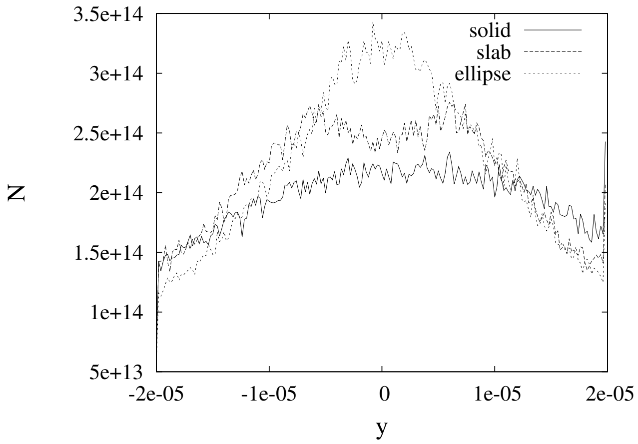

Figure 2: Number density collected by a virtual screen at 20μm behind the target. The electrons were collected from 5μm $\leq x \leq$ 9μm and projected ballistically onto the virtual screen.

To analyse to what extent the electrons remain collimated after leaving the target, we use a new diagnostic. We place a virtual screen at some position behind the target and project the fast electrons in a given region onto that screen, under the simplified assumption that the electrons follow straight ballistic trajectories. The particles are collected on the screen and binned according to their y-coordinate. This produces a number density as a function of the transverse coordinate y. Figure 2 shows this number density for a screen at a position 20μm behind the target. Curves are plotted for three different runs, for the solid, unstrucured target, for the slab geometry and for the elliptical mirror geometry. It can be seen that, while the slab geometry results in a small increase of fast electrons near the axis, only the ellipical geometry actually focuses the electrons, leading to a substantial increase of fast electrons near the axis.

Hybrid Simulations

In order to assess the performance of the magnetic mirror concept under more realistic conditions, we carried out hybrid simulations using the 3D particle hybrid code Zephyros [6, 7, 8]. The code is based on the hybrid method developed by Davies [9]. We use a 250 × 200 × 200 grid with a 1μm cell size. Figure 3 shows the initial target setup. The target consists of Al re-entrant cone the top 100m of which contains a guiding structure consisting of a truncated semi-ellipsoid core of Al surrounded by a CH_2 substrate. Outside the core is a mass of compressed DT, which is centred at $r_{DT} = (200, 100, 100)\mu$m. The background temperature is initially set to 100eV everywhere and the background resistivity was described by the model of Lee and More. The temporal profile of the injected fast electron beam is a top-hat function of 18 ps duration with a total injected

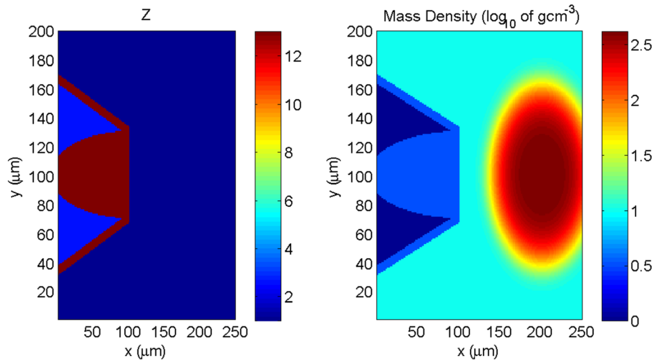

Figure 3: Initial configuration of the hybrid simulation for the charge number Z (left) and the mass density (right). The profiles are rotationally symmetric around the central x-axis.

fast electron energy of 23kJ. This models irradiation at an intensity of $4 \times 10^{20}\,\mathrm{W\,cm}^2$. The angular distribution of the fast electrons is a uniform distribution over a cone where the opening angle θ_{div} is a parameter of the simulation. In the baseline case this is chosen to be $\theta_{\mathrm{div}} = 70°$.

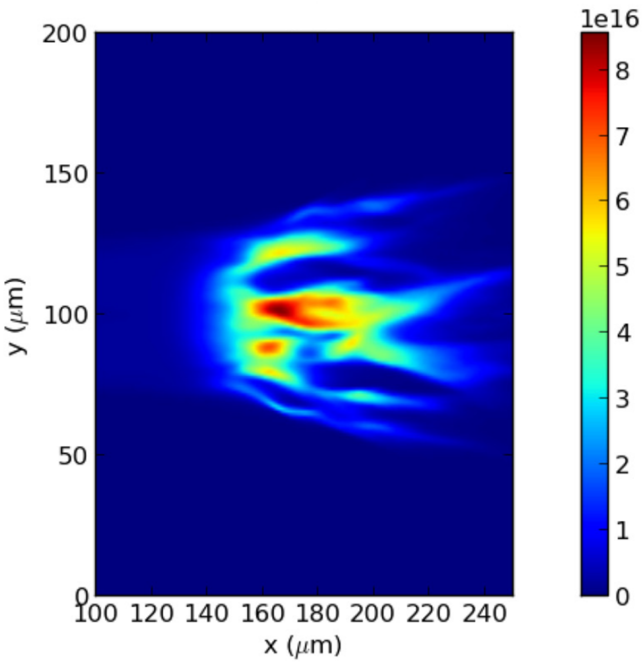

Figure 4: Ion internal energy density at 20ps in $\mathrm{J\,m}^{-}3$ in the baseline simulation for $x > 100\mu$m.

Figure 4 shows the ion internal energy density at 20ps. Of the total energy of the injected fast electrons, 14.07 kJ is deposited in the DT fuel. The rest is either deposited in the cone or lost by fast electrons passing through the far boundaries. About 4.4 kJ is deposited in a hot spot region, defined as a $40 \times 40 \times 40\mu$m cubic region centered at $(170, 100, 100)\mu$m. The energy deposited in this hot spot is used to define the coupling efficiency, which is 19.1% in the baseline case.

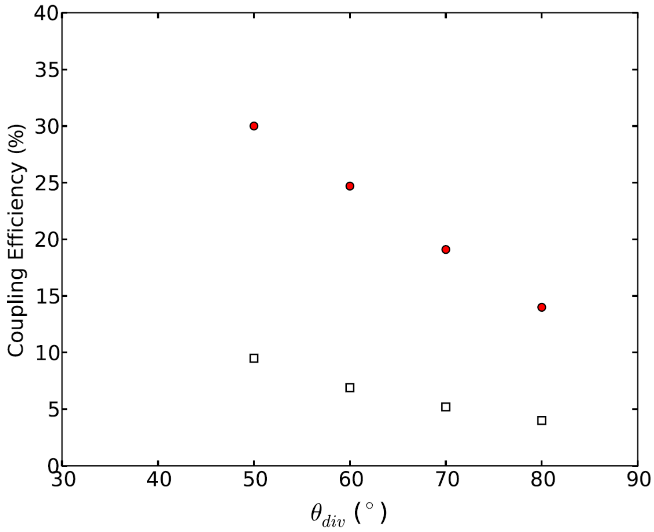

Figure 5: Coupling efficiency into hot spot for varying injectionn spreads (red circles) compared to the baseline case without magnetic mirror (black squares)

Figure 5 shows the coupling efficiency defined in this way for different electron spreads. The coupling efficiency is compared to results of control simulations, where the elliptical mirror is absent from the target structure. As expected, the coupling efficiency falls with increasing divergence half-angle. This observation is true for the control runs as well as the runs with the mirror. However, the coupling is always at least 3 times higher with the mirror than without. We therefore find that the elliptical mirror can be highly beneficial across a range of fast electron divergence angles.

Conclusions

We have carried out a series of numerical simulations in order to investigate a novel configuration to control the flux of fast electrons for FI. The magnetic mirror concept uses principles of mirror optics to design a target geometry that can effectively collimate the fast electrons towards the fuel core. Initial collisional PIC simulations provided a proof of principle for the concept. Analysis of the trajectories showed that the fast electrons were not merely channelled but effectively collimated.

Hybrid simulations extended the analysis to conditions which are much closer to full-scale FI. A number of different aspects of the source–target configuration have been examined, including the fast electron divergence. For multi-kJ conditions the elliptical mirror can improve the coupling efficiency into the hot spot by a factor of 3 to 4. For ponderomotive scaling of the fast electron temperature, we have obtained fast electron to hot spot coupling efficiencies of 20% to 30%.

We conclude that the elliptical mirror scheme has considerable potential for improving the prospects of Fast Ignition, by substantially improving the coupling efficiency.

References

[1] K. L. Lancaster *et al.*, Phys. Rev. Lett. **98**, 125002 (2007)

[2] J. S. Green *et al.*, Phys. Rev. Lett. **100**, 015003 (2008)

[3] A. P. L. Robinson and M. Sherlock, Phys. Plasmas **14**, 083105 (2007)

[4] H. Schmitz *et al.*, Plasma Phys. Controlled Fusion **54**, 085016 (2012)

[5] A. P. L. Robinson and H. Schmitz, Phys. Plasmas **20**, 062704 (2013)

[6] S. Kar et al., Phys. Rev. Lett. 102, 055001 (2009).

[7] B. Ramakrishna et al., Phys. Rev. Lett. 105, 135001 (2010).

[8] A. P. L. Robinson, M. H. Key, and M. Tabak, Phys. Rev. Lett. 108, 125004 (2012).

[9] J. R. Davies, Phys. Rev. E 65, 026407 (2002).

Numerical Modeling of the Sensitivity of X-Ray Driven ICF Implosions to Low-Mode Flux Asymmetries

Contact: robbie.scott@stfc.ac.uk

R.H.H. Scott
Central Laser Facility, STFC Rutherford Appleton Laboratory, Harwell Oxford, Didcot, Oxfordshire, OX11 0QX, United Kingdom.

D.S. Clark, D.K. Bradley, D.A. Callahan, M.J. Edwards, S.W. Haan, O.S. Jones, B.K. Spears, M.M. Marinak, R.P.J. Town, L.J. Suter, *Lawrence Livermore National Laboratory, Livermore, CA 94551, United States of America.*

P.A. Norreys
Central Laser Facility, STFC Rutherford Appleton Laboratory, Harwell Oxford, Didcot, Oxfordshire, OX11 0QX, United Kingdom. Department of Physics, University of Oxford, Parks Road, Oxford OX1 3PU, United Kingdom.

Abstract

The sensitivity of inertial confinement fusion implosions, of the type performed on the National Ignition Facility (NIF) [1], to low-mode flux asymmetries has been investigated numerically. It is shown that large-amplitude, low-order mode shapes (Legendre polynomial P_4), resulting from low order flux asymmetries, cause spatial variations in capsule and fuel momentum that prevent the DT "ice" layer from being decelerated uniformly by the hot spot pressure. This reduces the transfer of implosion kinetic energy to internal energy of the central hot spot, thus reducing neutron yield. Furthermore, synthetic gated x-ray images of the hot spot self-emission indicate that P_4 shapes may be unquantifiable for DT layered capsules. Instead the positive P_4 asymmetry "aliases" itself as an oblate P_2 in the x-ray images. Correction of this apparent P_2 distortion can further distort the implosion while creating a round x-ray image. Long wavelength asymmetries may be playing a significant role in the observed yield reduction of NIF DT implosions relative to detailed post-shot 2D simulations.

1 Introduction

Indirect-drive inertial confinement fusion (ICF) [2, 3, 1] uses lasers to heat the inside of a high-Z cavity (or hohlraum). The absorbed laser energy is re-emitted as x-rays. These x-rays heat the outer surface of a hollow, spherical, low-Z shell that contains a layer of frozen Deuterium and Tritium (DT) fuel. The heated outer shell ablates, creating a rocket-like reaction force, spherically imploding the shell at extremely high velocity (~ 350 km/s). During the implosion, spherical convergence causes the pressure in the central gaseous void (or hot spot) within the shell to rise. This pressure decelerates the shell, both compressing the solid fuel, and converting the shell's kinetic energy into hot spot internal energy, thus heating the hot spot, thereby initiating DT fusion reactions. Provided the hot spot areal density is sufficient, α-particles will further heat the hot spot, causing bootstrap heating, ignition and thermonuclear burn propagation into the surrounding cold fuel. Numerical modeling indicates that the NIF can, for the first time, initiate inertial fusion ignition in the laboratory [4, 5, 6]. In comparison to detailed post-shot simulations [7], current NIF DT layered capsule implosions have neutron yields reduced by $\sim 3-10\times$ and hotspot masses reduced by $2-3\times$ [8, 9], while hot spot temperatures are similar. Low mode capsule shape distortions may explain some of this apparent discordancy [10], as simulations indicate they can reduce the conversion of implosion kinetic energy to hotspot internal energy, thereby bringing the key implosion observables (hot spot mass, energy, temperature and neutron yield) more in line with experiments.

In this Letter, the effects of low-mode capsule shape asymmetries are examined numerically. The non-uniformity of the x-ray flux incident upon the shell and the resultant shell shapes can be described mathematically as a series of Legendre polynomials [11]. It is shown that a P_4 implosion asymmetry, that might result from low-order hohlraum generated flux asymmetries, causes spatial variations in the capsule & fuel momentum. This inhibits uniform deceleration of the capsule and fuel by the hot spot pressure, reducing the transfer of implosion kinetic energy to hot spot internal energy thus significantly reducing the capsule performance. Furthermore, simulated gated x-ray images of the hot spot self-emission show reduced sensitivity to the P_4 mode, instead the images appear to have a pronounced oblate P_2 shape. Reducing the amplitude of the oblate P_2 shape (as measured from the x-ray image) further reduces the sensitivity to the P_4 mode meaning the resulting x-ray images are round despite the capsule shape being highly distorted. Comparisons are made between key physical properties of the implosion, synthetically generated experimental observables, and NIF data.

2 Simulation Methodology

The indirect-drive approach to ICF smooths high mode spatial non-uniformities in the x-ray flux incident upon the capsule, however the spatial distribution of the cones of laser beams which illuminate the hohlraum means that low mode x-ray flux non-uniformities can occur [1], these are considerably lower mode than those recently examined by Thomas *et al* [12]. Capsule-only, two-dimensional (2D), cylindrically-symmetric geometry simulations were performed with the radiation-magnetohydrodynamics code Hydra [13]. These were driven by an x-ray drive taken from an integrated hohlraum simulation which was adjusted to match the shock timing data from the VISAR diagnostic [14, 15] from NIF shot N110521, and the capsule implosion trajectory [16] measured on NIF shot N110625. QEOS [17] was used with tabular opacities and multi-group radiation diffusion. The effects of hohlraum P_4 flux asymmetries were investigating by perturbing the applied flux with a P_4 distribution function of amplitude varying from +10% to −10%. 2D Hydra modeling of the hohlraum & capsule [18] suggests the P_4 flux asymmetry incident on the capsule would be expected to be $< 3\%$, except for in the first ~ 2 ns of the laser pulse where the flux asymmetry can be up to 10%. To date there is no direct measure of NIF hohlraum radiation asymmetry. The flux asymmetries were applied during the discrete time intervals $0-2$ ns (the 'picket' [19]), $2-11.5$ ns (the 'trough'), $11.5-14$ ns (2^{nd} shock), $14-16$ ns (3^{rd} shock) and $16-18$ ns (4^{th} rise) and $18-21.5$ ns (peak drive), creating >200 2D modeling runs of both DT layered capsules and DHe^3 gas filled capsules with a surrogate CH 'fuel' mass (symmetry capsules). In order to recreate images from the NIF gated x-ray diagnostic [20](GXD), time resolved, 11 μm resolution, synthetic gated x-ray images of the hot spot self-emission > 6 keV, were created from polar and equatorial directions by post processing the Hydra runs. Hot spot and synthetic GXD shapes were characterised by a Legendre polynomial decomposition of the appropriate contour. The hot spot contour is defined as the minimum radius where $T_{e_j} > \frac{1}{2}T_{e_{j_{max}}}$ and $\rho_j < \frac{1}{2}\rho_{j_{max}}$ where T_e is the electron temperature and ρ the mass density, 'max' denotes the maximum value within the j^{th} angular 'strip' of cells. This is a robust definition of the hot spot even for highly distorted implosions. Based on previous studies the 17% contour of the GXD is used both for the synthetic GXD and experimentally.

3 The effects of low mode asymmetries

The applied Legendre P_4 flux asymmetries induce P_4 hot spot shapes at stagnation (see Figs. 1 (a) & (c)), the sign of which is dependent on the timing of the applied flux asymmetry. If the asymmetry is present only during the shock compression phase (the first ~ 18 ns), shocks

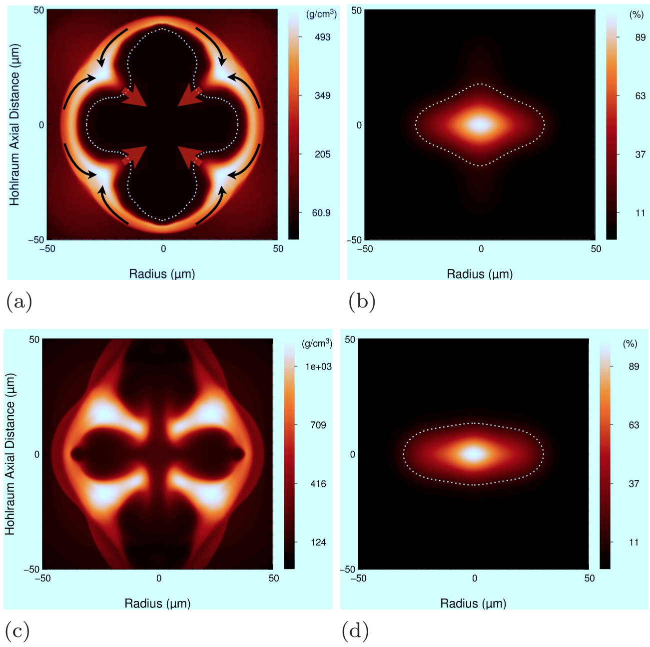

Figure 1: Axis of rotational symmetry is vertical at Radius = 0 μm. (a) DT layered capsule density plot at x-ray bangtime showing a positive Legendre polynomial P_4 shape. This simulation had a 10% flux asymmetry applied from 11.5-14 ns. Black arrows indicate the mass flows which occur during stagnation. After bangtime 'fingers' of fuel continue to flow inwards (red arrows). White dots depict the hot spot contour. (b) Synthetic gated x-ray image of the hot spot self emission from 1(a), white dots show the 17% contour, a_4 is greatly reduced compared to fig. 1(a). (c) The same implosion as fig. 1(a), but 100 ps later. Large a_4 brings the bangtime earlier, meaning this image is plotted at the neutron bangtime of an equivalent spherical implosion. (d) The synthetic GXD from 1(c), showing a large negative (oblate) P_2 and almost zero a_4 despite the obvious P_4 in 1(c).

created in regions of the capsule exposed to higher flux propagate faster, these break out of the inner DT ice layer earlier, causing these regions to move ahead. This also causes ablator mass to flow laterally, away from the high flux region. Consequently during peak drive the regions initially exposed to high flux are at smaller radii, meaning they are accelerated less efficiently by the hohlraum flux and gain less total momentum. They can also have less aerial density (ρr). The net effect is that the regions experiencing high flux during shock compression will protrude outwards at stagnation. Conversely if the flux asymmetry is applied during peak drive, the regions of the capsule exposed to more flux gain more momentum, and protrude inwards at stagnation. Regardless of the timing of the applied asymmetry, during the stagnation phase of the implosion, pressure within the lower density hot spot decelerates the higher density fuel from peak velocity, making any perturbation on

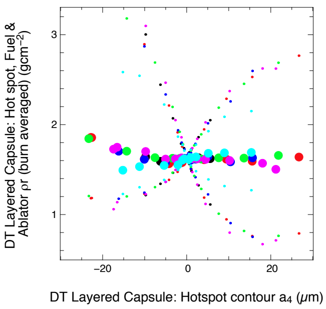

(a)

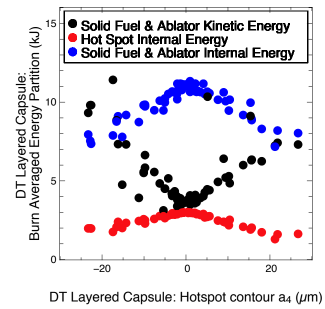

(b)

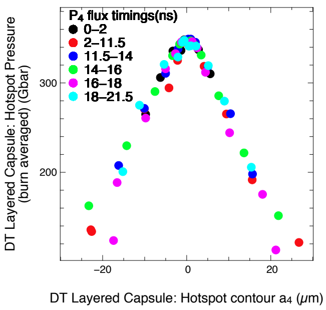

(c)

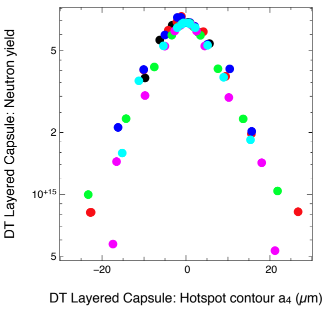

(d)

Figure 2: In (a), (c) and (d), colors depict timing of applied flux asymmetry, see (c) for legend. (a) Burn averaged hot spot + fuel + ablator ρr vs hot spot a_4 at x-ray bangtime: large dots depict spatially averaged ρr, while the smaller points are the corresponding maxima and minima in ρr. Large spatial variations in ρr occur due to P_4. (b) The burn averaged energy partition as a function of hot spot a_4; increasing P_4 perturbations prevent the kinetic energy of the solid fuel + remaining ablator (black) from being converted to both hot spot internal energy (red) and solid fuel + remaining ablator internal energy (blue) during stagnation. (c) Burn averaged hot spot pressure as a function of hot spot a_4. (d) Total thermonuclear neutron yield as a function of hot spot a_4; yield varies by a factor of 15 over the asymmetry range examined.

this interface grow due to the Rayleigh-Taylor instability [21, 22], in addition to the Bell-Plesset growth due to convergence [23]. As the perturbations become larger, velocity shear between the hot spot and cold fuel perturbations can lead to the Kelvin-Helmholtz instability [24, 25], as visible at the tips of the inward protruding 'fingers' in fig. 1(c).

Figure 2 summarizes the scalings of some important DT layered capsule implosion parameters as a function of hot spot a_4, all values are extracted from the simulations at x-ray bangtime. Fig. 2(a) depicts the 'burn averaged' ρr (the burn average of a quantity $Q_b = (\sum_{t=0}^{t=\infty} Q_t Eprodrdt)/\int_{t=0}^{t=\infty} Eprodr\ dt$ where Q_t is Q at time t and $Eprodr$ the thermonuclear energy production rate in time dt) as a function of hot spot a_4. Although the spatially averaged ρr is relatively constant, the lateral mass flows caused by the P_4 can create large spatial variations in ρr. The regions with higher momentum continue to propagate radially inwards; fig. 2(b) depicts the remaining capsule kinetic energy (integrated from the hot spot surface to the ablation front) as a function of a_4, and the partition of that energy into hot spot internal energy (integrated outwards to the hot spot surface) and solid fuel + ablator internal energy (integrated from the hot spot surface to the ablation front). For large a_4 less of the implosion kinetic energy is converted into hot spot internal energy and the hot spot pressure is reduced (fig. 2(c)). The reduction in neutron yield can be as large as 15× for hot spot $a_4 = 20\ \mu$m (flux asymmetry $\sim 10\%$) as shown in fig. 2(d)).

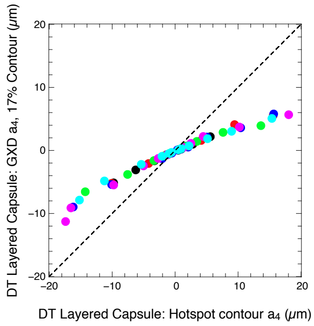

(a)

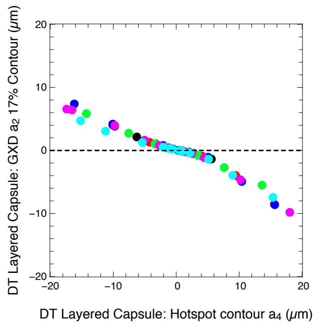

(b)

Figure 3: (a) Synthetic GXD a_4 plotted against DT layered capsule hot spot a_4; particularly for large positive a_4 the GXD is unable to effectively measure the amplitude of the P_4 mode. (b) Synthetic GXD a_2 plotted against DT layered capsule hot spot a_4; for large a_4 the GXD measures a significant P_2 mode amplitude despite the DT layered capsule hot spot a_2 being $0 \pm 1\ \mu$m (not shown).

Analysis of the synthetic GXD images suggests that the a_4 measured experimentally with the GXD is not a true representation of the hot spot a_4, particularly for large positive a_4. Fig. 3(a) depicts the relationship between the DT layered capsule hot spot a_4 and that of the synthetic GXD at x-ray bangtime (using the previously defined contours). The a_4 measured from the synthetic GXD is consistently lower than that of the hot spot. The insensitivity to positive hot spot a_4 is caused by lateral ablator mass flows which accumulate at $\sim 45°$ (see Fig. 1 (a)) and reduce at the equator and poles. The ablator material is rotationally symmetric about the vertical axis, so the accumulated material absorbs the x-rays emitted from the polar-lobes of the hot spot (top and bottom), while allowing x-rays to more readily pass through the equatorial regions (left and right). Consequently the polar-lobes of the hot spot are almost completely invisible in the synthetic GXD plots. This causes the x-ray image to have a negative (oblate) P_2 shape. As the hot spot $a_2 = 0 \pm 1\ \mu$m (a_2 is the amplitude of

Implosion Parameter	NIF expt. range[8]	Hydra ($a_4 = 0$ μm)	Hydra ($a_4 = 20$ μm)
Hot spot internal energy (kJ)	0.7-1.4	3.1	1.3
Hot spot mass (μ g)	2-6.4	8	5.5
X-ray P_0 (μm)	25-30	18.0	23.3
X-ray M_0 (μm)	25-35	17.0	27.1
Ion Temperature (keV)	3.3-4.4	3.9	3.9
Fuel ρr (gcm^{-2})	0.77-0.98	0.7	0.72
Yield (neutrons $\times 10^{14}$)	1.9-6.0	74	5.3

Table 1: A comparison of NIF DT layered capsule experimental data from 4 shots N110608-N110908 with two Hydra implosions, one spherical ($a_4 = 0$ μm), and another with $a_4 = +20$ μm. Large positive P_4 brings the modeled implosion observables approximately in line with the experimental data. P_0 and M_0 are the amplitude of the 0^{th} Legendre polynomial from the 17% contour of the equatorial and polar x-ray images respectively.

the P_2 mode) for all these pure P_4 modelling runs, the P_2 inferred from the x-ray image is a "false" negative P_2 mode. This suggests that a negative P_2 mode measured from the self-emission x-ray image may in fact be a signature of a positive P_4 mode, although it does not preclude the presence of a true P_2 mode. Fig. 3(b) quantifies this aliasing effect. Symmetry capsules are qualitatively and quantitatively very similar. This is potentially important for the interpretation of GXD images from NIF DT implosions, which often exhibit negative P_2 modes [26].

4 Comparison to NIF experimental data

In comparison to detailed 2D post-shot Hydra simulations [7], DT implosions on the NIF currently have yields reduced by $\sim 3-10\times$, while hot spot temperatures are similar. The inferred [8, 9] experimental hot spot volumes are increased in comparison to the post-shot simulations, while the hot spot mass is reduced, causing a $2-3\times$ reduction in the hotspot density. P_4 shape perturbations provide a mechanism which may explain these experimental observations, in particular bringing the yield and ion temperature relationship into better agreement. In the simulations discussed in this Letter, the DT fuel and hot spot do not mix; clear boundaries still exist (note these simulations use smooth capsules, but when nominal realistic capsule surface roughness [27] was employed and modes up to 200 resolved, no significant implosion degradation occurred for the full range of a_4). Consequently, unlike high mode 'mix' [1] (where the hot spot can be radiatively cooled by high Z impurities), the simulated ion temperature inferred from the neutron spectrum remains unaffected at 3.9 ± 0.05 keV for all a_4. The large a_4 does however truncate the thermonuclear burn, moving both the neutron and x-ray bangtimes earlier in time, so the capsule is still converging at bangtime. This, combined with the reduction in conversion of kinetic energy into internal energy, means the hot spot volume is increased. The hot spot mass decreases with positive a_4, bringing Hydra simulations approximately in line with experimental data, as shown in Table 1. This compares NIF experimental data with two Hydra implosions; one is perfectly spherical while the other has a hot spot a_4 of $+20$ μm (flux asymmetry 10%). Notable features of implosions with large positive a_4, all of which bring the simulations towards the data, are, the significantly reduced yield, reduced hot spot internal energy, reduced hot spot mass, unchanged ion temperature, increased x-ray image sizes, and hence increased hot spot volume, which reduces pressure and density, and finally, large spatial variations in ρr. We must emphasize, however, that this should not be interpreted as conclusive evidence that a P_4 asymmetry is responsible for the observed reduced NIF capsule performance. Although this study has concentrated on the P_4 mode, it is likely that all low modes would reduce the conversion of capsule kinetic energy into hot spot internal energy, and may result in similar ambiguity in the shape of the x-ray emission from the hot spot [28].

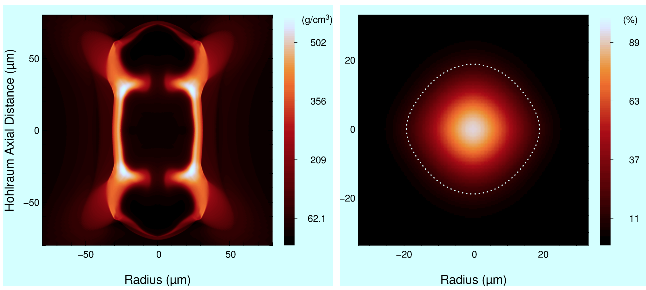

(a) (b)

Figure 4: (a) Density plot of a DT layered capsule run with both P_2 and P_4 flux modes applied. Axis of rotational symmetry is vertical at Radius = 0 μm. (b) The equatorial synthetic GXD image of fig. 4(a) at the same time, dotted line shows 17% contour. Despite the highly non-spherical density distribution in fig. 4(a), the equatorial GXD image is almost perfectly round. Note the spatial scales of (a) and (b) differ for clarity.

5 Coupled P_2 and P_4 asymmetries

As discussed, implosions with a significant P_4 asymmetry can have a very apparent but "false" P_2 asymmetry in GXD images. We find that attempting to correct this "false" P_2 by increasing laser power to the hohlraum waist (the capsule equator) [26] can lead to a round GXD image even though the correction actually produces a more distorted DT fuel ice layer. This is depicted in fig. 4 for the case of a DT layered capsule where we applied and empirically adjusted a P_2 flux asymmetry, in addition to the original P_4, in order to make the synthetic GXD image appear round. As the applied P_2 flux is increased in order to reduce the "false" GXD a_2 towards zero, there is a marked additional reduction in sensitivity to the a_4 measured from the x-ray image relative to that shown in Fig. 3(a) - in this simulation hot spot $a_4 = 25$ μm and GXD $a_4 = 1$ μm. This suggests that attempts to tune the hohlraum to eliminate a "false" P_2 can have the unintended consequence of exacerbating overall asymmetry, while further reducing the diagnostic sensitivity to the asymmetry. A corollary of figure 4, is that it is possible to create imploded configurations which appear to be spherical based on both orthogonal GXD images but, in fact, are significantly asymmetric and have greatly reduced performance in comparison to equivalent spherical implosions because a large fraction of the imploding shell's kinetic energy remains unstagnated.

6 Conclusions

The Science of Fusion Ignition Workshop [30] identified the understanding of the origin of the measured ρr asymmetries as a high priority. Experiments are currently being developed on the NIF to measure low mode asymmetry of the ablator in-flight using x-ray backlighting [16], and of the DT fuel at stagnation using Compton radiography [29]. These will eliminate the degeneracy in inferring implosion asymmetry form hot spot x-ray emission, as identified in this Letter. The P_4 x-ray drive asymmetry may be modified by repointing the laser beams within the hohlraum, moving the laser hot spots relative to the capsule. Large beam repointing may require changing the hohlraum length in order for the laser beams to pass cleanly through the laser entrance holes.

In summary, numerical simulations have been used to examine the sensitivity of implosions similar to those currently taking place on NIF to low-mode flux asymmetries. It is shown that Legendre polynomial P_4 flux modes induce P_4 shape modes at the time of capsule stagnation. The largest P_4 amplitudes studied in this Letter can cause up to 50% of the capsule kinetic energy to remain unconverted to hot spot and DT ice internal energy, in turn reducing the neutron yield by up to 15×. Simulated x-ray images of the hot spot self-emission show reduced sensitivity to the positive P_4 mode, instead the images appear to have a pronounced oblate P_2 shape. Attempting to correct for this apparent P_2 distortion can further distort the implosion while creating x-ray images which appear round and self-consistent from both equatorial and polar directions. This also further reduces the sensitivity to the P_4 mode such that that no quantitative evaluation of the hot spot a_4 can be made. Long wavelength asymmetries may be playing a significant role in the observed yield reduction of NIF DT implosions relative to detailed post-shot 2D simulations.

References

[1] J. D. Lindl *et al.*, Physics of Plasmas **11**, 339 (2004).

[2] N. Basov, Edward teller lectures (1991).

[3] J. NUCKOLLS *et al.*, Nature **239**, 139 (1972).

[4] S. W. Haan *et al.*, Physics of Plasmas **18**, 051001 (2011).

[5] D. S. Clark *et al.*, Phys. Plamas **17**, 052703 (2010).

[6] D. A. Callahan *et al.*, Journal of Physics: Conference Series **112**, 022021 (2008).

[7] D. Clark *et al.*, Physics of Plasmas *(Submitted)* (2012).

[8] P. T. Spinger and C. Cerjan, in *IFSA Proceedings* Bordeaux, France (2011).

[9] C. Cerjan, P. T. Springer and S. M. Sepke, Physics of Plasmas, Submitted.

[10] B. K. Spears *et al.*, Physics of Plasmas **19**, 056316 (2012).

[11] M. Abramowitz and I. A. Stegun, *Handbook of Mathematical Functions with Formulas, Graphs, and Mathematical Tables*, volume pp. 331-339 and 771-802, Dover (1972).

[12] V. A. Thomas and R. J. Kares, Phys. Rev. Lett. **109**, 075004 (2012).

[13] M. M. Marinak *et al.*, Physics of Plasmas **8**, 2275 (2001).

[14] L. M. Barker and R. E. Hollenbach, Journal of Applied Physics **43**, 4669 (1972).

[15] H. F. Robey *et al.*, Physics of Plasmas **19**, 042706 (2012).

[16] D. G. Hicks *et al.*, Physics of Plasmas **19**, 122702 (2012).

[17] R. M. More *et al.*, Physics of Fluids **31**, 3059 (1988).

[18] O. S. Jones, Private Communication, (2012).

[19] H. F. Robey *et al.*, Phys. Rev. Lett. **108**, 215004 (2012).

[20] J. A. Oertel *et al.*, Rev. of Sci. Instrum. **77**, 10E308 (2006).

[21] L. Rayleigh, *Scientific Papers*, Cambridge University Press, Cambridge, England (1900).

[22] G. I. Taylor, *The Instability of Liquid Surfaces when Accelerated in a Direction Perpendicular to their Planes. I*, Proc. R. Soc. London, Ser. A (1950).

[23] R. Epstein, Physics of Plasmas **11**, 5114 (2004).

[24] W. Kelvin, *Hydrokinetic solutions and observations*, London, Edinburgh Dublin Philos. Mag. J. Sci. 42, 362 (1871).

[25] H. Helmholtz, *On discontinuous movements of fluids*, London, Edinburgh Dublin Philos. Mag. J. Sci. 36, 337 (1868).

[26] S. H. Glenzer *et al.*, Science **327**, 1228 (2010).

[27] D. S. Clark *et al.*, Physics of Plasmas **18**, 082701 (2011).

[28] B.K. Spears, Private Communication, (2012).

[29] R. Tommasini *et al.*, Physics of Plasmas **18**, 056309 (2011).

[30] *Science of Fusion Ignition On NIF*, LLNL internal report, LLNL-TR-570412.

Using k-alpha emission to determine fast electron spectra using the Hybrid code ZEPHYROS

Contact *thomas.white@physics.ox.ac.uk*

T. G. White, G. Gregori

Clarendon Laboratory
University of Oxford,
Oxford,
OX3 0PT

A. P. L. Robinson

Central Laser Facility
Rutherford Appleton Laboratory
Harwell Oxford
Didcot
Oxfordshire, OX11 0QX

Introduction

A high intensity laser-solid interaction invariably drives a non-thermal fast electron current through the target. These electrons are accelerated by the radiation field of the laser pulse and can reach energies from a few keV to several MeV. The background resistivity of the solid target or plasma means that the electron current sets up resistive electric fields, a strong return current and magnetic fields. Through a process of collisions and Ohmic heating by the return current the fast electron population loses energy to the surrounding material. On reaching the far side of the target strong sheath fields are set-up which reflect many of the electron back into the target. These processes complicate the dynamics of fast electron transport [1].

Understanding how fast electrons propagate through dense materials is of fundamental interest and has applications relevant to fast ignition schemes and ion acceleration. The return currents also heat solid density material to temperatures from a few to tens of eV creating high energy density states of matter relevant to the study of planetary interiors, warm dense matter and equation-of-state.

A fast electron that has been accelerated through a target produces intense x-ray and VUV emission, primarily through Bremsstrahlung radiation and K-shell ionization in the solid material. The resulting K-shell line emission can be used as an x-ray diagnostic to infer the properties of the fast electron population. Here, we show how the ZEPHYROS hybrid code can be used to infer the spectral temperature, angular divergence and absorbed laser energy of the fast electron distribution from the emitted k-α spectrum. A spectrum of this kind can be obtained experimentally though the use of an absolutely calibrated, imaging, k-alpha spectrometer [2].

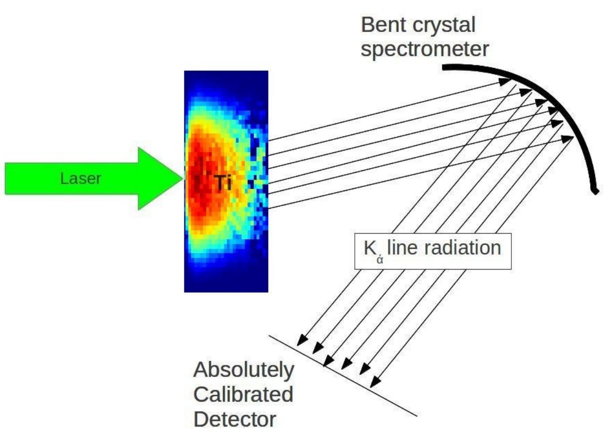

Figure 1: Possible schematic showing how the k-alpha radiation can be obtained experimentally

The code

The ZEPHYROS code is a 3D macroparticle based hybrid code developed by A. P. L. Robinson for the study of electron transport in dense plasmas. The fast electron population is treated as macro particles as in a typical particle-in-cell code while the background electron and ions are treated as a two temperature fluid. The code has many features currently implemented including Bremsstrahlung cooling of the background electrons, electron-ion energy exchange, creation and evolution of magnetic fields and various equation of models for both plasma and solid conditions. Recently, the ZEPHYROS code was upgraded to calculate the k-alpha photon emission rate due to fast-electron-induced k-shell excitation using the algorithm developed by A. G. R. Thomas [3].

The code currently outputs the rate of production of k-alpha photons for each element of the simulation in units of photon number per second per volume. By taking into account radiation transport, the solid angle of a detector and integrating across both the depth of the sample and along a single spatial direction at the back of the target it is possible to obtain the linear intensity of photons on the detector. This number is directly comparable to experimental results obtained from an absolutely calibrated imaging spectrometer.

Simulation parameters

Here we simulate a $2.5{\cdot}10^{18}$ TW cm^{-1} laser with a 30 micron radius flat-topped spot incident on a 200 micron Ti target for 0.7 ps. The simulation contained 400000 fast electron macro-particles distributed thermally at some characteristic temperature. The simulation was carried out in a 20x30x30 box representing a 200x1800x1800 micron sample. It was run for a time of 6 ps and the k-alpha production was output at 0.2 ps steps. Each simulation was run on the SCARF lexicon cluster operated by the CLF. A single run required a time of approximately 300 seconds included post-processing, and operated on a single core. A total of 18000 simulations were carried out representing a range of fast electron characteristics. This range covered a 3D parameter space of size 30x30x20 representing fast electron spectra temperature (0.02-0.6 eV), laser energy absorption (0.5-15 %) and FWHM divergence angle (63 – 86 degrees).

The figure of merit (χ^2) used for comparison between the simulated spectra and the experimental spectra is achieved using a least mean squares fit between the experimental data and simulation,

$$\chi^2 = \frac{1}{N}\sum_x \left(I_{Simulation}(x) - I_{Experiment}(x)\right)^2$$

Here N is the number of experimental data points, x the position across the target surface and I the linear intensity of k-alpha photons hitting the detector. The minimum of this function represents the conditions where the simulated spectra best matches that observed experimentally.

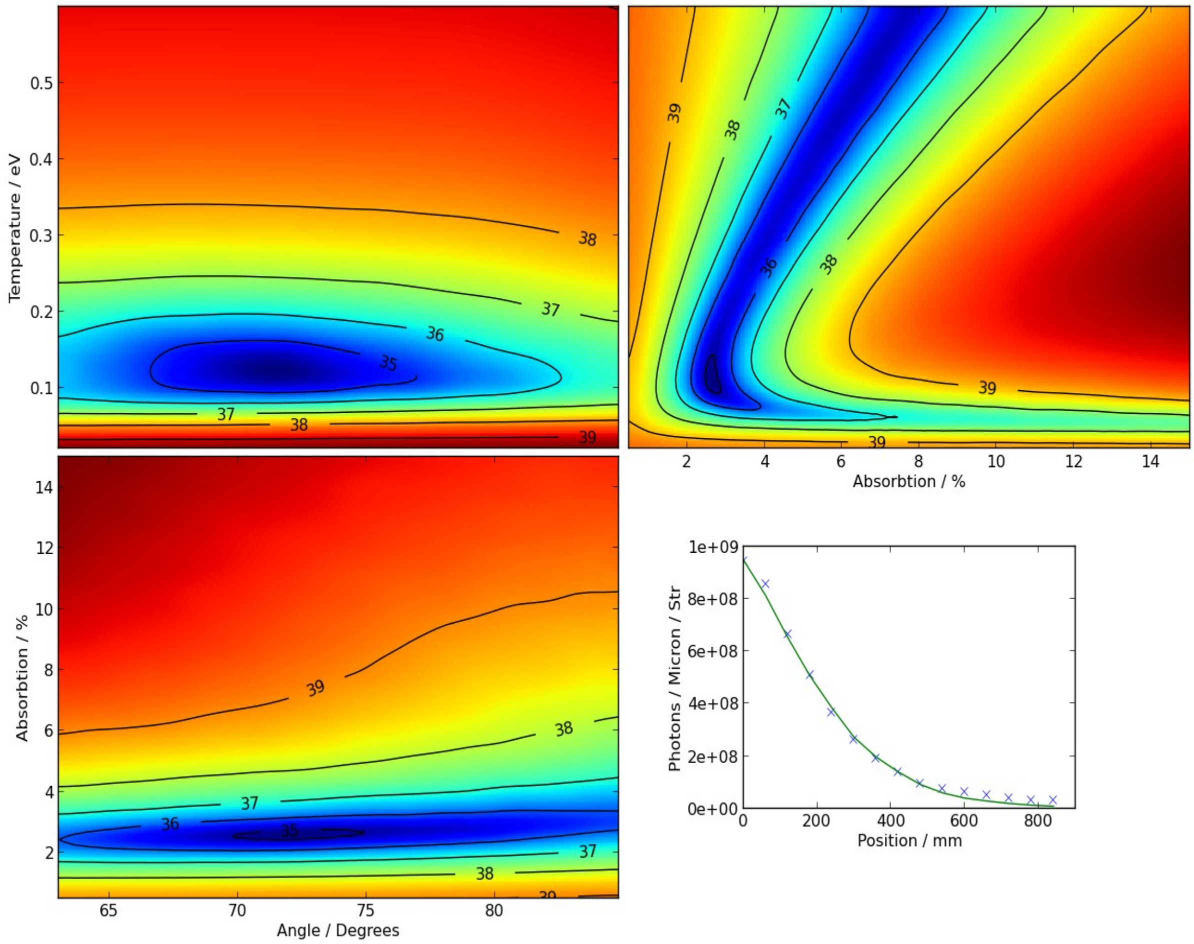

Figure 2: Log of least mean square fit (χ^2) between simulation and experiment as a function of fast electron properties a) Temperature and Angle b) Temperature and Absorption c) Absorption and Angle. d) Best fitting simulation result (line) and typical experimental k-alpha production (crosses)

Results

To demonstrate this process we have used a typical experimental k-alpha spectrum obtained using the set-up shown in Fig. 1. The lowest figure of merit was obtained when the fast-electron temperature was set to 1.2 eV, the angle to 72 degrees and the absorption fraction of laser light to 2.3%. Plotted in Fig. 2 is the log of this figure of merit shown where one of the electron distribution variables is held constant and the other two are varied. It can clearly be seen that there exists a point in the three dimension space where the figure of merit is minimized. This suggests that these three variables are somewhat decoupled and that this measurement allows all three to be determined to within some degree of accuracy.

Additionally, a region of parameter space where the figure of merit is below a certain value determined by the size of the experimental error bars is traced out. This region contains the predicted properties of the fast electron distribution. Shown in Fig. 2-d is the experimentally obtained k-alpha spectrum (crosses) and the simulation result using the best parameters (line).

Conclusions

Utilizing the SCARF lexicon cluster at the CLF facility and the hybrid code ZEPHYROS it is possible to run many thousands of simulations simultaneously to compare with experimental measurements. The addition of k-alpha production to the code along with a small amount of post-processing is one such comparison that could possible give insight into the electron transport and behavior inside a dense target.

Due to the efficient nature of the code it is possible to build up a large parameter space which can then be used to fit experimental data as done here. The agreement between the simulated spectra and experimental results shown in Fig. 2-d both in absolute values and shape is extremely encouraging.

Acknowledgements

The author would like to thank A. P. L. Robinson for his support in upgrading the ZEPHYROS code. In addition, the author thanks the SCARF computing services group at the CLF, P. Norreys, and R. Trines for their assistance in gaining access to the SCARF-lexicon computing cluster.

References

1. A.R.Bell and R.J. Kingham PRL 91, 035003 (2003)
2. T. Missalla *al. Rev. Sci. Inst.*, **70**, 1288 (1999)
3. A. G. R. Thomas *et al.* New J. Phys, **15**, 015017 (2013)

Simulations of ring structures produced in proton acceleration from dense targets

Contact *jinqing.yu@imperial.ac.uk*

Jinqing Yu

The John Adams Institute, Blackett Laboratory, Imperial College London, SW7 2AZ, United Kingdom
Vacuum Electronics National Laboratory, University of Electronic Science and Technology of China
Chengdu, 610054, People's Republic of China

N. P. Dover, C. A. J. Palmer, A. E. Dangor and Z. Najmudin

The John Adams Institute, Blackett Laboratory, Imperial College London SW7 2AZ, United Kingdom

Xiaolin Jin and Bin Li

Vacuum Electronics National Laboratory, University of Electronic Science and Technology of China
Chengdu, 610054, People's Republic of China

Introduction

In the past twenty years, with the development of ultra-high power and ultra-short pulse lasers, relativistic laser-plasma interaction (LPI) has attracted remarkable interest. One of the hottest topics in the field of LPI is laser-driven ion (proton) acceleration because of its potential applications in high energy density physics diagnostics, fast ignition in inertial confinement fusion, and hadron therapy. Sheath acceleration [1] is one of the most important mechanisms in laser proton acceleration and considered to be an effective method to obtain high quality proton beams with currently available laser systems.

Palmer *et al*. have observed proton beam ring structures in experiment of high power lasers interacting with thin gold foils [2]. This particular experiment has not yet been investigated using numerical simulation, which may reveal the mechanism behind the formation of the rings. The Particle-in-cell (PIC) is widely used method in investigating the interaction between high intensity lasers and plasma, and is appropriate for numerical studies of sheath acceleration. To date, there have been no PIC simulations of sheath driven ion acceleration including ionisation processes, and the targets are normally initialised fully ionized. However, without ionisation in the simulation, some important physics may be ignored.

In this report we discuss the simulation of ring structures produced in proton acceleration from the interaction of a high intensity laser modeled on the short pulse laser of Vulcan Target Area West (TAW) with gold targets. An ionisation model has been included in the PIC code, and has been found to have a crucial role in the formation of the rings. The results agree well with experimental results. Using PIC codes including ionisation may open a new avenue in the understanding of laser-matter interaction.

Ionisation model in PIC code and simulation conditions

PIC codes are widely used in plasma physics and astrophysics because it is simple and straightforward. The PIC code we used is EPOCH2D [3], which includes an ionisation model. For tunnelling ionisation, the Ammosov, Delone, Krainov (ADK) equation for ionisation rate has been used, which is suitable for complex atoms of arbitrary principle, magnetic and angular quantum numbers. When the laser field energy is larger than electron binding energy, electron escapes classically in what is known as barrier suppression ionisation (BSI). As collisional ionisation is not included in the code, the ionisation level in the simulation may be lower than the actual value.

A λ=1μm laser pulse with gaussian transverse and temporal laser profile with a pulse length of 400 fs (full-width half maximum (FWHM)) duration and focal spot of 9.0 micron (FWHM) was introduced at normal incidence on the target from the left. The peak laser intensity on laser axis was 8.0×10^{19} W/cm^2. The target was a thin gold (Z= 79) foil. In order to reduce numerical error, the initial mass density of gold atom was 2.0 g/cm^3 (about l/10th of actual gold density). For the sake of comparison, the interaction between the laser and preformed plasma was also considered. The plasma included electrons and fully ionised gold ions. The electron and ion density are $158n_c$ and $2n_c$, respectively, where n_c is critical density. The dimensions of the targets are 10 μm thick (in longitudinal direction) and 60 μm wide (in transverse direction). A hydrogen layer (proton layer for preformed target) of thickness 0.1 μm and width 60 μm is at the rear surface of the gold target. The density of the hydrogen layer is 0.01 g/cm^3 ($2n_c$ for the proton layer).

Simulation results

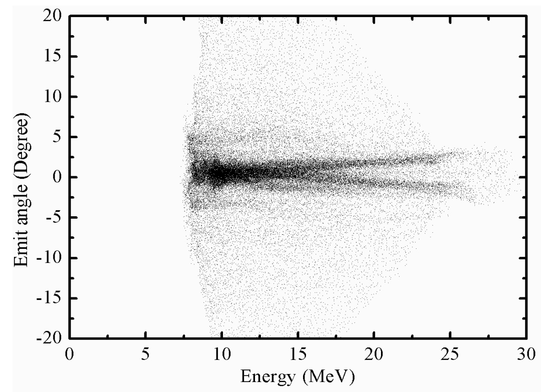

Figure 1: Proton emission angle as a function of their energy for the simulation with a preformed plasma.

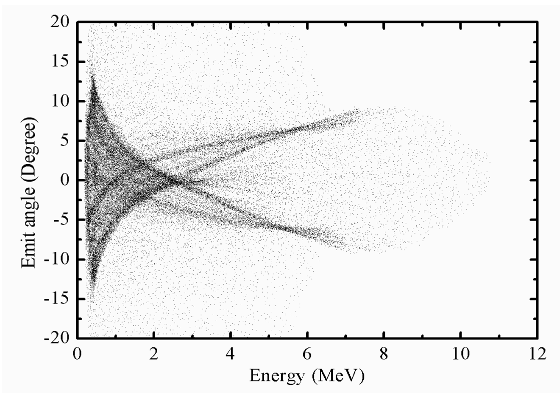

Figure 2: The relation between proton energy and emission angle at the end of the simulation with the ionisation model on.

In the work of Fuchs [4], it is shown that the effective acceleration time is proportional to laser pulse duration, as t_{acc}~1.3 t_L, where t_{acc} is the effective acceleration time and t_L is laser pulse duration. In our simulations, the effective acceleration time should be about 520 fs (Our laser duration

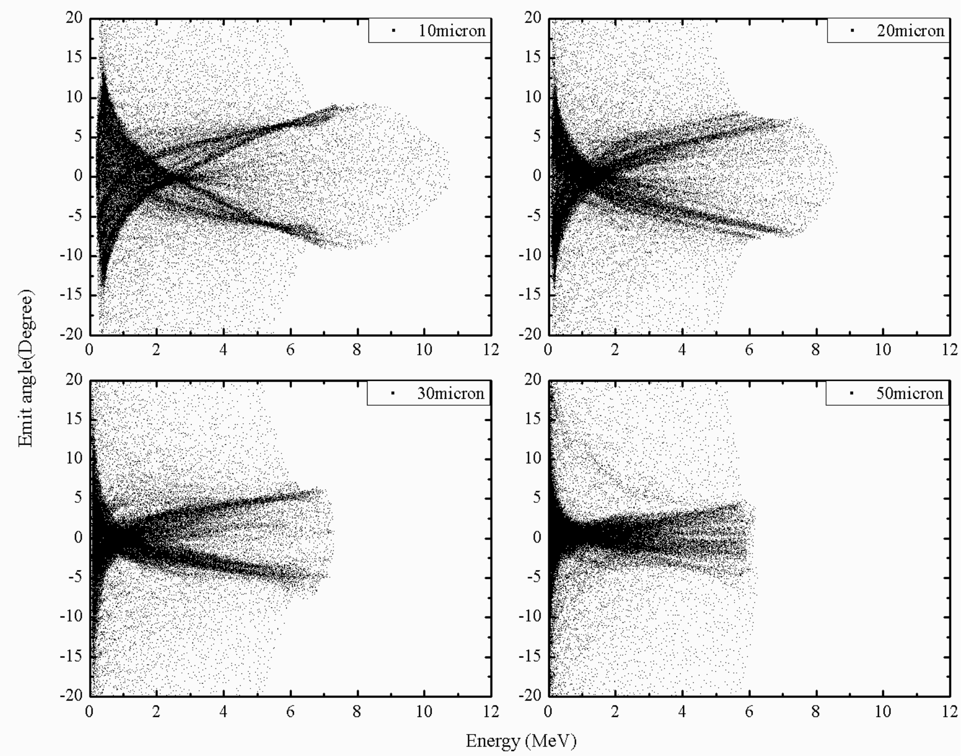

Figure 3: The relation between proton energy and emission angle at the end of the simulation with the ionisation model on is shown as the gold foil thickness was changed from 10 μm to 50 μm with fixed width and the same hydrogen layer.

full-width half maximum is $t_L \sim 400$ fs), which means that the acceleration process in sheath field is finished at the end of simulation time (1.2 ps). Figure 1 shows the angle at which the protons are emitted as a function of their energy at the end of the simulation for the preformed plasma. From the figure, one can see that there are no protons below 5 MeV, such a sharp cut off energy was never observed in the experiment.

When the ionisation model is on, the relation between proton energy and their emission angle is shown in figure 2. From the figure one can see that ionisation plays a very important role on the formation of proton beam's ring structure and energy. At low energy (below 3 MeV), the number of protons is very large and the emission angle is broad. As proton energy increases, a ring structure becomes very clear, and at many energy intervals multiple rings can be found. The exact mechanism for the formation of these rings will be explained fully in future. The distribution of proton energy and their emission angle is similar to the experimental results observed by Palmer *et al* (RCF results shown in Palmer's Thesis [2]).

We also considered the effect of gold foil target thickness on the rings formation. The gold foil thickness was changed from 10 μm to 50 μm with width fixed to 60 μm. In all these four simulations, the hydrogen layer is fixed to 60 μm wide and 0.1μm thick. The relation between proton energy and their emission angle for different thickness are shown in figure 3. From the figure, one can see that the rings number is related to target thickness, which is consistent with the experiment result.

Conclusions

Simulations demonstrating ring structures in proton beam profiles from acceleration from the interaction between a high intensity laser and a gold foil has been reported in this paper. In the simulations an ionisation model has been included, and was found to play a very important role on the ring structure formation. The simulation results are similar to those observed in the experiments. PIC simulation including ionisation process may server as a new way to further understanding the physics of rings formation.

Acknowledgements

Jinqing Yu thanks the Fundamental Research Funds for the Central Universities (Grant No. ZYGX2012YB023).

References

1. S. C. Wilks, A. B. Langdon, T. E. Cowan, M. Roth, M. Singh, S. Hatchett, M. H. Key, D. Pennington, A. MacKinnon, and R. A. Snavely, Phys. Plasmas **8**, 542 (2001); E. L. Clark, K. Krushelnick, J. R. Davies, M. Zepf, M. Tatarakis, F. N. Beg, A. Machacek, P. A. Norreys, M. I. K. Santala, I. Watts, and A. E. Dangor, Phys. Rev. Lett. **84**, 670 (2000); R. A. Snavely, M. H. Key, S. P. Hatchett, T. E. Cowan, M. Roth, T.W. Phillips, M. A. Stoyer, E. A. Henry, T. C. Sangster, M. S. Singh, S. C. Wilks, A. MacKinnon, A. Offenberger, D.M. Pennington, K. Yasuike, A. B. Langdon, B. F. Lasinski, J. Johnson, M. D. Perry, and E. M. Campbell, Phys. Rev. Lett. **85**, 2945 (2000); T. Murakami, Y. Kitagawa, Y. Sentoku, M. Mori, R. Kodama, K. A. Tanaka, K. Mima, and T. Yamanaka, Phys. Plasmas **8**, 4138 (2001);

2. C. A. J. Palmer, PhD. Thesis, Imperial College London, 2011; C. Palmer, C. Bellei, A. E. Dangor, S. Kneip, S. P. D. Mangles, S. R. Nagel, Z. Najmudin and L. Willingale, R. J. Clarke and R. Heathcote, A. Henig and J. Schreiber, M. C. Kaluza and A. Sävart, CENTRAL LASER FACILITY ANNUAL REPORT **2007/2008** 52(2008).

3. C. S. Brady, A. Lawrence-Douglas, and T. D. Arber, Phys. Plasmas **19**, 063112 (2012).

4. J. Fuchs, P. Antici, E. D' Humières, E. Lefebvre, M. Borghesi, E. Brambrink, C. A. Cecchetti, M. Kaluza, V. Malka, M. Manclossi, S. Meyroneinc, P. Mora, J. Schreiber, T. Toncian, H. Pepin, and P. Audebert, Nat. Phys. **2**, 48-54. (2006).